Kinetic Turbulence in Collisionless High-β Plasmas

Lev Arzamasskiy*

School of Natural Sciences, Institute for Advanced Study, Princeton, New Jersey 08540, USA

Matthew W. Kunz

Department of Astrophysical Sciences, Princeton University,
Peyton Hall, Princeton, New Jersey 08544, USA
and Princeton Plasma Physics Laboratory, PO Box 451, Princeton, New Jersey 08543, USA

Jonathan Squire

Physics Department, University of Otago,
730 Cumberland Street, North Dunedin, Dunedin 9016, New Zealand

Eliot Quataert

Department of Astrophysical Sciences, Princeton University,
Peyton Hall, Princeton, New Jersey 08544, USA

Alexander A. Schekochihin

The Rudolf Peierls Centre for Theoretical Physics, University of Oxford,
Clarendon Laboratory, Parks Road, Oxford OX1 3PU, United Kingdom
and Merton College, Merton Street, Oxford OX1 4JD, United Kingdom

We present results from three-dimensional hybrid-kinetic simulations of Alfvénic turbulence in a high-β, collisionless plasma. The key feature of such turbulence is the interplay between local wave-wave interactions between the fluctuations in the cascade and the nonlocal wave-particle interactions associated with kinetic microinstabilities driven by anisotropy in the thermal pressure (namely, firehose, mirror, and ion cyclotron). We present theoretical estimates for, and calculate directly from the simulations, the effective collisionality and plasma viscosity in pressure-anisotropic high-β turbulence, demonstrating that, for strong Alfvénic turbulence, the effective parallel-viscous scale is comparable to the driving scale of the cascade. Below this scale, the kinetic-energy spectrum indicates an Alfvénic cascade with a slope steeper than $-5/3$ due to the anisotropic viscous stress. The magnetic-energy spectrum is shallower than $-5/3$ near the ion-Larmor scale due to fluctuations produced by the firehose instability. Most of the cascade energy ($\approx 80\%$–90%) is dissipated as ion heating through a combination of Landau damping and anisotropic viscous heating. Our results have implications for models of particle heating in low-luminosity accretion onto supermassive black holes, the effective viscosity of the intracluster medium, and the interpretation of near-Earth solar-wind observations.

I. INTRODUCTION

Many space and astrophysical plasmas are so hot and dilute that the mean free path between particle-particle binary interactions is comparable to (or even larger than)

*leva@ias.edu

the characteristic scales of the system. Examples of such weakly collisional plasmas include the intracluster medium (ICM) of galaxy clusters (characteristic scale $L \sim 100$ kpc, Coulomb-collisional mean free path $\lambda_{\mathrm{mfp}} \sim 1$–$10$ kpc [1]), low-luminosity accretion flows onto supermassive black holes (e.g., for the accretion flow around Sgr A* at the Bondi radius, $\lambda_{\mathrm{mfp}} \sim L \sim 0.1$ pc [2]), and the near-Earth solar wind ($\lambda_{\mathrm{mfp}} \sim L \sim 1$ A.U. [3]). All of these plasmas also have particle Larmor radii ρ many orders of magnitude smaller than macroscopic scales (e.g., $\rho/L \lesssim 10^{-14}$ for the ICM, $\lesssim 10^{-10}$ for Sgr A*, and $\lesssim 10^{-6}$ for the solar wind). Despite this strong magnetization, the magnetic fields in

these systems are typically energetically subdominant, with the ratio of thermal pressure p and magnetic pressure $B^2/8\pi$, $\beta \equiv 8\pi p/B^2 \gtrsim 1$.

A particularly interesting question in such high-β, low-collisionality plasmas is how the kinetic physics, which acts on extremely small (and often unobservable) scales, influences the global evolution of the system and impacts the interpretation of current and future observations. The deviations from local thermodynamic equilibrium allowed by the low collisionality of these plasmas can have a dramatic effect on the transport of energy and momentum and the evolution of cosmic magnetic fields. For example, the viscous stress caused by velocity-space anisotropy in the particle distribution function can provide an order-unity contribution to the mass-accretion rate, enhancing or reducing it depending on the shape of the particle distribution [4–7]. In addition, the electrons may have a different temperature than the poorly radiating ions [8,9], thereby complicating the interpretation of interferometric images of black-hole accretion flows (such as those taken by the Event Horizon Telescope [10,11]). As a result, in order to understand high-β astrophysical systems, one must discover how the energy injected in these systems by large-scale processes gets transferred to the electron and ion distribution functions, and how these distributions are shaped by field-particle interactions and various kinetic instabilities.

In this paper, we explore energy transfer and dissipation in collisionless high-β turbulence. This problem is of fundamental importance for the aforementioned astrophysical systems because all of them are observed or thought to host a broadband cascade of turbulent fluctuations. Most theories of magnetohydrodynamic (MHD) turbulence assume that the local nonlinear turbulent interactions are the main process by which energy is transferred from large scales to kinetic scales (see Ref. [12] for a recent review). In collisionless systems, additional energy-transfer channels are available, not only via phase mixing to small scales in velocity space [13] but also through the action of a number of kinetic microinstabilities at ion [firehose [14–17], mirror [18–20], and Alfvén ion cyclotron (AIC) [21]] and electron (firehose, mirror, and whistler [21]) scales. These instabilities feed off the free energy associated with field-anisotropic deviations from local thermodynamic equilibrium (e.g., pressure anisotropies). In the absence of collisions (including any effective collisionality due to wave-particle interactions), such deviations are expected to be largest within the injection range of the cascade, where the amplitude of the turbulent motions is largest [22]. The implication is a nonlocal transfer of energy from large "fluid" scales to astrophysically microscopic kinetic scales, instead of a scale-by-scale cascade that is customarily believed to occur in more mundane systems [23]. This is not necessarily the case in weakly collisional plasmas, in which the (effective) collisionality is large enough to efficiently isotropize the distribution at the injection scale but not throughout the inertial range. In such plasmas, the

pressure anisotropy is driven by the motions between the injection scale and the effective viscous scale, the latter of which being mediated by the wave-particle interactions from microinstabilities. As we show in Sec. II, this effective viscous scale can be comparable to the injection scale of the cascade, making the interactions between microinstabilities and the cascade crucial for the dynamics even at macroscopic scales.

The effect of kinetic microinstabilities on the plasma has been studied with pressure anisotropies driven either externally (with large-scale shear [24,25] or expansion [26,27]) or by individual nonlinear waves (Alfvén [28], ion acoustic [29], magnetosonic [30]). Here we explore, for the first time, and using six-dimensional hybrid-kinetic numerical simulations, the interaction between the local cascade of strong turbulence and the nonlocal excitation of microscale kinetic instabilities that are self-consistently produced by the fluctuations in the cascade themselves.

The article is organized as follows. We begin in Sec. II with a summary of analytical and numerical results on the properties of waves and turbulence in pressure-anisotropic, high-β plasmas. We use these results to obtain analytical estimates for the effective collisionality and effective viscosity in such plasmas. We then test these results with self-consistent numerical simulations in Sec. III, which allow us to measure the effective collisionality and viscosity and to determine the dominant energy dissipation mechanisms in collisionless high-β turbulence. In Sec. IV our results and their range of validity are discussed and put in the context of observations of turbulence in the ICM and in the solar wind. We close in Sec. V with a summary of our results.

II. THEORETICAL EXPECTATIONS

Modern theories of strong plasma turbulence in magnetized plasmas (starting with Goldreich and Sridhar [23]) stipulate a dynamical balance between the linear physics of plasma fluctuations and their nonlinear interactions. In Alfvénic turbulence, the typical linear timescale for a given eddy is determined by the time it takes for an Alfvén wave to cross that eddy. For an eddy whose extent along the local mean magnetic field $\boldsymbol{B}_0$ is $\ell_\parallel$, this timescale is $\tau_{\text{lin}} \sim \ell_\parallel/v_{A0}$, where v_{A0} is the associated Alfvén speed. The nonlinear timescale, on which the mutual shearing and advection of the fluctuations decorrelates the eddy, is estimated as $\tau_{\text{nl}} \sim \ell_\perp/\delta u_\perp \sim \ell_\perp/(v_{A0}\delta B_\perp/B_0)$, where $\ell_\perp$ is the size of the fluctuation across ("perpendicular" to) $\boldsymbol{B}_0$, and $\delta u_\perp$ and $\delta B_\perp$ are the amplitudes of the fluid-velocity and magnetic-field perturbations. The relationship between linear and nonlinear timescales determines how many nonlinear interactions are required to decorrelate the eddies. If $\tau_{\text{nl}} \ll \tau_{\text{lin}}$, different parts of an eddy decorrelate before they can be in causal contact via Alfvén-wave propagation, which leads to a decrease in $\ell_\parallel$ and thus τ_{lin} [31]. On the other hand, if $\tau_{\text{nl}} \gg \tau_{\text{lin}}$, the turbulence is considered to be "weak," and it evolves in a way such
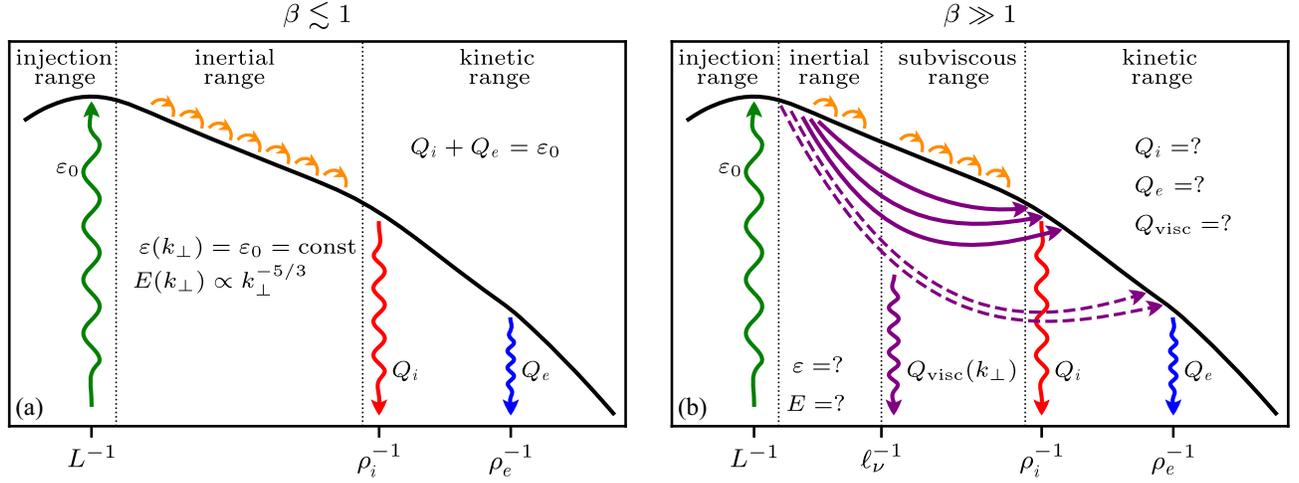
FIG. 1.   Qualitative picture of how the cascade proceeds in low-β (a) and high-β (b) kinetic turbulence. For $\beta \lesssim 1$, the energy flux, injected at some large scale L, remains constant in the inertial range, and is eventually dissipated by ions and electrons at the corresponding kinetic scales. In contrast, high-β plasma allows for the nonlocal energy transfer by kinetic microinstabilities. The effective viscosity of such a plasma can convert bulk kinetic energy into thermal energy. The goal of this paper is to examine the effects of this physics on the turbulent cascade and on the distribution of energy between species.

that these timescales become comparable to one another, $\tau_{\mathrm{nl}} \sim \tau_{\mathrm{lin}}$ at small scales [32]. This causes the system ultimately to settle into a scale-by-scale "critical balance" between the linear and nonlinear timescales [23,33]. The result is a Kolmogorov [34] spectrum in the direction perpendicular to the magnetic field, $k_\perp^{-5/3}$, where $k_\perp \sim 1/\ell_\perp$ is the perpendicular wave number, shown schematically in Fig. 1(a). The associated scale-dependent anisotropy, $\ell_\parallel \propto \ell_\perp^{2/3}$, was confirmed numerically by Refs. [35,36] and subsequently measured in the solar wind using spacecraft data by Ref. [37] (and many others; see Refs. [38,39] for reviews).

In collisionless plasmas, nonlinear wave-wave interactions are accompanied by additional linear and nonlinear physics related to wave-particle interactions. For example, changes in magnetic-field strength caused by turbulent fluctuations on scales much larger than the kinetic scales lead to changes in perpendicular pressure through the conservation of particles' magnetic moments [40]. The pressure then becomes *anisotropic* with respect to the local magnetic-field direction, with the field-perpendicular component of the pressure $p_\perp$ differing from the field-parallel component of the pressure $p_\parallel$. This pressure anisotropy effectively modifies the Alfvén speed by contributing a field-aligned viscous stress [41–43], thereby changing the characteristic linear timescale that features in the critical balance [44,45]. To see that, consider the equation for the evolution of the fluid velocity $\boldsymbol{u}$ in the presence of pressure anisotropy:

$$\varrho \frac{d\boldsymbol{u}}{dt} = -\boldsymbol{\nabla} \cdot \left(\mathbf{P} + \frac{B^2}{8\pi}\mathbf{I} - \frac{B^2}{4\pi}\hat{\boldsymbol{b}}\hat{\boldsymbol{b}} \right), \quad (1)$$

where $d/dt \equiv \partial/\partial t + \boldsymbol{u} \cdot \boldsymbol{\nabla}$ is the comoving time derivative, ϱ is the mass density, $\mathbf{P}$ is the pressure tensor, $\mathbf{I}$ is the unit dyadic, and $\hat{\boldsymbol{b}} \equiv \boldsymbol{B}/B$ is the unit vector in the direction of the magnetic field $\boldsymbol{B}$. For a magnetized plasma in which the characteristic timescales are much longer than ion-Larmor period $2\pi/\Omega_i$, the pressure tensor is predominantly diagonal in a coordinate frame defined by the field direction [40]:

$$\mathbf{P} = p_\perp(\mathbf{I} - \hat{\boldsymbol{b}}\hat{\boldsymbol{b}}) + p_\parallel \hat{\boldsymbol{b}}\hat{\boldsymbol{b}} = p_\perp \mathbf{I} - \Delta p \hat{\boldsymbol{b}}\hat{\boldsymbol{b}}, \quad (2)$$

the latter equality defining the pressure anisotropy $\Delta p \equiv p_\perp - p_\parallel$. Equation (1) may then be rewritten as

$$\varrho \frac{d\boldsymbol{u}}{dt} = -\boldsymbol{\nabla}\left(\frac{B^2}{8\pi} + p_\perp\right) - \boldsymbol{\nabla} \cdot \left[\left(\frac{B^2}{4\pi} + \Delta p\right)\hat{\boldsymbol{b}}\hat{\boldsymbol{b}}\right]. \quad (3)$$

The final term in Eq. (3) highlights the role of the pressure anisotropy in modifying the magnetic tension force compared to MHD, viz.,

$$\frac{\boldsymbol{B} \cdot \boldsymbol{\nabla}\boldsymbol{B}}{4\pi} = \boldsymbol{\nabla} \cdot \left[\frac{B^2}{4\pi}\hat{\boldsymbol{b}}\hat{\boldsymbol{b}}\right] \rightarrow \boldsymbol{\nabla} \cdot \left[\left(\frac{B^2}{4\pi} + \Delta p\right)\hat{\boldsymbol{b}}\hat{\boldsymbol{b}}\right]. \quad (4)$$

As a result of this modification, the effective Alfvén speed in the plasma,

$$v_{A,\mathrm{eff}} \equiv v_A \left(1 + \frac{\beta}{2}\Delta\right)^{1/2}, \quad (5)$$

where $\Delta \equiv \Delta p/p$, $\beta \equiv 8\pi p/B^2$, and $p = (2p_\perp + p_\parallel)/3$ may depart significantly from v_A when $|\Delta| \sim 1/\beta$. In particular, as the firehose instability threshold $\Delta = -2/\beta$, below which $v_{A,\mathrm{eff}}$ becomes imaginary, is approached, it becomes

energetically "cheaper" for the fluid motions to bend the magnetic-field lines [46]. Thus, with $\beta \gg 1$, even small departures from pressure isotropy can influence the plasma dynamics in a dramatic way.

What makes this influence particularly complicated in a turbulent environment is the associated spatiotemporal inhomogeneity of the pressure anisotropy. Pressure anisotropy is generated by the (approximate) conservation of each particle's adiabatic invariants, $\mu \equiv m w_\perp^2 / 2B$ and $\mathcal{J} \equiv \oint m w_\parallel \cdot dx$, where n is plasma number density, m is the particle mass, and $w_{\perp,\parallel}$ are the velocities of the peculiar ("thermal") motions of the particle perpendicular and parallel to the local magnetic field. As the magnetic-field strength fluctuates, the perpendicular and parallel energies of the particles therefore fluctuate as well, resulting in a pressure anisotropy that varies both in space and time. To describe this evolution, if only heuristically, we use the Chew *et al.* [40] equations with $|\Delta| \lesssim 1/\beta \ll 1$ to write, to the lowest order in Δ,

$$\frac{d\Delta}{dt} \approx 3\hat{b}\hat{b}:\nabla u - 3\nu\Delta. \tag{6}$$

Here we assume incompressible motions, include the isotropizing effect of collisions not present in the original equations, and neglect contributions from heat fluxes. The first term on the right-hand side of Eq. (6) captures the adiabatic production of pressure anisotropy caused by changes in magnetic-field strength as measured in the fluid frame. Indeed, adopting an ideal Ohm's law and assuming incompressibility, Faraday's law of induction provides $d\ln B/dt = \hat{b}\hat{b}:\nabla u$. In this case, pressure anisotropy is driven by field-parallel gradients of field-parallel flows, i.e., the "parallel rate of strain." The second term in Eq. (6) represents the relaxation of the pressure anisotropy by collisions, a process that isotropizes the distribution function on a characteristic timescale ν^{-1}. In collisionless plasmas, such isotropization may be provided by the field-particle interactions, and may depend on the local distribution function and magnetic-field strength.

Adapting the Goldreich-Sridhar theory to account for the effective Alfvén speed Eq. (5) only works as long as the pressure anisotropy is small compared to $1/\beta$. For example, an attempt to construct such a theory in the gyrokinetic limit was made in Refs. [44,46]; in this theory, background pressure anisotropy modifies the fluctuations and their nonlinear interactions, while the pressure anisotropy associated with the fluctuations is too small to feed back nonlinearly on the fluctuations themselves. If instead the pressure anisotropy (either background or fluctuation driven) exceeds any of the thresholds of the various kinetic microinstabilities (at high plasma β, mostly firehose and mirror), it can cause energy to be transferred nonlocally [see Fig. 1(b) for a schematic picture of the cascade]. The behavior of turbulence in

such a situation is the topic of this paper. In the remainder of this section, we provide analytical estimates for the effective collisionality and viscosity of a high-β, kinetically unstable plasma supporting a turbulent cascade of electromagnetic fluctuations.

We begin by supposing that energy is injected in the form of bulk motions at an outer scale L and initiates a turbulent cascade of Alfvénically polarized fluctuations with amplitudes $\delta u_\perp$ and $\delta B_\perp \sim (\delta u_\perp / v_A)B_0$, where v_A is the Alfvén speed associated with the mean magnetic field B_0. We further assume that these fluctuations satisfy $\delta B_\perp / B_0 \gtrsim 1/\sqrt{\beta}$ above some scale, so that the pressure anisotropy generated adiabatically by the fluctuating magnetic-field strength is large enough to trigger firehose and/or mirror instabilities [28,47]. In this case, the instabilities grow to wrinkle the magnetic field sharply on ion-Larmor scales, ultimately leading to pitch-angle scattering of ions at an effective collision frequency ν_{eff} that is large enough to limit the fluctuating pressure anisotropy to marginally (un)stable values, viz., $|\Delta p|/p \sim |\hat{b}\hat{b}:\nabla u|/\nu_{\text{eff}} \sim 1/\beta$ [24,48]. With $|\hat{b}\hat{b}:\nabla u| \sim \omega_A (\delta B_\perp / B_0)^2$ for Alfvénic fluctuations that have a linear frequency ω_A, the effective collision frequency ν_{eff} then satisfies

$$\nu_{\text{eff}} \sim \beta \omega_A \frac{\delta B_\perp^2}{B_0^2}. \tag{7}$$

For a critically balanced cascade, ω_A is always comparable to the inverse of the turnover time at each scale. Namely, for an Alfvénic fluctuation with parallel extent $\ell_\parallel$ and perpendicular extent $\ell_\perp$, we have $\omega_A \sim v_A/\ell_\parallel \sim \delta u_\perp/\ell_\perp \sim (v_A/\ell_\perp)(\delta B_\perp / B_0)$. Equation (7) then becomes

$$\nu_{\text{eff}} \sim \beta \frac{v_A}{\ell_\perp} \frac{\delta B_\perp^3}{B_0^3}. \tag{8}$$

If the cascade is approximately conservative [49], then we furthermore have $\delta B_\perp^3 \ell_\perp^{-1} \sim$ const, so that Eq. (8) implies an effective collision frequency independent of $\ell_\perp$ and large enough to regulate the pressure anisotropies generated at all scales in the cascade. Evaluating Eq. (8) at the outer scale L, we find that

$$\nu_{\text{eff}} \sim \beta \frac{v_A}{L} \frac{\delta B_{\perp,L}^3}{B_0^3} \sim \beta \frac{v_A}{L} M_A^3, \tag{9}$$

where $M_A \equiv \delta u_L/v_A$ is the Alfvénic Mach number of the outer-scale motions.

The collisionality given by Eq. (9) implies an effective (field-parallel) Reynolds number:

$$\text{Re}_{\parallel\text{eff}} \equiv \frac{\delta u_L L}{v_{\text{th}i}^2/\nu_{\text{eff}}} \sim M_A^4. \tag{10}$$

From this effective Reynolds number, one can define an effective viscous scale $\ell_\nu \equiv L \mathrm{Re}_{\|\mathrm{eff}}^{-3/4}$, which is appropriate if the dissipation rate due to the effective viscosity is proportional to $\nabla^2 \delta u^2$ [50]. Equation (10) then implies

$$\ell_\nu / L \sim M_A^{-3}. \qquad (11)$$

The viscous scale given by Eq. (11) is equivalent to the Alfvén scale on which the turbulent velocity is approximately Alfvénic. As a result, for strong Alfvénic turbulence, the collisionless viscous scale due to kinetic microinstabilities is comparable to the outer scale of the turbulence. This conclusion does not depend on the plasma β or on the exact instability that regulates the pressure anisotropy (so long as its threshold is proportional to $1/\beta$ and it is saturated via an enhancement of the plasma's collisionality).

One of the caveats of the above derivation is that we assume asymptotic scalings for the cascade, which are valid only for scales much smaller than the driving scale and much larger than the dissipation scale (i.e., in the inertial range). In this case, we interpret any implied value of $\ell_\nu > L$ as indicating $\ell_\nu \sim L$. Indeed, our results suggest that the dissipation scale ($\sim \ell_\nu$) is comparable to the forcing scale ($\sim L$) when $M_A \sim 1$. An alternative derivation of the viscous scale could be obtained by assuming $k_\| \delta u_\| \sim k_\perp \delta u_\perp$, which is equivalent to incompressibility for $M_A \sim 1$ fluctuations. With this assumption, $|\hat{\boldsymbol{b}}\hat{\boldsymbol{b}}:\boldsymbol{\nabla u}|_k \sim k_\perp \delta u_\perp$ increases with $k_\perp$ for a Goldreich-Sridhar-like cascade until it reaches its maximum value of $(\ell_\nu/L)^{2/3} M_A v_A / L$ at $k_\perp \ell_\nu \sim 1$. This different scaling of the parallel rate of strain leads to the same value of the effective Reynolds number, $\mathrm{Re}_{\|\mathrm{eff}} \sim M_A^4$, implying that our results hold for nonasymptotic fluctuations. Note that our assumptions about the cascade are expected to hold only for $M_A \lesssim 1$. For $M_A \gg 1$, dynamo is expected to increase the magnetic-field strength until the Mach number decreases sufficiently [51,52]. In the opposite limit of $M_A \ll 1$, it is possible that the cascade is in the weak-turbulence regime, which has $\delta u_k \propto k_\perp^{-1/2}$ and $k_\| \propto \mathrm{const}(k_\perp)$ [53,54]. Assuming such a cascade with $L_\| \sim L$ gives $\mathrm{Re}_{\|,\mathrm{eff}} \sim M_A^3$ and $\ell_\nu / L \sim M_A^{-9/4}$.

Yet another caveat to these scaling arguments is that the pressure-anisotropy stress can backreact on the motions to reduce $\hat{\boldsymbol{b}}\hat{\boldsymbol{b}}:\boldsymbol{\nabla u}$ below the simple Alfvénic estimate used in Eq. (7) (an effect termed magneto-immutability by Ref. [55]). This would reduce the drive of pressure anisotropy, and thus ν_eff would in turn decrease compared to the above estimates. However, this effect seems unlikely to be important if ℓ_ν is comparable to the scale of an external forcing, because then the dominant contribution to Δp will be from the forcing motions rather than from somewhere in the inertial range.

To determine the importance of the effective collisionality in astrophysical systems, we use Eq. (9) to compute the effective ion mean free path:

$$\lambda_{\|\mathrm{mfp,eff}} \sim \frac{v_{\mathrm{th}i}}{\nu_\mathrm{eff}} \sim M_A^{-2} \frac{v_{\mathrm{th}i} L}{\beta \delta u_L} \sim L \frac{M_A^{-3}}{\sqrt{\beta}}. \qquad (12)$$

In weakly collisional high-β systems like the ICM, this effective mean free path could be smaller than the mean free path due to Coulomb collisions (λ_Coulomb) even if the latter is smaller than the system size. For example, using physical parameters relevant to the Coma cluster of galaxies [56–58],

$$\frac{\lambda_{\|\mathrm{mfp,eff}}}{\lambda_\mathrm{Coulomb}} \approx \frac{L M_A^{-3}/\sqrt{\beta}}{\frac{3\sqrt{2}}{4\sqrt{\pi}} \frac{T_i^2}{n_i \Lambda_i e^4}}$$

$$\approx 0.05 \left(\frac{\delta u_L}{200 \ \mathrm{km\,s^{-1}}} \right)^{-3} \left(\frac{L}{100 \ \mathrm{kpc}} \right) \left(\frac{B}{2 \ \mu\mathrm{G}} \right)^4$$

$$\times \left(\frac{n_e}{10^{-3} \ \mathrm{cm^{-3}}} \right)^{-1} \left(\frac{T_e}{10^8 \ \mathrm{K}} \right)^{-5/2}, \qquad (13)$$

where Λ_i is ion Coulomb logarithm, and the temperatures $T_{i,e}$ and densities $n_{i,e}$ of ions and electrons are assumed to be equal. This simple estimate predicts more than an order-of-magnitude suppression in the effective viscosity of the ICM, consistent with the observationally based conclusion by Refs. [58,59]. Note that the scenario sketched out above for the effective mean free path is very sensitive to the magnetic-field strength ($\propto B^4$) and can change easily by an order of magnitude given current measurement uncertainties.

III. NUMERICAL EXPERIMENTS

A. Method of solution

Astrophysical high-β plasmas typically have extremely large-scale separations that are not computationally feasible to capture in numerical simulations. Because of our focus on the interplay between inertial-range turbulence and ion-scale kinetic instabilities, we adopt a hybrid-kinetic model, in which the ions are treated as kinetic while the electrons are assumed to be fluidlike. Such an approximation ignores the potential effects of electron-scale microinstabilities on the cascade. We argue in Sec. IV that these instabilities are likely to be less important than ion-scale ones (particularly in the weakly collisional ICM, in which the electron pressure anisotropy is expected to be too small to produce instabilities), but this should be verified with fully kinetic simulations in the future.

1. Model equations

The hybrid-kinetic approach that we employ assumes the plasma to be nonrelativistic with all relevant scales much

larger than the Debye length. Plasma on these scales is quasineutral, so $n_e = Z_i n_i$, where $Z_i \equiv q_i/e$. The displacement current in Ampère's law is negligible; hence,

$$n_e \boldsymbol{u}_e = Z_i n_i \boldsymbol{u}_i - \frac{c}{4\pi e} \boldsymbol{\nabla} \times \boldsymbol{B}. \qquad (14)$$

The electric field in hybrid kinetics is obtained from the equation of motion for the electron fluid,

$$m_e n_e \frac{d\boldsymbol{u}_e}{dt} = -\boldsymbol{\nabla} \cdot \mathbf{P}_e - en_e \left(\boldsymbol{E} + \frac{\boldsymbol{u}_e \times \boldsymbol{B}}{c} \right), \qquad (15)$$

after neglecting electron inertia (the left-hand side) and specifying the form of the electron pressure tensor $\mathbf{P}_e$. For simplicity, we assume the electrons to be isothermal and isotropic, $\mathbf{P}_e = n_e T_e \mathbf{I}$, with $T_e = T_{i0} = $ const. As a result, the electric field in our model is given by

$$\boldsymbol{E} = -\frac{\boldsymbol{u}_i \times \boldsymbol{B}}{c} + \frac{(\boldsymbol{\nabla} \times \boldsymbol{B}) \times \boldsymbol{B}}{4\pi e n_i Z_i} - \frac{T_e \boldsymbol{\nabla} n_i}{en_i}, \qquad (16)$$

where the first term is the (MHD) motional electric field, the second is associated with the Hall effect, and the third represents the thermoelectric effect. The magnetic field evolves according to the induction equation,

$$\frac{1}{c} \frac{\partial \boldsymbol{B}}{\partial t} = -\boldsymbol{\nabla} \times \boldsymbol{E}, \qquad (17)$$

and satisfies $\boldsymbol{\nabla} \cdot \boldsymbol{B} = 0$. Note that the final term in Eq. (16) does not contribute to Faraday's law [Eq. (17)], as it may be written as a full derivative $\propto \ln n_i$ and is thus electrostatic.

The ion distribution function $f(t, \boldsymbol{x}, \boldsymbol{v})$ evolves according to the collisionless Vlasov equation:

$$\frac{\partial f}{\partial t} + \boldsymbol{v} \cdot \frac{\partial f}{\partial \boldsymbol{x}} + \left[\frac{Z_i e}{m_i} \left(\boldsymbol{E} + \frac{\boldsymbol{v} \times \boldsymbol{B}}{c} \right) + \frac{\boldsymbol{F}}{m_i} \right] \cdot \frac{\partial f}{\partial \boldsymbol{v}} = 0, \qquad (18)$$

where $\boldsymbol{F}$ is an external force that we use to drive turbulence at the largest scales of the simulation box (specified in Sec. III A 3). The number density $n_i(t, \boldsymbol{x})$ and flow velocity $\boldsymbol{u}_i(t, \boldsymbol{x})$ of ions are then obtained by taking the zeroth and first moments of f.

2. PEGASUS++

Equations (16)–(18) are solved using a new hybrid-kinetic code, PEGASUS++ [60], which is based on the algorithms of its predecessor PEGASUS [61] and on the infrastructure of the popular magnetohydrodynamic code ATHENA++ [62]. PEGASUS++ is much better optimized to take advantage of modern supercomputing architectures than PEGASUS, thereby making the simulations reported in this paper possible.

PEGASUS++ solves Eq. (18) using a particle-in-cell approach, in which the distribution function is represented with a finite number of macroparticles. These

macroparticles' positions and velocities evolve along the characteristics of Eq. (18), with electric and magnetic fields interpolated from the computational grid to the particle positions using a second-order (triangular) shape function. The latter ensures that, in the limit of infinite resolution, the moments of the ion distribution function and their derivatives are continuous in space. PEGASUS++ solves Eqs. (17) and (18) with the electric field given by Eq. (16) using a predictor-predictor-corrector method that is second-order accurate in both time and space. The code employs a staggered grid to preserve $\boldsymbol{\nabla} \cdot \boldsymbol{B} = 0$.

3. Simulation parameters

The ion macroparticles in our simulations are initialized to have a Maxwell-Boltzmann distribution with spatially uniform density $n_i(t = 0, \boldsymbol{x}) = n_{i0}$ and temperature T_{i0}. The electron temperature is constant, $T_e = T_{i0}$, and $Z_i = 1$. The initial magnetic ("guide") field is uniform, $\boldsymbol{B}(t = 0, \boldsymbol{x}) = B_0 \hat{z}$.

Bulk flows in the ion species are driven on large scales by an external force $\boldsymbol{F}$, which is oriented perpendicular to the guide field ($\boldsymbol{F} \perp \hat{z}$) and constructed to be solenoidal ($\boldsymbol{\nabla} \cdot \boldsymbol{F} = 0$). This results in almost incompressible fluctuations with typical density variation of $\sim 5\%$. The force is correlated in time using an Ornstein-Uhlenbeck process with a correlation time equal to the Alfvén crossing time, $t_{\text{corr}} = (k_\parallel^f v_{A0})^{-1}$, associated with the smallest parallel wave number of the forcing $k_\parallel^f$. This forcing results in fluctuations that are primarily Alfvénically polarized, a feature that makes our simulations relevant to many space and astrophysical plasmas. For example, observations of turbulence in the solar wind find that most of the power is in fluctuations that are Alfvénically polarized [63–65]. Outside of the solar wind, *Hitomi* observations of the ICM [66] show that the turbulent motions in the Perseus cluster of galaxies have $\delta u \sim 160$ km/s, consistent with subsonic turbulence and an Alfvénic Mach number $M_A \gtrsim 1$, given typical values of the plasma $\beta \sim 100$ implied by Faraday rotation measurements of the intracluster magnetic field in several clusters [57,67–70]. Similarly, the turbulence in black-hole accretion flows is expected to be composed of incompressible fluctuations, as indicated by local shearing-box simulations of the magnetorotational instability [5,71,72] (although a recent study shows a comparable amount of slow-mode fluctuations [73]).

We perform multiple simulations of driven turbulence in high-β, collisionless plasmas. All simulations employ an elongated computational domain spanning a size of $L_x \times L_y \times L_z \approx (120.5\rho_{i0})^2 \times 241\rho_{i0}$ with $384^2 \times 768$ grid cells and 1000 macroparticles per cell. These dimensions imply perpendicular wave numbers $k_\perp$ that span both an inertial range, with $k_{\perp,\text{min}}\rho_{i0} \approx 0.05$, and a kinetic (sub-Larmor) range, with $k_{\perp,\text{max}}\rho_{i0} = 10$. While it is not computationally feasible to run even larger simulations,
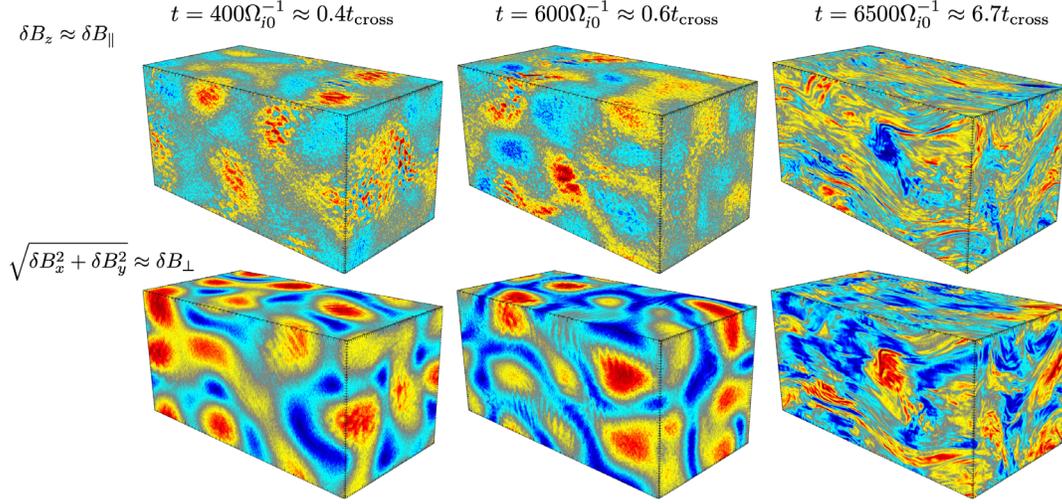
FIG. 2.   Time evolution of the magnetic-field strength along the guide field ($\delta B_z \approx \delta B_\parallel$, upper row) and perpendicular to the guide field ($\sqrt{\delta B_x^2 + \delta B_y^2} \approx \delta B_\perp$, lower row). We show three snapshots: $t \approx 0.4t_{\text{cross}}$, when we see the first mirror fluctuations (see also Fig. 16 in Appendix A and further discussion there); $t \approx 0.6t_{\text{cross}}$, when we detect AIC fluctuations (see also Fig. 17); and in the quasisteady state ($t \approx 6.7t_{\text{cross}}$), when we can instead identify firehose fluctuations (see also Fig. 6).

we have tested the convergence with smaller simulations and obtained qualitatively similar results. The majority of the results we present in this paper (the exception being Figs. 11 and 12) are drawn from two simulations that have $\beta_{i0} = 4$ and 16, but identical energy injection rates per volume $\varepsilon_{\text{dr}} = n_{i0}(L_x/L_z)^2 v_{A0}^2/2t_{\text{corr}}$. The latter is expected to drive critically balanced fluctuations at the outer scale of the box with amplitudes $\delta u_L/v_{A0} \sim L_x/L_z = 0.5$; the actual strength of the fluctuations is time dependent and can be different from this value, depending on the response of the plasma to the driving (the values measured in our runs are $M_A \approx 0.35$ for $\beta_{i0} = 16$ and $M_A \approx 0.48$ for $\beta_{i0} = 4$). In these two simulations, the forcing excites fluctuations with $k_\perp \in [1, 2]k_{\perp,\text{min}}$ and $k_\parallel \in [1, 2]k_{\parallel,\text{min}}$. We also test driving with $k_\perp = k_{\perp,\text{min}}$ and $k_\parallel = k_{\parallel,\text{min}}$ in an additional run, which produces more coherent large-scale modes than does the other forcing scheme (see Fig. 11). We also reproduce our results qualitatively and quantitatively using smaller runs with $\delta u_L/v_{A0} \sim L_x/L_z = L_y/L_z = 1.0$. Each simulation is run for several Alfvén crossing times $t_{\text{cross}} \equiv L_\parallel/v_{A0}$ to achieve quasisteady state (these simulations are never in a true steady state because of continued energy injection from driving and, consequently, continued heating of the underlying ion distribution). For our $\beta_{i0} = 16$ simulations, $t_{\text{cross}} \approx 964\Omega_{i0}^{-1}$; for $\beta_{i0} = 4$ simulations, $t_{\text{cross}} \approx 482\Omega_{i0}^{-1}$.

Most of the energy injected by forcing leads to particle energization. The remaining energy cascades below the ion Larmor scale, which can eventually lead to a pileup of magnetic energy at the grid scale (because we employ hybrid-kinetic model, there are no electron-kinetic and -inertial effects to absorb this energy or unfreeze the magnetic flux). To mitigate this effect, we add hyper-resistive dissipation with the value of resistivity just large enough to dissipate energy at the grid scale. This hyper-resistivity is implemented as an additional electric-field component in Eq. (17) of the form $\boldsymbol{E}_{\text{hyper}} = -\eta_{\text{hyper}}\nabla^2\boldsymbol{J}$, where $\boldsymbol{J} = (c/4\pi)\nabla \times \boldsymbol{B}$ is the electric current.

B. Evolution of high-β turbulence

In this section, we summarize the evolution of turbulent fluctuations in our simulations of high-β turbulence. This evolution is illustrated with three-dimensional snapshots of the magnetic field in Fig. 2 and is separated into several stages: the excitation of mirror and AIC instabilities at early times, when the external driving dominates; an intermediate steady state dominated by Landau damping; and a quasisteady state characterized by the coexistence of a turbulent cascade and microfluctuations associated with the firehose instability.

1. Excitation of mirror and ion-cyclotron instabilities

In our simulations of high-β turbulence, large-scale fluctuations in the bulk ion velocity are driven by the external forcing. These motions cause the volume-averaged magnetic-field strength to increase, which produces positive temperature anisotropy, $\Delta T \equiv T_\perp - T_\parallel > 0$, through adiabatic invariance. Figure 3 shows the evolution of the box-averaged parallel (red line) and perpendicular (blue line) temperatures during the simulation at $\beta_{i0} = 16$. (Density fluctuations in our simulation are small, so adopting density-weighted averaging does not change the results significantly.) The box-averaged temperature anisotropy, $\overline{\Delta T} = \delta T_\perp - \delta T_\parallel$, where $\delta T_{\perp,\parallel} \equiv \bar{T}_{\perp,\parallel} - T_{i0}$, is shown with the purple line. Very early in the simulation,
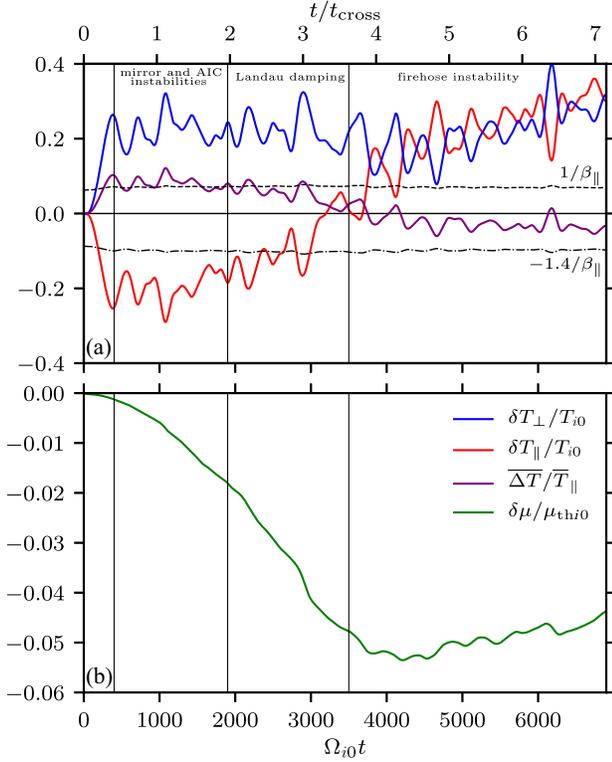
FIG. 3. (a) Time evolution of box-averaged perpendicular and parallel temperatures of the plasma ($\delta T_{\perp,\parallel} \equiv \bar{T}_{\perp,\parallel} - T_{i0}$) and box-averaged temperature anisotropy $\overline{\Delta T} = \delta T_\perp - \delta T_\parallel$ in $\beta_{i0} = 16$ simulation. Different stages of the simulation are marked with vertical lines. See text for more details about individual stages: Sec. III B 1 and Appendix A for mirror and AIC stage, Sec. III B 2 for Landau-damping stage, and Sec. III B 3 for quasisteady-state firehose stage. (b) Evolution of box-averaged magnetic moment of particles ($\delta\mu \equiv \bar{\mu} - \mu_{\mathrm{thi0}}$). During the mirror, AIC, and Landau-damping stages, the average magnetic moment decreases due to scattering off mirror and AIC fluctuations. In the quasisteady state, it slowly increases, because of ion heating and coupling of perpendicular and parallel temperatures due to scattering of ions off firehose fluctuations.

the box-averaged temperature anisotropy $\overline{\Delta T}/\bar{T}_\parallel$ reaches the $1/\beta_\parallel$ threshold for the mirror instability. Some parts of the box also cross the threshold for rapid growth of the AIC instability, which we take to be $0.5/\sqrt{\beta_\parallel}$ following Refs. [21,74]. (The AIC instability is technically thresholdless, but its growth rate decreases exponentially for pressure anisotropies below $\approx 0.5/\sqrt{\beta_\parallel}$; see Refs. [27,75,76] for additional details on the AIC instability's thresholds.) As a result, mirror and AIC fluctuations appear at small scales. These fluctuations can be seen in the three-dimensional snapshot of $\delta B_\parallel$ in Fig. 2 (left-hand column), and in more detail in Fig. 16 in Appendix A, where we also present a detailed structure-function analysis of mirror and AIC modes. Ultimately (after ≈ 2–3 Alfvén crossing times), the temperature anisotropy falls below the mirror threshold and

positive-pressure-anisotropy instabilities are no longer driven, meaning that the mirror and AIC stages are just transient in our simulations. In the quasisteady state, only a small portion of the simulation box is above the mirror threshold, and mirror fluctuations are not obviously present (see Fig. 5 for more detail).

2. Landau-damping stage

After this initial transient, the simulation reaches an intermediate quasisteady state. Its key characteristic is growth of the parallel temperature of the plasma. As we show in Fig. 3, at the start of the $\beta_{i0} = 16$ simulation (before $t \approx 0.3 t_{\mathrm{cross}}$), the temperatures evolve adiabatically: conservation of particles' adiabatic invariants implies $T_\perp \propto B$ and $T_\parallel \propto B^{-2}$, and thus the temperature anisotropy is driven toward positive values as B increases. Once $\Delta T/T_\parallel$ reaches the $1/\beta_\parallel$ threshold of the mirror instability, Larmor-scale magnetic mirrors are produced, which limit further growth of pressure anisotropy by trapping particles in the deepening troughs of the mirrors where the total magnetic-field strength is approximately constant [24,48,77].

Further evolution of the system is influenced by two processes. Pitch-angle scattering off the AIC fluctuations and the edges of strong mirror fluctuations reduces the average magnetic moments of particles [Fig. 3(b)]. At the same time, the parallel temperature steadily grows during this period. Part of this growth can be attributed to pitch-angle scattering, occurring at a rate that can be estimated from the evolution of the average magnetic moment [Fig. 3(b)]. From $\Omega_{i0} t = 2000$ to 3500 (or from ~ 2 to $\sim 3.5\, t_{\mathrm{cross}}$), it changes by $\delta\mu/\mu_{\mathrm{thi0}} \sim 0.035$, corresponding to $\delta T_\perp/T_{i0} \sim 0.035$. Assuming that this change is due to
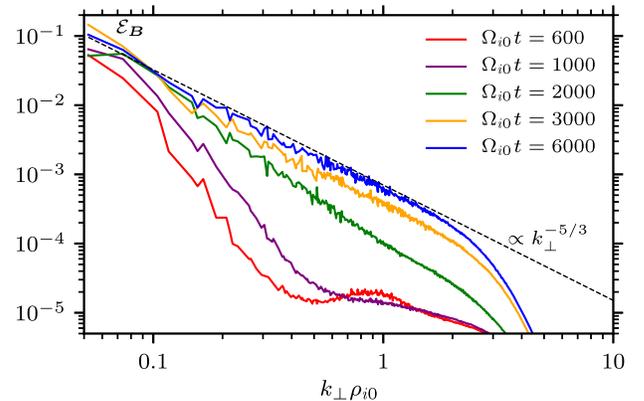
FIG. 4. Time evolution of the magnetic-energy spectra in the $\beta_{i0} = 16$ simulation. In the initial phase of the simulation (red line, Sec. III B 1), mirror instability is triggered, and the spectrum has a bump at kinetic scales. In the Landau-damping stage (green and orange lines, Sec. III B 2), the spectrum is steeper than $k_\perp^{-5/3}$ due to dissipation of turbulence. In the quasisteady state (blue line, Sec. III B 3), firehose fluctuations are produced, and the spectrum becomes slightly shallower than $k_\perp^{-5/3}$.

pitch-angle scattering, $\delta T_\parallel / T_{i0} \sim 2 \delta T_\perp / T_{i0} \sim 0.07$, which is only enough to explain ~25% of the parallel heating during the same time period. We interpret the remaining energization as caused by the Landau damping of Alfvénic fluctuations. This interpretation is also supported by the spectrum of magnetic energy ($\mathcal{E}_B$) being much steeper than $-5/3$ (see Fig. 4), in agreement with gyrokinetic results [78]. In contrast, in kinetic simulations of $\beta \lesssim 1$ turbulence [79,80], a spectrum with a slope of $-5/3$ develops within ~1–2 Alfvén crossing times. Additional evidence for Landau damping can be found in the evolution of the ion distribution function, which shows flattening near the Alfvén speed (see Fig. 19) and from analysis of the field-particle correlation function (not included in the paper), which exhibits resonant features near v_A, consistent with expectations from Landau damping [81]. Details of this diagnostic can be found in Refs. [79,80].

This Landau-damping phase continues until the pressure anisotropy becomes negative, the firehose instability is triggered, and the simulated turbulence reaches a quasi-steady state. A very rough estimate for the time required for Landau damping to drive the pressure anisotropy beyond the firehose threshold may be obtained by supposing that the entire cascade rate were dissipated as parallel energization. In this case, the parallel temperature would grow large enough to produce a firehose-unstable pressure anisotropy within a time $t/t_{\text{cross}} \sim n \Delta T_\parallel \varepsilon_{\text{dr}}^{-1} t_{\text{cross}}^{-1} \sim \Delta p_\parallel n^{-1} M_A^{-2} v_A^{-2} \sim v_{\text{th}}^2 \beta^{-1} M_A^{-2} v_A^{-2} = M_A^{-2}$. For our simulations having $M_A \approx 0.5$, this time is $\sim 4 t_{\text{cross}}$.

3. Quasisteady state

Once the combination of pitch-angle scattering and Landau damping drives the pressure anisotropy beyond the firehose threshold, magnetic-field fluctuations grow on ion-Larmor scales at the expense of the anisotropy in the distribution function. A quasisteady state results in which the magnetic spectrum acquires power at small scales that locally flattens it to be shallower than $k_\perp^{-5/3}$ and the box-averaged pressure anisotropy is close to zero but slightly negative (see Figs. 3 and 4, respectively). Figure 5 provides further information on the pressure anisotropy in the quasisteady state by showing its distribution versus $\beta_\parallel$ (so-called "Brazil" plots, extensively used in the solar-wind community [82,83]). The accompanying dashed lines indicate the thresholds of the mirror instability ($1/\beta_\parallel$) and of the fluid firehose instability ($-2/\beta_\parallel$), beyond which the Alfvén speed becomes imaginary. The dot-dashed line at positive pressure anisotropy represents the threshold of the AIC instability ($\approx 0.5/\sqrt{\beta_\parallel}$), which is active in the beginning of the run. At negative pressure anisotropy, the dot-dashed line shows the approximate threshold ($\approx -1.4/\beta_\parallel$) of the kinetic firehose instability [45,84]. Unlike in the mirror and AIC snapshots (Figs. 16 and 17 of Appendix A), the pressure anisotropy is bound between the
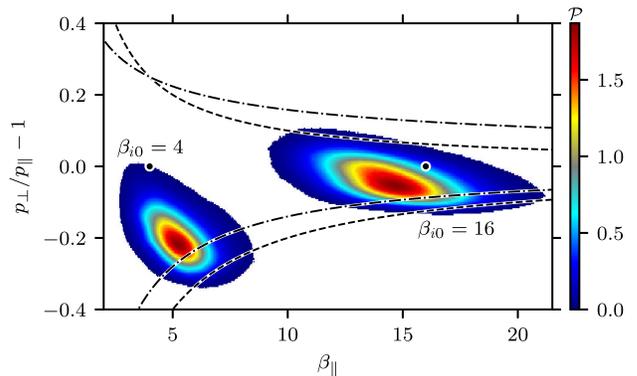
FIG. 5. A probability density function of pressure anisotropy and parallel plasma β for simulations with $\beta_{i0} = 4$ and $\beta_{i0} = 16$. Histograms are normalized so that the integral over $\beta_\parallel$ and $p_\perp / p_\parallel - 1$ equals 1. Black dots indicate the positions of these simulations at the start of each run. Dashed and dot-dashed lines represent the threshold of various kinetic microinstabilities (see text for more detail). Despite being initially driven toward positive values, the quasisteady-state pressure anisotropy is negative, and is close to the $-1.4/\beta_\parallel$ threshold of kinetic firehose instability (dot-dashed line).

mirror and firehose instability thresholds, hugging the latter more closely. The average pressure anisotropy is negative, and its absolute value is smaller than $1/\beta$.

This distribution of pressure anisotropy in the quasisteady state is very different from what has been found in comparable Braginskii-MHD simulations of Alfvénic guide-field turbulence [55] and of magnetorotational turbulence [7], in which a significant amount of the simulated plasma sits up against either the mirror or the firehose threshold [85]. There are (at least) two reasons for this difference. First, our kinetic simulations allow for collisionless damping, which we find constantly pushes the simulated plasma toward the firehose threshold by parallel heating the ions. Second, once the kinetic instabilities are triggered, they self-consistently produce Larmor-scale mirror and firehose fluctuations, which regulate the pressure anisotropy. These fluctuations decay rather slowly [29,48], and continue to scatter particles toward isotropy even after the pressure anisotropy has returned below the instability thresholds. As a result, Δp is reduced much more efficiently and its mean quasisteady-state value is smaller than seen in Braginskii-MHD simulations, which account for these instabilities with a large "limiter" collisionality that is active only when the plasma ventures beyond the stability thresholds.

Figure 6 shows slices of the magnetic-field strength, plasma fluid velocity, and pressure anisotropy normalized to magnetic pressure $8\pi\Delta p/B^2$, all in the quasisteady state of the $\beta_{i0} = 16$ simulation. Mirror fluctuations, manifest at the beginning of the run (Fig. 16), are no longer visible. This is likely due to their decay and shearing by the fluctuations associated with the turbulent cascade. One can
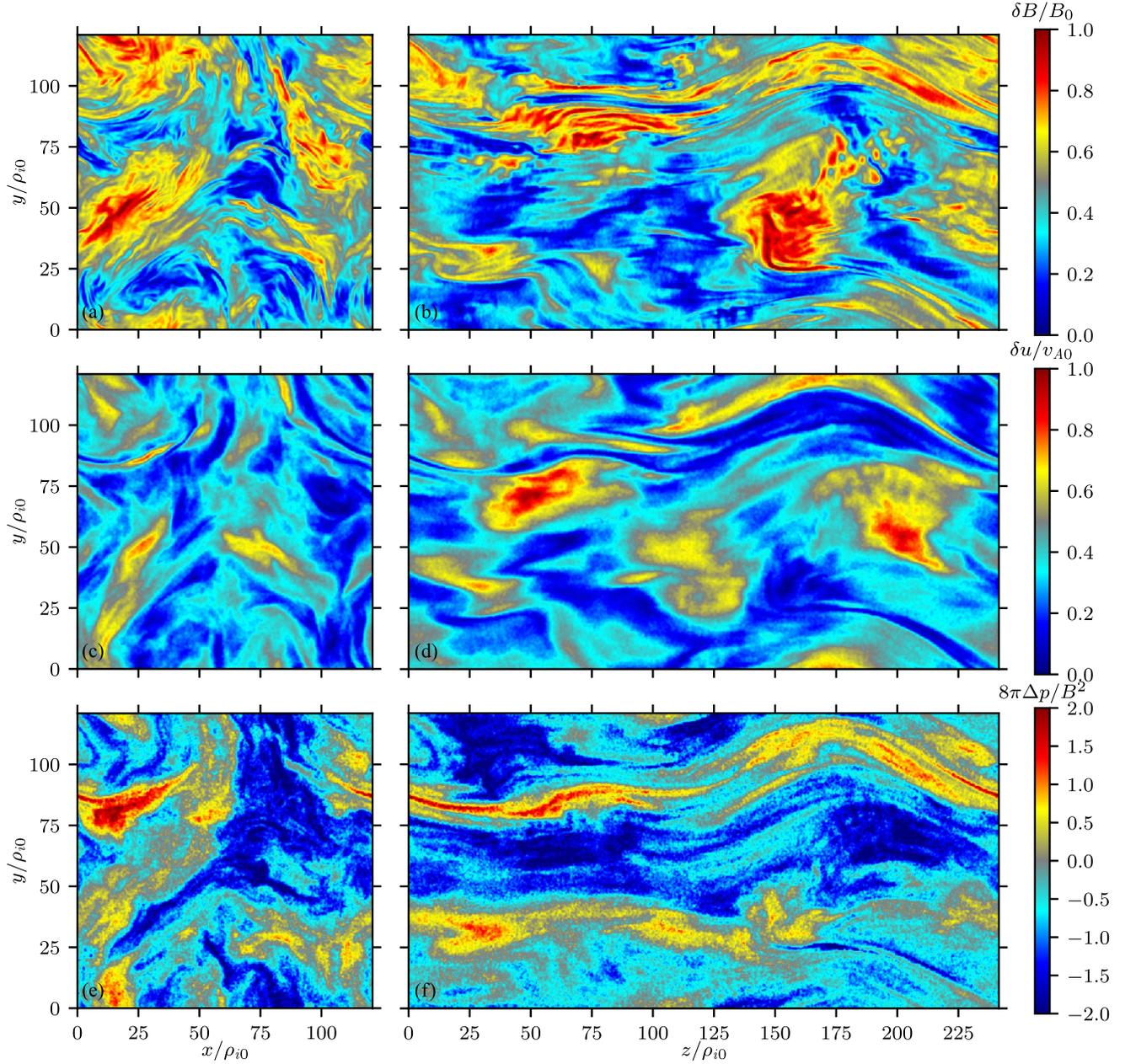
FIG. 6.   Snapshots of the magnetic-field-strength fluctuations (a),(b), fluctuations of the flow velocity (c),(d), and of pressure anisotropy normalized to the magnetic pressure (e),(f), all taken in the quasisteady state of $\beta_{i0} = 16$ simulation. There is much more small-scale structure in the magnetic field relative to the flow velocity, which indicates that the effective magnetic Prandtl number is large. Mirror and AIC fluctuations are not apparent, unlike in the earlier stages of the same simulation (Figs. 16 and 17). Instead, there are small-scale oblique modes in the regions with large negative pressure anisotropy (e.g., near $z \approx 25\rho_{i0}$, $y \approx 75\rho_{i0}$ and $z \approx 130\rho_{i0}$, $y \approx 10\rho_{i0}$). We associate these fluctuations with the firehose instability.

still see some quasiparallel fluctuations in regions with positive pressure anisotropy (e.g., near $z \approx 25\rho_{i0}$, $y \approx 75\rho_{i0}$ and $z \approx 130\rho_{i0}$, $y \approx 10\rho_{i0}$), which we attribute to AIC instability. Additionally, one can notice small-scale oblique modes of large amplitude (such as those at $y \approx 75\rho_{i0}$ and $z \approx 200\rho_{i0}$), which are correlated with regions of negative pressure anisotropy. Studies of localized firehose instability [24] show that this instability produces similar

oblique modes, and so we interpret those fluctuations as firehose modes produced continually in the quasisteady state.

In the quasisteady state, the box-averaged magnetic moment of the particles slowly increases with time [Fig. 3(b)]. The reason for this is that the perpendicular and parallel components of the temperature are coupled to one another via pressure-anisotropy regulation by the

firehose instability (although many different instabilities are present in our simulations, the firehose is much more efficient at scattering particles than mirror [24], so the temperatures are well coupled only after firehose is triggered). As a result, as turbulence is dissipated into particle heat, those components increase together, which causes slow growth of the average magnetic moment. In our simulation setup, kinetic energy is constantly injected into the box, so we expect such an increase in average magnetic moment to continue indefinitely. The changes of the magnetic moments of some individual particles are much more rapid, as we discuss in Sec. III E.

C. Energy transfer in high-β turbulence

The results we describe in the previous sections suggest that collisionless high-β turbulence contains a superposition of local interactions (a Kolmogorov-like cascade from large to small scales) and nonlocal processes mediated by kinetic microinstabilities (mirror and AIC during the driving stage, and firehose in the quasisteady state). In this section, we explore the relative importance of different energy-transfer channels. To do that, we calculate various "transfer functions" that diagnose quantitatively the scale-to-scale transfer of energy in the turbulence caused by different bulk forces [87,88]. A detailed derivation of these diagnostics is given in Appendix B. In brief, the equations for the bulk kinetic, thermal, and magnetic energies are written in a form that makes explicit the transfer of energy between different "reservoirs" of energy and different wave numbers. These reservoirs are defined as vector fields $\boldsymbol{a}$ with associated energy $\boldsymbol{a}^2/2$. For the bulk kinetic energy, the corresponding vector field is $\boldsymbol{a}^u \equiv \sqrt{\varrho}\boldsymbol{u}$; for the magnetic energy it is $\boldsymbol{a}^B \equiv \boldsymbol{B}/\sqrt{4\pi}$. For the thermal energy, multiple definitions are possible. In this paper, we choose $\boldsymbol{a}^{\Delta p} \equiv \sqrt{|\Delta p|}\hat{\boldsymbol{b}}$, so that the viscous stress in the momentum equation may be written as $\boldsymbol{a}^{\Delta p}\boldsymbol{a}^{\Delta p}$, similar to the Maxwell stress. Only the part of the thermal energy associated with Δ ("anisotropic thermal energy") is included in our definition of $\boldsymbol{a}^{\Delta p}$; the remaining part of thermal energy, "isotropic thermal energy," is equal to $3p_\perp/2$. Our definition of $\boldsymbol{a}^{\Delta p}$ is also consistent with the expression for the free energy in the "kinetic reduced MHD" limit (i.e., the long-wavelength limit of gyrokinetics) [46]:

$$\begin{aligned} W^\Delta_{\mathrm{KRMHD}} &= \frac{B_0^2}{8\pi}\int \beta_{\parallel,i}\frac{\Delta_i}{2}\frac{\delta B_\perp^2}{B_0^2}\,d^3\boldsymbol{x} \\ &= \frac{B_0^2}{8\pi}\int \vartheta_{\Delta p}\frac{(\delta\boldsymbol{a}^{\Delta p})^2}{2}\,d^3\boldsymbol{x}, \quad (19) \end{aligned}$$

where $\vartheta_{\Delta p} \equiv \mathrm{sgn}(\Delta p)$, $\delta\hat{\boldsymbol{b}} = \delta\boldsymbol{B}_\perp/B_0 \ll 1$, and the pressure anisotropy is assumed to have an absolute value much larger than its fluctuation due to $\delta\boldsymbol{B}$ [viz., $\Delta_i = \overline{\Delta_i} + \mathcal{O}(|\delta\hat{\boldsymbol{b}}|^2)$], which allows us to neglect terms

proportional to $\delta\Delta_i^2$ and $\delta\Delta_i\delta B_\perp$ and write $\delta\boldsymbol{a}^{\Delta p} = \sqrt{|\Delta p|}\delta\hat{\boldsymbol{b}}]$. The definition of $\boldsymbol{a}^{\Delta p}$ contains the absolute value of the pressure anisotropy. Such a choice was made from a purely technical standpoint, in order to avoid imaginary values when computing this vector at each point of the simulation domain. This choice also forces us to include the sign of Δp in various expressions, such as in Eq. (19), which can make results hard to interpret if $\vartheta_{\Delta p}$ changes significantly throughout the domain. Fortunately, as we show in Fig. 5, most of the domain has negative pressure anisotropy, and the volume fraction with positive Δp is small.

Given the definitions of the energy reservoirs, some terms in the equation for the bulk kinetic energy can be written in the form of shell-to-shell transfer functions. The most important transfer functions in that equation are the transfer function due to the Reynolds stress,

$$\mathcal{T}^{\mathrm{Re}}_{q_\perp \to k_\perp} \equiv -\int \langle\boldsymbol{a}^u\rangle_{k_\perp} \cdot \boldsymbol{u} \cdot \boldsymbol{\nabla}\langle\boldsymbol{a}^u\rangle_{q_\perp}\,d^3\boldsymbol{x}, \quad (20)$$

the transfer function due to the Maxwell stress,

$$\mathcal{T}^{\mathrm{Max}}_{q_\perp \to k_\perp} \equiv \int \langle\boldsymbol{a}^u\rangle_{k_\perp} \cdot \frac{\boldsymbol{B}}{\sqrt{4\pi\varrho}} \cdot \boldsymbol{\nabla}\langle\boldsymbol{a}^B\rangle_{q_\perp}\,d^3\boldsymbol{x}, \quad (21)$$

and the transfer function due to the anisotropic viscous stress,

$$\mathcal{T}^{\mathrm{visc}}_{q_\perp \to k_\perp} \equiv \int \langle\boldsymbol{a}^u\rangle_{k_\perp} \cdot \vartheta_{\Delta p}\sqrt{\frac{|\Delta p|}{\varrho}}\hat{\boldsymbol{b}} \cdot \boldsymbol{\nabla}\langle\boldsymbol{a}^{\Delta p}\rangle_{q_\perp}\,d^3\boldsymbol{x}. \quad (22)$$

Each of these transfer functions represents the rate of energy transfer between fluctuations whose wave numbers lie within the logarithmic perpendicular-wave-number shells centered on $q_\perp$ and $k_\perp$ (from kinetic to kinetic in the case of $\mathcal{T}^{\mathrm{Re}}$, from magnetic to kinetic for $\mathcal{T}^{\mathrm{Max}}$, and from anisotropic thermal energy to kinetic for $\mathcal{T}^{\mathrm{visc}}$).

Figure 7 shows the flow of kinetic energy through Fourier space as calculated by the transfer functions [Eqs. (20)–(22)] in the two-dimensional plane of wave numbers $q_\perp$ and $k_\perp$ in quasisteady state of $\beta_{i0} = 16$ simulation at $\Omega_{i0}t = 6000$. Results from the same diagnostic obtained during earlier stages of this simulation are in Appendix B, Fig. 18. The sign of the transfer terms in Fig. 7 represents the change in bulk kinetic energy in shell $k_\perp$. In the early stages of the simulation, including the mirror, AIC and the Landau-damping stages, the transfers are mostly local, and are similar to those found previously in simulations of MHD turbulence [88]. In contrast, in the quasisteady state, there is considerable nonlocal energy transfer associated with the Maxwell and viscous stresses [see the $q_\perp > k_\perp$ part of Figs. 7(b) and 7(c)]. This nonlocal transfer takes energy from the large-scale fluid motions and transfers it into small-scale magnetic fields, as
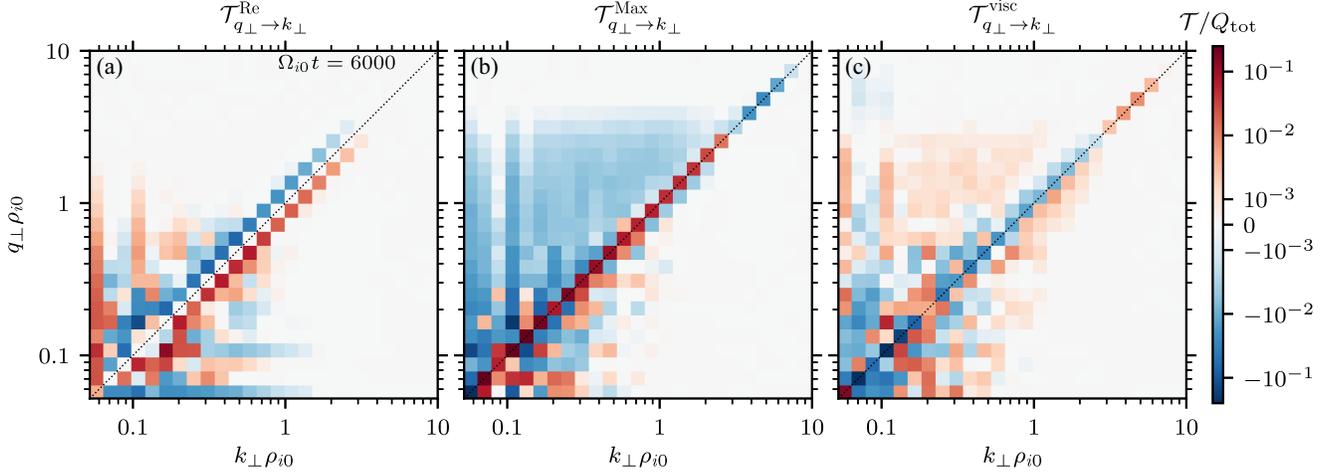
FIG. 7.   Energy-transfer functions [Eqs. (20)–(22)] due to the Reynolds (a), Maxwell (b), and viscous stresses (c) in the quasisteady state of our $\beta_{i0} = 16$ simulation. There is a considerable amount of nonlocal energy transfer due to the firehose instability, which is not present during the early stages of the simulation (see Appendix B for an analogous plot featuring the earlier stages).

is expected from the firehose instability. We thus conclude that kinetic microinstabilities are active even in the quasisteady state and that they contribute a non-negligible amount of energy transfer. Out of the three instabilities that we see in our simulations, the one most responsible for the nonlocal energy transfer appears to be the firehose, as this nonlocal transfer becomes competitive with the local transfers only after the box-averaged pressure anisotropy approaches the firehose threshold and localized patches of the plasma exceed that threshold. The viscous stress in the quasisteady state has both local and nonlocal components, which we discuss in more detail in Sec. III F, and is mostly negative, indicating that the viscous stress mostly removes energy from the bulk motions. This transfer causes the conversion of energy between bulk kinetic and anisotropic thermal energies, and subsequently steepens the kinetic-energy spectrum (as we show in Sec. III D).

The energy transfer quantified by the transfer functions Eqs. (20)–(22) is, in principle, reversible. Indeed, for any energy transfer term of the form $\boldsymbol{a}_1 \cdot \boldsymbol{f} \cdot \boldsymbol{\nabla} \boldsymbol{a}_2$ for some vector field $\boldsymbol{f}$, there is another term of the form $\boldsymbol{a}_2 \cdot \boldsymbol{f} \cdot \boldsymbol{\nabla} \boldsymbol{a}_1$ (see Appendix B for the transfer terms in the induction equation and in the equation for Δp). The total energy transfer due to such terms,

$$\sum_{k_\perp, q_\perp} \mathcal{T}^{a_1 \to a_2}_{q_\perp \to k_\perp} + \mathcal{T}^{a_2 \to a_1}_{q_\perp \to k_\perp} = \int (\boldsymbol{a}_1 \cdot \boldsymbol{f} \cdot \boldsymbol{\nabla} \boldsymbol{a}_2 + \boldsymbol{a}_2 \cdot \boldsymbol{f} \cdot \boldsymbol{\nabla} \boldsymbol{a}_1) d^3\boldsymbol{x}$$

$$= \int \boldsymbol{f} \cdot \boldsymbol{\nabla} (\boldsymbol{a}_1 \cdot \boldsymbol{a}_2) d^3\boldsymbol{x}$$

$$= - \int (\boldsymbol{a}_1 \cdot \boldsymbol{a}_2) \boldsymbol{\nabla} \cdot \boldsymbol{f} \, d^3\boldsymbol{x}, \qquad (23)$$

is zero if $\boldsymbol{\nabla} \cdot \boldsymbol{f}$ is zero, which is one of the assumptions we are making in our transfer-function analysis. We check this

assumption *a posteriori* in Appendix B by computing "compressive" terms and comparing them to "advection-like" terms such as Eqs. (20)–(22). Although Eq. (23) is valid for arbitrary $\boldsymbol{f}$, this vector in practice is proportional to $\boldsymbol{u}$ or $\boldsymbol{B}$. We refer the reader to Appendix B, and Fig. 18 in particular, for more information. One of the terms, which we do not consider explicitly, is the transfer of energy due to an effective collisionality [i.e., the last term in Eq. (6)]. This term is quite important in the quasisteady state, as it is responsible for the conversion of energy between the anisotropic ($\Delta p/2$) and isotropic ($3p_\perp/2$) thermal energies: it reduces the pressure anisotropy and leads to irreversible heating. It is not feasible to compute this term directly in our simulations because, unlike the last term of Eq. (6), the effective collisionality in our runs comes from wave-particle interactions and its analysis requires computation of high-order moments of the distribution function. The only other irreversible term is resistive dissipation, which we find to be relatively less important.

D. Effective viscous scale and subviscous turbulence

In Sec. II we argue that, in critically balanced turbulence, the effective viscous scale associated with scattering by ion-Larmor-scale kinetic instabilities satisfies $\ell_\nu \sim L M_A^{-3}$. This means that, for our simulations with $M_A \lesssim 1$, the viscous scale is expected to be close to, or, formally speaking, even above, the driving scale. Formally, we define the viscous scale as the scale at which the pressure anisotropy peaks. We obtain this scale in a way analogous to the regular energy-containing scale of the turbulence: if the velocity field has a spectrum of $\mathcal{E}_{\boldsymbol{u}}(k_\perp)$, then the energy-containing scale corresponds to the peak of $\delta u_k^2 \sim k_\perp \mathcal{E}_{\boldsymbol{u}}(k_\perp)$. For the viscosity, this means that the effective viscous scale $\ell_{\nu,\mathrm{eff}}$ corresponds to the value of $k_\perp$ at which the spectrum of pressure anisotropy $\mathcal{E}_{\Delta p}$ has a slope of -1. It is possible to
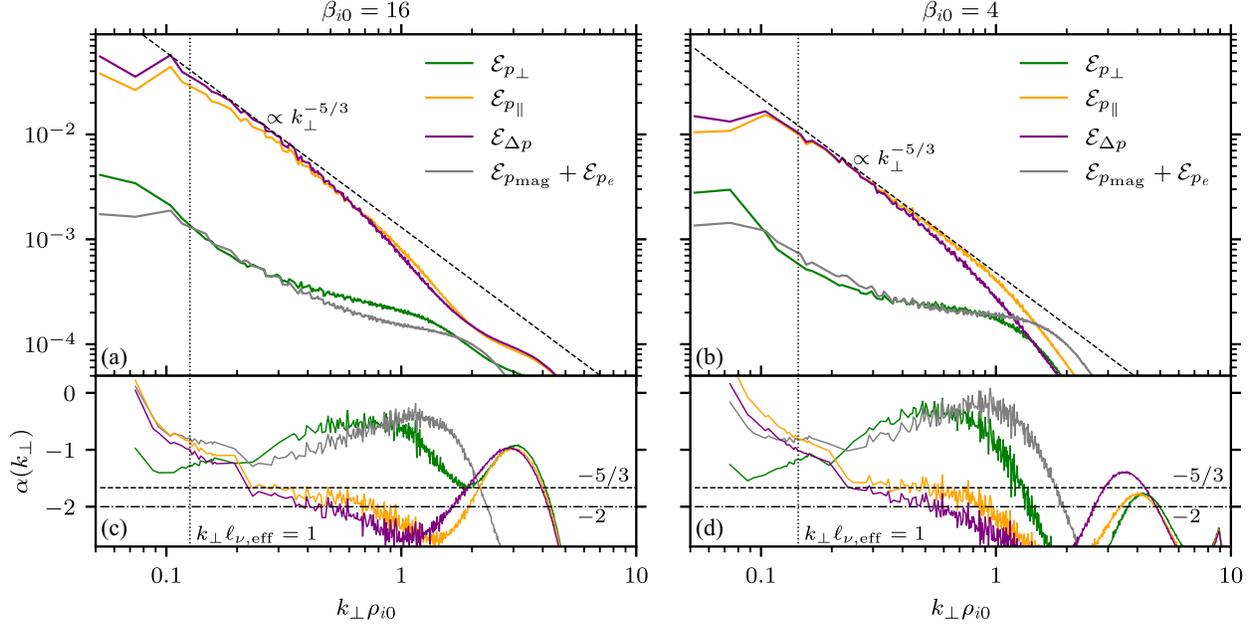
FIG. 8. (a),(b) Spectra of parallel (orange) and perpendicular (green) pressures, pressure anisotropy (purple), and the sum of electron pressure and magnetic pressure (gray). We define the effective viscous scale $\ell_{\nu,\mathrm{eff}}$ as the scale at which the pressure anisotropy fluctuation amplitude $\sim k_\perp^{1/2}\Delta p_k$ peaks. This scale is close to the driving scale, in line with the analytical prediction of Sec. II. (c),(d) Spectral indices as a function of wave number for the spectra from upper panels.

define the effective viscous scale in other ways, e.g., by looking at the k-space peak of viscous dissipation. We do not use such a definition because of the nonlocal nature of the viscous dissipation (e.g., the spatial scale at which most of the kinetic energy is removed is not necessarily the same as the scale at which most of the thermal energy is deposited; see Sec. III C).

Figure 8 shows the spectra of the parallel and perpendicular pressures, as well as of the pressure anisotropy, in the quasisteady state of the $\beta_{i0} = 16$ and $\beta_{i0} = 4$ simulations. The effective viscous scale for each simulation is indicated by a vertical dashed line: at $k_\perp \rho_{i0} \approx 0.126$ for $\beta_{i0} = 16$ and at $k_\perp \rho_{i0} \approx 0.144$ for $\beta_{i0} = 4$. These scales are close to the outer scale of the turbulence, consistent with the expectations presented in Sec. II. An interesting feature seen in Fig. 8 is that the parallel-pressure spectrum is much larger in magnitude than the perpendicular-pressure spectrum. This difference may be explained as follows. If we assume perpendicular pressure balance, which is a natural outcome in high-β anisotropic turbulence [13,46], and is also observed in our simulations (gray lines in Fig. 8 correspond to the sum of electron pressure, $p_e = n_e T_e = n_i T_{i0}$, and magnetic pressure, $p_{\mathrm{mag}} = B^2/8\pi$), that would imply $p_\perp + B^2/8\pi \approx$ const, and therefore $\delta p_\perp \sim -\delta B^2/8\pi$. At the same time, pressure anisotropy at subviscous scales (where the effective collisionality is less important [89]) behaves nearly adiabatically: $d\Delta p/dt \sim pd\ln|B|/dt$. This leads to pressure-anisotropy fluctuation of $\delta \Delta p \sim \beta \delta B^2 \gg \delta B^2 \sim \delta p_\perp$, and therefore $\delta p_\parallel \gg \delta p_\perp$. In the subviscous range, $\delta p_\parallel$ is passively advected, its spectrum has a similar slope to δu_k, and the parallel pressure remains larger than the perpendicular pressure throughout the subviscous range. Landau damping, viscous heating, and pitch-angle scattering off microfluctuations produced by kinetic microinstabilities gives rise to large-scale fluctuations of $\delta p_\parallel$ to achieve a value of pressure anisotropy close to $\nu_{\mathrm{eff}}^{-1}\hat{\boldsymbol{b}}\hat{\boldsymbol{b}}:\boldsymbol{\nabla u}$.

To examine how the effective viscosity affects the cascade, we plot in Fig. 9 the quasisteady-state spectra of magnetic energy (blue) and bulk kinetic energy (red) from both simulations. The magnetic-energy spectra have larger amplitudes than the kinetic-energy spectra at the driving scales due to changes in the effective Alfvén speed caused by the mean negative pressure anisotropy in the box (cf. Fig. 5). These spectra have similar slopes above the viscous scale. The kinetic-energy spectrum is steeper than $-5/3$ (close to -2), which is an indication of the viscous dissipation. Below the viscous scale, the kinetic-energy spectrum continues to steepen because of the subviscous ion heating (see Sec. III F for more details on ion heating). In contrast, the magnetic-energy spectrum becomes shallower. We attribute this flattening to small-scale energy injection by kinetic microinstabilities [90]. Given that the majority of the simulation box is near the threshold for the firehose instability (see Fig. 5), we interpret this bump in the magnetic-energy spectrum as the spectrum of the firehose fluctuations.

The deviation of the magnetic spectrum from the kinetic spectrum at sub-parallel-viscous scales indicates
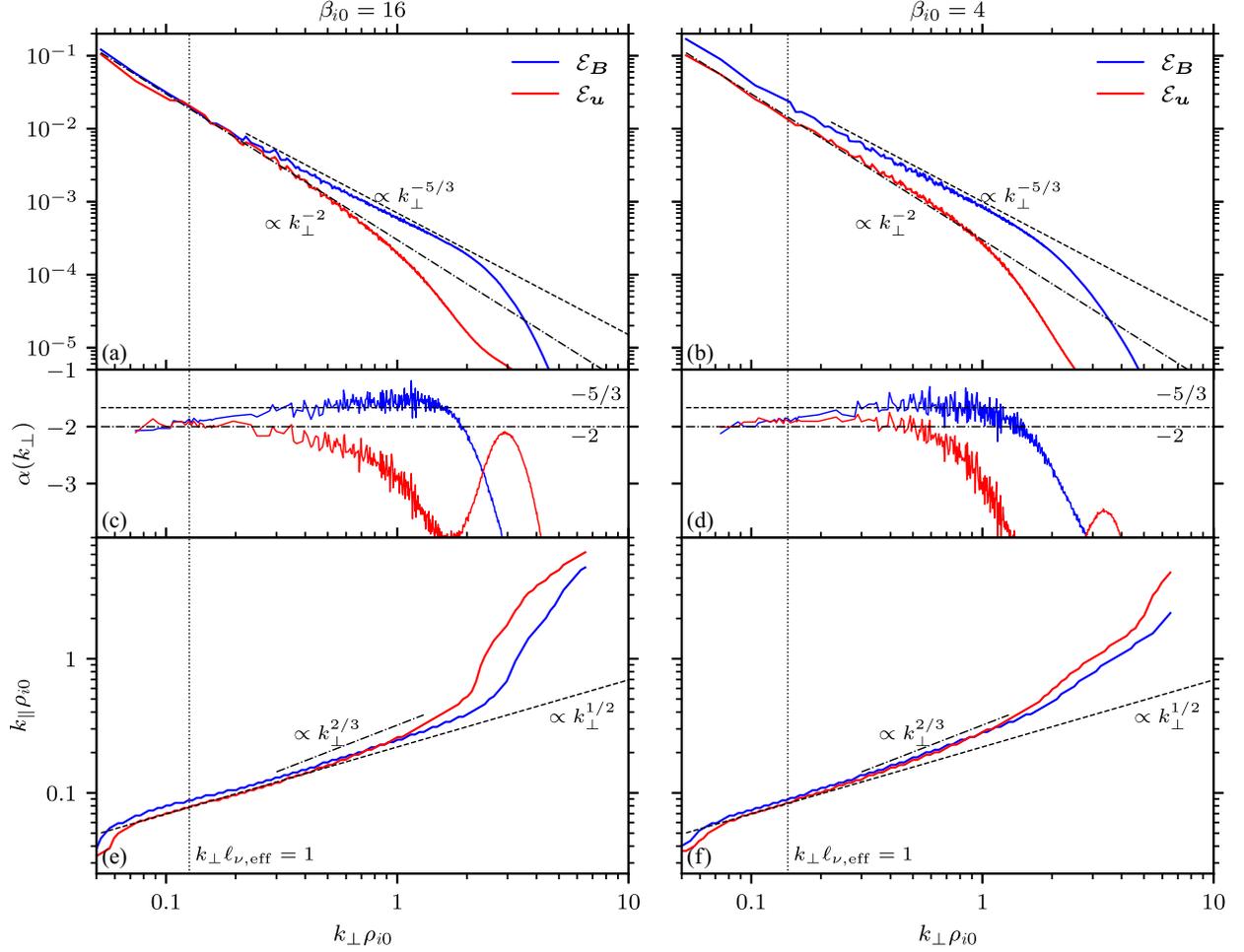
FIG. 9. (a),(b) Quasisteady-state spectra of magnetic (blue) and kinetic (red) energies in the $\beta_{i0} = 16$ (a) and $\beta_{i0} = 4$ (b) simulations. These spectra have similar slopes near the driving scale, but deviate from one another at scales below the effective viscous scale (defined in Sec. III D and in the caption of Fig. 8, and indicated by the dotted lines). The kinetic-energy spectra are steeper than $-5/3$ because of the anisotropic viscous stress; the slope of the kinetic-energy spectrum becomes close to -2. The magnetic-energy spectrum becomes shallower toward $k_\perp \rho_{i0} \sim 1$ because firehose fluctuations are injected at these scales in the quasisteady state. (c),(d) Spectral indices as functions of wave number for the magnetic- and kinetic-energy spectra. (e),(f) Parallel wave number ($k_\parallel$) of the fluctuations as a function of their perpendicular wave number ($k_\perp$) obtained from magnetic-field structure-function analysis. The value of spectral anisotropy $k_\parallel / k_\perp$ agrees with critical-balance predictions.

an important feature of high-β turbulence: the small-scale firehose fluctuations are decoupled from the Alfvénic cascade. To illustrate this point, we plot in Figs. 9(e) and 9(f) the wave number anisotropy $k_\parallel(k_\perp)$ for δu and δB fluctuations. This dependence is computed using the values of the quasisteady-state structure functions at $\ell = \ell_\perp$ and $\ell = \ell_\parallel$. The wave number anisotropy appears to have a scaling of $k_\parallel \propto k_\perp^{1/2}$ in the inertial range, consistent with critical balance:

$$k_\parallel v_A \sim k_\perp \delta u_\perp \propto k_\perp^{3/2} \mathcal{E}_u^{1/2} \propto k_\perp^{1/2}, \qquad (24)$$

where in the final step we adopt a $k_\perp^{-2}$ spectrum. It is interesting that this critical balance is measured to hold at what are notionally sub-parallel-viscous scales, which

suggests that the viscous backreaction on the cascade is not purely dissipative. The anisotropy computed using the magnetic-field fluctuations has the same scaling, despite the magnetic energy having a shallower spectrum. This means that the firehose modes, which are oblique and affect neither the parallel nor the perpendicular structure functions, do not participate in the critically balanced cascade. The magnetic spectrum is a superposition of the critically balanced cascade with a slope close to -2 and an additional spectrum of the firehose fluctuations, which peaks at kinetic scales. Independence of the firehose fluctuations from the Alfvénic cascade has also been shown by Ref. [45] using an expanding box, in which the dominant contribution to the pressure anisotropy is from plasma expansion perpendicular to the mean field (rather than from the fluctuations).
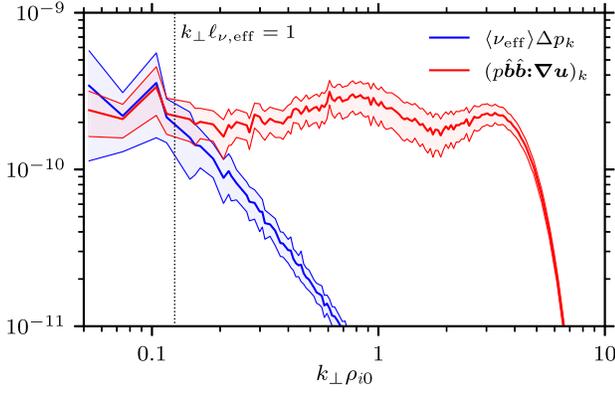
FIG. 10. Comparison between the spectra of pressure anisotropy (blue lines) and $p\hat{\boldsymbol{b}}\hat{\boldsymbol{b}}\!:\!\boldsymbol{\nabla u}$ (red lines), the latter of which is proportional to the rate of growth of the magnetic field [see Eq. (6)]. Above the effective viscous scale $\ell_{\nu,\mathrm{eff}}$ (vertical dotted line), the pressure anisotropy is proportional to $p\hat{\boldsymbol{b}}\hat{\boldsymbol{b}}\!:\!\boldsymbol{\nabla u}$. The proportionality coefficient between the two (the "Braginskii estimate" for the effective collision frequency) is $\langle\nu_{\mathrm{eff}}\rangle\sim 0.01\Omega_{i0}$. At scales smaller than $\ell_{\nu,\mathrm{eff}}$, this effective collisionality is not large enough relative to the dynamical frequencies, so the pressure anisotropy deviates significantly from the Braginskii estimate. Note the bump in $\hat{\boldsymbol{b}}\hat{\boldsymbol{b}}\!:\!\boldsymbol{\nabla u}$ near $k_\perp\rho_{i0}\sim 1$, which corresponds to firehose fluctuations in quasisteady state (the additional peak at $k_\perp\rho_{i0}\approx 3$ is due to particle noise).

E. Effective collisionality

In this section, we estimate the effective collisionality from the results of our hybrid-kinetic simulations. For that, we use two independent methods: one based on the evolution of the pressure stress in the simulations (Sec. III E 1) and one based on the motion of individual particles (Sec. III E 2).

1. Effective collisionality from pressure-stress evolution

In Sec. II, we employ a simple model [Eq. (6)], where pressure anisotropy grows with the local parallel rate of strain $S\equiv\hat{\boldsymbol{b}}\hat{\boldsymbol{b}}\!:\!\boldsymbol{\nabla u}$ and is relaxed by Coulomb collisions between particles at the rate ν. A common assumption in reduced fluid models, such as Braginskii MHD, is that the typical frequency of fluctuations satisfies $\omega\ll\nu$, so $d\Delta/dt$ is much smaller than other terms in Eq. (6). Then $\Delta\simeq S/\nu$. To test whether such a closure works in kinetic high-β turbulence, we plot in Fig. 10 the spectra of Δp (blue) and $p\hat{\boldsymbol{b}}\hat{\boldsymbol{b}}\!:\!\boldsymbol{\nabla u}$ (red). The spectrum of pressure anisotropy is multiplied by a coefficient $\langle\nu_{\mathrm{eff}}\rangle\sim 0.01\Omega_{i0}$, which is the value of $(p\hat{\boldsymbol{b}}\hat{\boldsymbol{b}}\!:\!\boldsymbol{\nabla u})_k/\Delta p_k$ averaged over scales satisfying $k_\perp\ell_{\nu,\mathrm{eff}}<1$. In what follows, we refer to the latter [which we also label as $(p\hat{\boldsymbol{b}}\hat{\boldsymbol{b}}\!:\!\boldsymbol{\nabla u})_L/\Delta p_L$] as the "Braginskii estimate," because the pressure anisotropy in a weakly collisional plasma when the fluid motions are incompressible is given by Braginskii [43] as $\Delta p=p\hat{\boldsymbol{b}}\hat{\boldsymbol{b}}\!:\!\boldsymbol{\nabla u}/\nu$.

ν_{eff} represents our approximation for the effective collisionality, which in our simulations is mediated by wave-particle interactions [91]. Shaded regions in Fig. 10 indicate root-mean-square fluctuations in pressure anisotropy and rate of strain measured during the quasisteady state. The pressure-anisotropy spectrum follows the rate of strain down to the viscous scale, below which the pressure anisotropy starts to decrease while the parallel rate of strain increases. This increase corresponds to the injection of small-scale firehose fluctuations in quasisteady state.

Despite their being comparable in magnitude, $p\hat{\boldsymbol{b}}\hat{\boldsymbol{b}}\!:\!\boldsymbol{\nabla u}$ and $\nu_{\mathrm{eff}}\Delta p$ are not directly proportional to one another, as in the standard Braginskii closure. Instead, there is a phase difference between the two, a feature that may be explained as follows. If the local rate of strain behaves as $S(t)=S_0\exp(-i\omega t)$, and $\Delta(t=0)=0$, then Eq. (6) has the simple solution

$$\Delta(t)=\frac{3S_0}{-i\omega+3\nu}e^{-i\omega t}=\frac{S(t)}{\sqrt{\nu^2+\omega^2/9}}e^{i\phi}, \quad (25)$$

where $\cos\phi=\nu/\sqrt{\nu^2+\omega^2/9}$ and ϕ is the phase lag between the pressure anisotropy and the rate of strain. This phase lag is relatively small at the injection scale, where $\nu\sim\beta\omega\gg\omega$, but becomes increasingly larger toward the smaller scales. Nonzero phase lag makes the energy transfer due to effective viscosity non-sign-definite, and makes the behavior of kinetic plasma different from a Braginskii-MHD plasma.

Another effect neglected in the Braginskii model is the growth of small-scale magnetic fields associated with kinetic microinstabilities (mostly firehose). Kinetic instabilities increase the ion-Larmor-scale contribution to the shear $\hat{\boldsymbol{b}}\hat{\boldsymbol{b}}\!:\!\boldsymbol{\nabla u}$ and cause it to deviate from Δp. Structure-function analysis of the rates of strain (not shown) suggests that $\hat{\boldsymbol{b}}\hat{\boldsymbol{b}}\!:\!\boldsymbol{\nabla u}$ peaks at $k_\parallel\rho_{i0}\approx k_\perp\rho_{i0}\approx 0.4$, which corresponds to the wave number of fastest growth for the oblique firehose instability [24].

2. Effective collisionality from particle motion

Figure 10 provides just one way of estimating the effective collisionality of an (otherwise collisionless) high-β plasma. This method relies on the assumption that pressure anisotropy evolves according to Eq. (6), which is not necessarily true if strong heat fluxes are present. To provide an independent measurement of the effective collisionality, we examine to what extent the magnetic moments μ of the particles are conserved. In the absence of scattering, the only way to change μ is through nonadiabatic heating or cooling. Although there has not yet been a self-consistent study of heating in collisionless high-β plasmas, existing studies suggest that nonadiabatic heating is small; e.g., stochastic heating is suppressed at $\beta\gg 1$ [80,92]. Additionally, in the absence of pressure
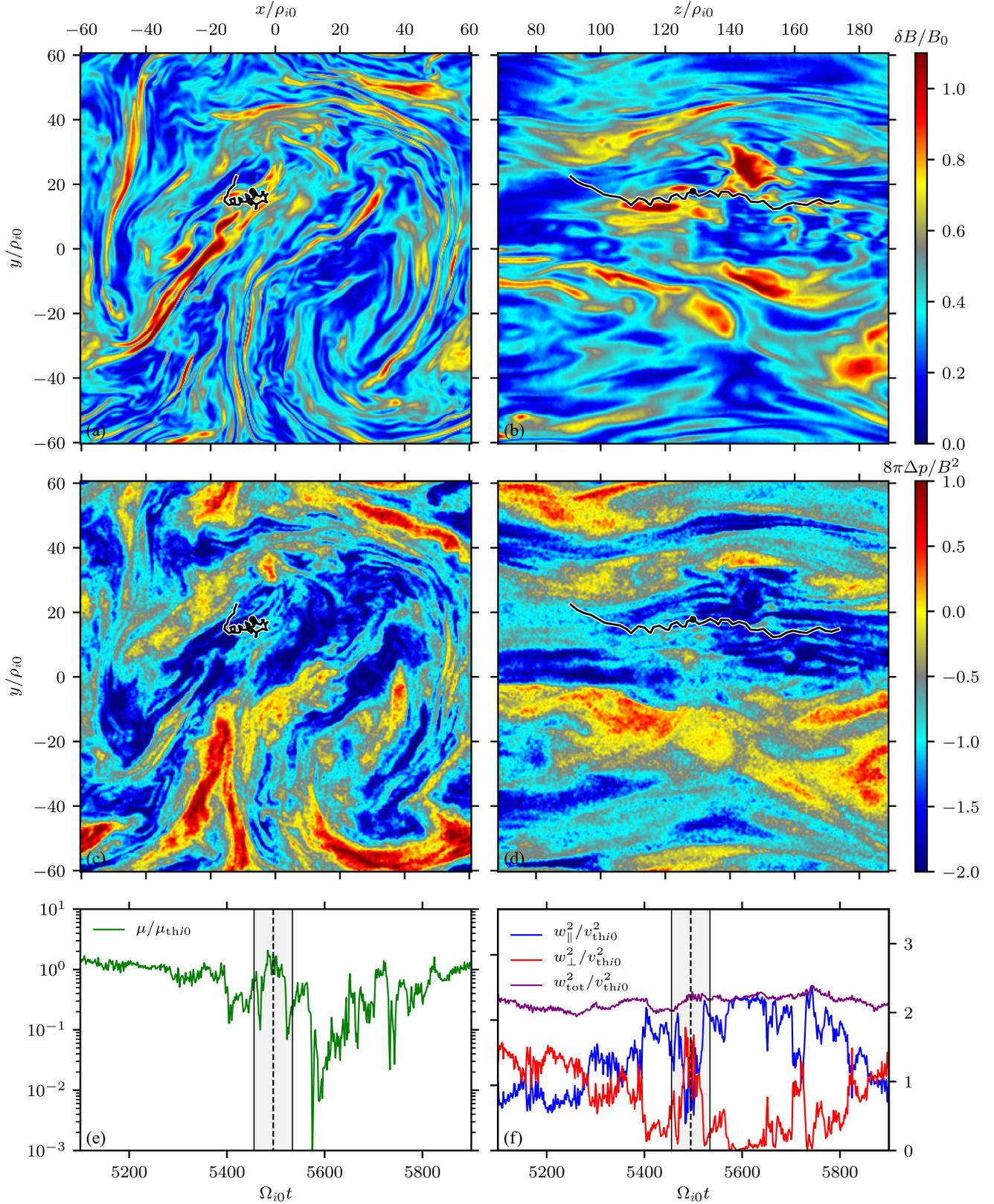
FIG. 11. Trajectory of a tracked particle from the $\beta_{i0} = 16$ simulation with single-mode driving (see Sec. III A 3). This particle moves through a region with firehose-unstable pressure anisotropy (c),(d). The same region shows small-scale oblique magnetic-field fluctuations (a),(b), which we interpret as firehose modes. As the particle passes through the region, its magnetic moment starts to break (e), and it experiences pitch-angle scattering at almost constant total energy (f). The gray shaded regions in (e) and (f) indicate the period of time over which the trajectory in (a)–(d) is plotted.
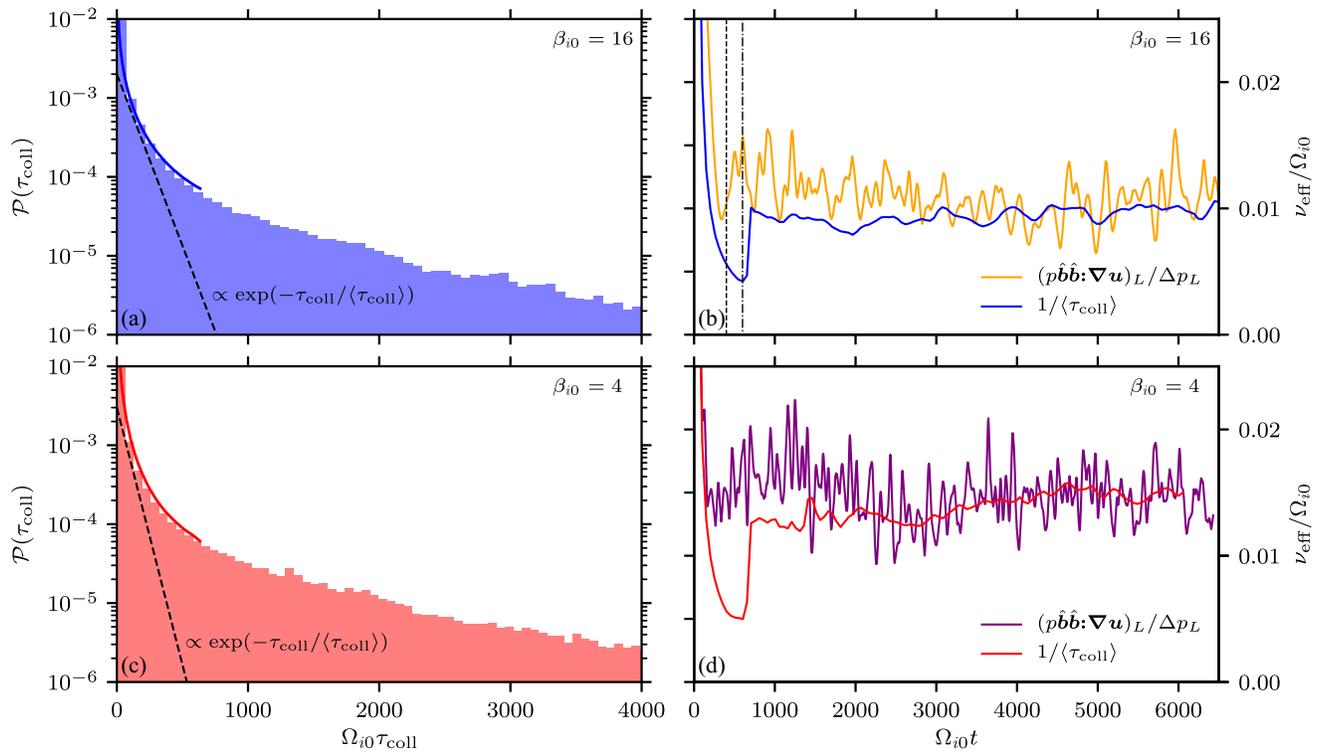
FIG. 12.   Histograms of collision times of tracked particles in the $\beta_{i0} = 16$ (a) and $\beta_{i0} = 4$ (c) simulations averaged over the duration of the simulations. Solid lines denote the probabilities obtained with the collisionality diagnostic described in Sec. III E, which uses all particles in the simulation (Sec. III E 2). (b),(d) Comparison of effective collisionalities obtained by computing Δp_k and $(p\hat{\boldsymbol{b}}\hat{\boldsymbol{b}}:\boldsymbol{\nabla}\boldsymbol{u})_k$ at large scales ($k_\perp \ell_{\nu,\mathrm{eff}} < 1$; see Fig. 10) and those obtained from $\langle \tau_{\mathrm{coll}} \rangle$ based on the distributions in (a) and (c). A good agreement between these independent methods indicates that the collisionality is similar to the Braginskii estimate [Eq. (26)]. Vertical dashed and dot-dashed lines in (b) show the values of time for the snapshots in Figs. 16 and 17.

anisotropy, Landau damping can dissipate a significant portion of the cascade [78], leaving little energy for additional nonadiabatic channels.

An example of this process is shown in Fig. 11. The black lines in Figs. 11(a)–11(d) show the trajectory of a particle from the $\beta_{i0} = 16$ simulation (see Sec. III A 3) in the planes perpendicular and parallel to the guide field, plotted over a snapshot of fluctuations in magnetic-field strength [Figs. 11(a) and 11(b)] and in pressure anisotropy [Figs. 11(c) and 11(d)]. The fluctuations themselves evolve over time, while Figs. 11(a)–11(d) only show them at a fixed moment; this should not present a problem of interpretation given that, at high plasma β, the fluctuations evolve much more slowly than the particles stream across them $(k_\parallel v_A \ll k_\parallel v_{\mathrm{th}})$. This particular particle has been chosen because it moves through a region with firehose-unstable pressure anisotropy, and the magnetic-field slices exhibit clear firehose fluctuations. These fluctuations cause the particle's magnetic moment to break by pitch-angle scattering [Fig. 11(e)], during which the total energy of the particle is almost constant [Fig. 11(f)].

One way of measuring collisionality from particle trajectories is to look at the particles' magnetic moments as functions of time and compute a histogram of times τ_{coll}

needed for the magnetic moment of each tracked particle to change by one factor of e. In Figs. 12(a) and 12(c), we show such a histogram, computed using the trajectories of $> 10^4$ tracked particles from our $\beta_{i0} = 16$ and $\beta_{i0} = 4$ simulations. Solid lines in this figure show the distribution functions of τ_{coll}, but evaluated during the simulation time using all available particles ($> 10^{11}$ particles in total) [93]. These solid lines are then used to evaluate $\langle \tau_{\mathrm{coll}} \rangle$ at different times during the simulations. The effective collisionality is then obtained as $\nu_{\mathrm{eff}} = 1/\langle \tau_{\mathrm{coll}} \rangle$. We use $1/\langle \tau_{\mathrm{coll}} \rangle$ as a definition of the effective collisionality because it is the maximum likelihood estimator for an exponential distribution (which is our hypothesis for collision events). Figures 12(b) and 12(d) compare the effective collisionalities computed in this manner with those computed from the ratio of rate of strain and pressure anisotropy at large scales $L \gtrsim \ell_{\nu,\mathrm{eff}}$ (Sec. III E 1).

In the beginning of each simulation, the collisionality is smaller than the Braginskii estimate, which is to be expected because the simulation is not yet in quasisteady state. After the microinstabilities are triggered [vertical dashed and dot-dashed lines in Fig. 12(b)], the collisionality grows rapidly, and its value in quasisteady state is consistent with the Braginskii estimate. The values of

collisionality are also consistent with our expectations from Sec. II. Namely, for $\beta_{i0} = 16$,

$$\nu_{\rm eff} \sim \beta_{i0}\hat{\boldsymbol{b}}\hat{\boldsymbol{b}} : \boldsymbol{\nabla}\boldsymbol{u}|_{\max} \sim \beta_{i0}M_A^3\frac{v_{A0}}{L_\perp} \approx 0.01\Omega_{i0}. \quad (26)$$

Although the collisionality is expected to scale proportionally to $\sqrt{\beta_{i0}}$ [based on Eq. (26) with $L_\perp \propto \rho_{i0}$], we find a larger value of collisionality in the $\beta_{i0} = 4$ simulation than in the $\beta_{i0} = 16$ simulation. We attribute this to differences between Mach numbers and the quasisteady-state pressure anisotropies in the simulations (the $\beta_{i0} = 4$ simulation ends up closer to the firehose threshold; see Fig. 5). If positive pressure anisotropies are mediated by the AIC instability with threshold $\propto 1/\sqrt{\beta}$, then $\nu_{\rm eff} = \sqrt{\beta_{i0}}\hat{\boldsymbol{b}}\hat{\boldsymbol{b}} : \boldsymbol{\nabla}\boldsymbol{u}|_{\max}$, and thus both runs should have the same collisionality. However, our simulations are continuously driven, and after a long enough time, the firehose instability is triggered, which increases the collisionality to $\beta_{i0}\hat{\boldsymbol{b}}\hat{\boldsymbol{b}} : \boldsymbol{\nabla}\boldsymbol{u}|_{\max}$.

F. Ion heating

In Sec. II, we present theoretical arguments, subsequently supported by our numerical results presented in Secs. III D and III E, that suggest that the viscous scale in collisionless high-β turbulence is close to the outer scale. Here we ask whether this means that most of the heating happens at the effective viscous scale, rather than at kinetic scales. Heating close to kinetic scales has been found numerically in low-β kinetic turbulence [79,80,94], and also in gyrokinetic simulations of high-β turbulence [78]. In the latter, it came from the Landau damping of Alfvén waves, expected to peak at a scale [44,78,95]

$$\rho_\star \equiv (3/4\pi^{1/4}\sqrt{2})\beta_i^{1/4}\rho_i. \quad (27)$$

Both low-β simulations and gyrokinetic studies lack dynamically important viscous stresses, which can cause a significant portion of the cascade to be dissipated at the viscous scale. The precise amount of such dissipation might be difficult to estimate given the dynamical backreaction of the parallel-viscous stress, which tends to rearrange fields so as to reduce the amount of parallel-viscous heating [7,55]. In this section, we ask whether most of the heating happens at small scales due to Landau damping or at large scales due to the pressure-anisotropic viscous stress, and show that the latter is the case in our simulations.

We first note that the velocity spectrum in Fig. 9 has a slope steeper than $-5/3$, instead of closer to -2. There are two potential explanations: either the nonlinear interactions of turbulent eddies are modified in such a way as to steepen the spectrum or the large-scale ion heating causes dissipation of a considerable portion of the cascade energy flux. As we explain in Sec. III D, for the former explanation to be valid, the conservative critically balanced cascade should satisfy $k_\parallel\delta u_k^2 \sim {\rm const}$, which for a $k_\perp^{-2}$ spectrum means that $k_\parallel \propto k_\perp$. As we show in Figs. 6(e) and 6(f), this is not the case, as $k_\parallel$ scales as $k_\perp^{1/2}$ in the quasisteady state. This means that the cascade is not conservative, and some part of the cascade is dissipated as ion heating. Our energy-transfer function for the viscous stress (Fig. 7) also suggests considerable dissipation in the inertial range.

To determine the wave number dependence of the ion heating Q_i, we employ the energy-transfer functions for the thermal-energy equation (see Sec. III C and Appendix B) and separate the total heating into its local ($q_\perp = k_\perp$) and nonlocal ($q_\perp \neq k_\perp$) components averaged over the quasisteady state. These averages are computed from two-dimensional transfer functions by summing over $q_\perp$ shells, $\mathcal{T}_{\rm nonloc} \equiv \sum_{q_\perp \neq k_\perp} \mathcal{T}_{q_\perp \to k_\perp}$ and $\mathcal{T}_{\rm loc} \equiv \mathcal{T}_{k_\perp \to k_\perp}$. Such a definition can, in principle, depend upon the choice of

FIG. 13. The dependence of anisotropic viscous heating $\boldsymbol{\Pi} : \boldsymbol{\nabla}\boldsymbol{u}$ in the $\beta_{i0} = 16$ simulation on time (a) and wave number (b). Heating is separated into local (red line) and nonlocal (blue line) components, as defined in Sec. III F, with total heating indicated by the green dashed line. The purple dot-dashed line denotes the nonlocal transfer from kinetic to magnetic energy, which we attribute to the growth of small-scale firehose fluctuations.

wave number shells; for simplicity, we ignore this dependence, while noting that the local and nonlocal contributions to the transfer functions in Fig. 7 are quite distinct. Figure 13 shows the dependence of local and nonlocal ion heating $\boldsymbol{\Pi}:\boldsymbol{\nabla u}$ on time [Fig. 13(a)] and on perpendicular wave number [Fig. 13(b)] for the $\beta_{i0} = 16$ simulation. The simulation starts with most of $\boldsymbol{\Pi}:\boldsymbol{\nabla u}$ being local. This is the reversible energy transfer between bulk kinetic and thermal energies; indeed, it changes sign several times during this stage of the simulation. After sufficiently negative pressure anisotropy has built up, so that the simulation becomes unstable to the firehose instability, the nonlocal ion heating becomes the dominant component of the energy transfer. During this stage, nonlocal heating approximately follows the nonlocal energy transfer between kinetic and magnetic energies due to firehose instability. In the quasisteady state, there are comparable amounts of local and nonlocal heating, while the effective collisionality makes the transfer of energy due to anisotropic viscosity $\boldsymbol{\Pi}:\boldsymbol{\nabla u}$ irreversible. The quasisteady-state value of $\mathcal{T}_{\text{nonloc}}^{\text{Max}}$ is comparable to, or even larger than, the total heating, which indicates that nonlocal transfer due to firehose growth is comparable to the overall energy flux in the system and that the firehose instability is important in the quasisteady state. We interpret all nonlocal transfer due to magnetic tension ($\mathcal{T}_{\text{nonloc}}^{\text{Max}}$) as firehose growth (see Sec. III C).

The steep spectrum of $dQ_i/dk_\perp$ implies that most of the energy is dissipated at large scales, close to the effective viscous scale (and hence outer scale) of the system. Such dissipation is not present in low-β simulations of collisionless Alfvénic turbulence [79,80], in which heating typically peaks at subion scales. That being said, there is some dissipation at small scales as well: the spectrum of $dQ_i/dk_\perp$ continues even after the cutoff of the kinetic-energy spectrum. There are several heating mechanisms that can operate in this range. Cyclotron heating, which can be important at $\beta \sim 1$ [79], is expected to have a localized peak at the wave number at which the frequency of kinetic Alfvén waves $\omega_{\text{KAW}} \sim \Omega_i$; this behavior is inconsistent with the results in Fig. 13 (assuming Alfvénic nature of sub-ρ_i fluctuations, which is not exactly true if firehose instability is present). Similarly, stochastic heating [80,92,96] is expected to have a localized peak at $k_\perp \rho_{i0} \sim 1$. Both of these mechanisms are expected to be relatively unimportant at $\beta \gg 1$. It is likely that the subviscous dissipation in our high-β simulations is caused instead by Landau damping, which is the dominant energization mechanism seen in gyrokinetic simulations at high β [78]. That being said, the importance of Landau damping changes as the simulation progresses. Figure 14 shows the wave number and velocity dependence of ion energization during three time intervals: the mirror and AIC stages, $\Omega_{i0}t \leq 2000$; the Landau-damping stage, $2000 < \Omega_{i0}t \leq 4000$; and the quasisteady state, $\Omega_{i0}t > 4000$. The first two intervals have considerable heating near $k_\perp \rho_\star \sim 1$ [recall the definition of $\rho_\star$
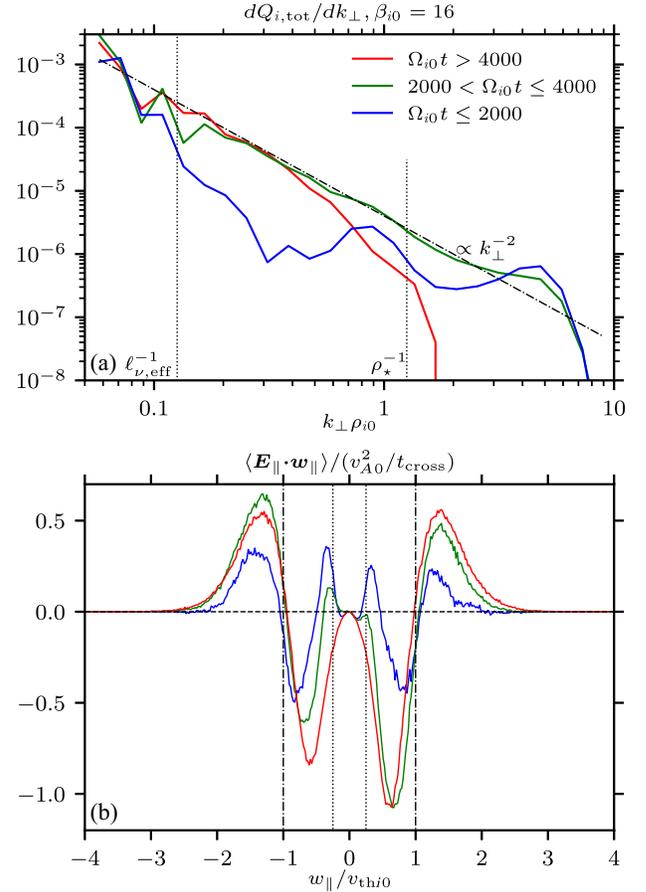
FIG. 14. (a) Wave number dependence of particle energization during three time intervals in the $\beta_{i0} = 16$ simulation. The first two stages have a considerable amount of heating at $k_\perp \rho_\star \sim 1$, where Landau damping is expected to be important. Subviscous heating is suppressed in the quasisteady state, and most of the heating occurs close to the effective viscous scale. (b) Phase-space dependence of parallel energization of particles during the same time intervals. The peaks at $w_\parallel \sim \pm v_{A0}$ (vertical dotted lines), indicative of Landau damping, are present during the early stages, but disappear in the quasisteady state.

given by Eq. (27)]. In contrast, Larmor-scale heating is considerably suppressed in the final stage [97]. The phase-space energization is defined as the product $\langle \boldsymbol{E}_\parallel \cdot \boldsymbol{w}_\parallel \rangle$ of the local parallel electric field and the parallel component of particle peculiar velocity ($\boldsymbol{w} \equiv \boldsymbol{v} - \boldsymbol{u}$) averaged over all particles within a given region of the velocity space (Fig. 14 shows only the dependence on $w_\parallel$). The origin of the sign reversal around $w_\parallel \sim \pm v_{\text{th}i0}$ remains uncertain, but could relate to the Landau damping of acoustic fluctuations or could be a signature of the viscous heating (though if so, exactly how this arises remains poorly understood). The Landau-damping signatures at $w_\parallel \sim \pm v_{A0}$ are present at early times, but recede as the simulation progresses. This indicates that Landau damping is suppressed (but still important), and a significant fraction of the heating in the quasisteady state is due to the pressure-anisotropic

viscous stress. We measure large-scale viscous heating to be responsible for approximately one-half of the overall heating rate.

We defer an investigation of how heating and scattering affect the ion distribution function to Appendix C.

IV. DISCUSSION

A. Simulation dynamics and effective viscosity

In this paper, we explore the evolution of turbulent fluctuations in a collisionless, high-β plasma. The initially driven fluctuations become unstable to mirror and, later, to AIC instabilities. These instabilities result in ion-Larmor-scale perturbations of the magnetic field, which cause ions to scatter with a characteristic scattering frequency $\sim S\beta$, where $S \equiv \hat{\boldsymbol{b}}\hat{\boldsymbol{b}} : \boldsymbol{\nabla}\boldsymbol{u}$ is the growth rate of the magnetic-field strength. This scattering limits the (otherwise adiabatically driven) pressure anisotropy. The average value of the pressure anisotropy ultimately becomes negative (i.e., $p_\parallel > p_\perp$), thereby triggering the firehose instability. The pressure anisotropy then fluctuates across the box and has a broadband spectrum that peaks at the viscous scale, which, for the effective collisionality $\nu \sim S\beta$ and Alfvénic Mach number $M_A \sim 1$, is always comparable to the driving scale. The root-mean-square value of pressure anisotropy is consistent with the Braginskii value of $\nu^{-1}\hat{\boldsymbol{b}}\hat{\boldsymbol{b}} : \boldsymbol{\nabla}\boldsymbol{u}$ with ν measured directly from the particles, although there is a phase lag between it and the parallel rate of strain, which makes the dynamical impact of pressure anisotropy somewhat different than found in Braginskii MHD [55]. The parallel viscous stress associated with the instability-regulated pressure anisotropy leads to irreversible dissipation, which peaks at a scale $\ell_{\nu,\mathrm{eff}}$ that is close to the outer scale of the turbulence, and steepens the kinetic-energy spectrum below that scale to a spectral slope close to -2.

B. Ion energization

At high values of β, the viscous heating, to which we attribute the steepening of the kinetic-energy spectrum, dissipates the majority of the cascade energy flux. This heating mechanism should persist, no matter the scale separation in the system, as long as the outer-scale fluctuations are above the Alfvén-wave interruption limit (i.e., as long as their amplitudes are such that the pressure anisotropy that they adiabatically produce ventures beyond the β-dependent kinetic-instability thresholds). In addition to large-scale viscous heating, there is considerable heating at subviscous scales, especially during the early stages of the simulations. We attribute this heating, which peaks at $k_\perp \rho_i \sim \beta^{-1/4}$ [see Eq. (27)], to Landau damping, the dominant mechanism in gyrokinetic simulations [78]. The ion-to-electron heating ratio is ~ 5–10 in all our simulations (electron heating is measured via the hyper-resistive dissipation at $k_\perp \rho_{i0} \gg 1$). There is also considerable nonlocal energy transfer from driving scales to

kinetic scales due to the firehose instability (comparable to overall energy flux; see Fig. 13).

For studies of high-β turbulence in fully collisionless plasmas, there is an important physical ingredient missing from our simulations: realistic electron physics. Imagine a turbulent plasma composed of collisionless ions and electrons. The large-scale fluctuations make the distribution functions of both ions and electrons anisotropic, and at sufficiently large β unstable to pressure-anisotropy-driven instabilities. If the quasisteady-state anisotropy of both species is Braginskii-like, with $\Delta p/p \sim \nu^{-1}\hat{\boldsymbol{b}}\hat{\boldsymbol{b}} : \boldsymbol{\nabla}\boldsymbol{u}$—as it is for ions in our simulations—the ion-to-electron heating ratio should be

$$\frac{Q_i}{Q_e} \sim \frac{p_i/\nu_i}{p_e/\nu_e}. \tag{28}$$

Therefore, the partition of energy is determined by the effective collisionality of the species. If the collisionality of both species is $\nu \sim S\beta$, then $p/\nu \propto \beta/\nu = \mathrm{const}$ is independent of both β and the species. It is therefore possible that ions and electrons receive the same amounts of energy, which contradicts, e.g., the models used in the interpretation of Event Horizon Telescope images of black-hole accretion flows in M87 and around Sgr A* [98,99]. This estimate depends on the exact thresholds of the instabilities that regulate the particle velocity distributions. For example, Sharma *et al.* [100] argue that, for AIC and electron-whistler instabilities, $Q_i/Q_e \sim 10$, consistent with some theories of radiatively inefficient black-hole accretion flows.

Additionally, in the presence of cooling, the electron temperature can decrease due to radiation. This would lead to a decrease in T_e, and thus β_e. If β_e decreases to a point where the plasma is stable to electron microinstabilities, this can lead to a state with $Q_i/Q_e \gg 1$ and, thus, $T_i/T_e \gg 1$. The resulting large temperature ratios may persist, as there are no known collisionless mechanisms for efficient electron-ion thermal coupling [101].

One particularly important application of the results of this section is to the interpretation of Event Horizon Telescope images of black-hole accretion flows. This interpretation involves carrying out general-relativistic magnetohydrodynamic simulations with some prescription for the heating rate of the electrons [98,99], which is typically informed from gyrokinetic calculations [78,102]. In Fig. 15, we display a summary plot of the ion-to-electron heating ratio obtained from our hybrid-kinetic simulations done with PEGASUS++ as a function of plasma β. The low-β values are taken from our earlier work on ion energization in strong Alfvénic turbulence [79,80], while the high-β points represent the results of this paper. Averaged over the final $3.5t_{\mathrm{cross}}$, about 83% of the total cascaded energy is absorbed by ions in the $\beta_{i0} = 16$ simulation, and about 82% at $\beta_{i0} = 4$. The remaining energy flux cascades further
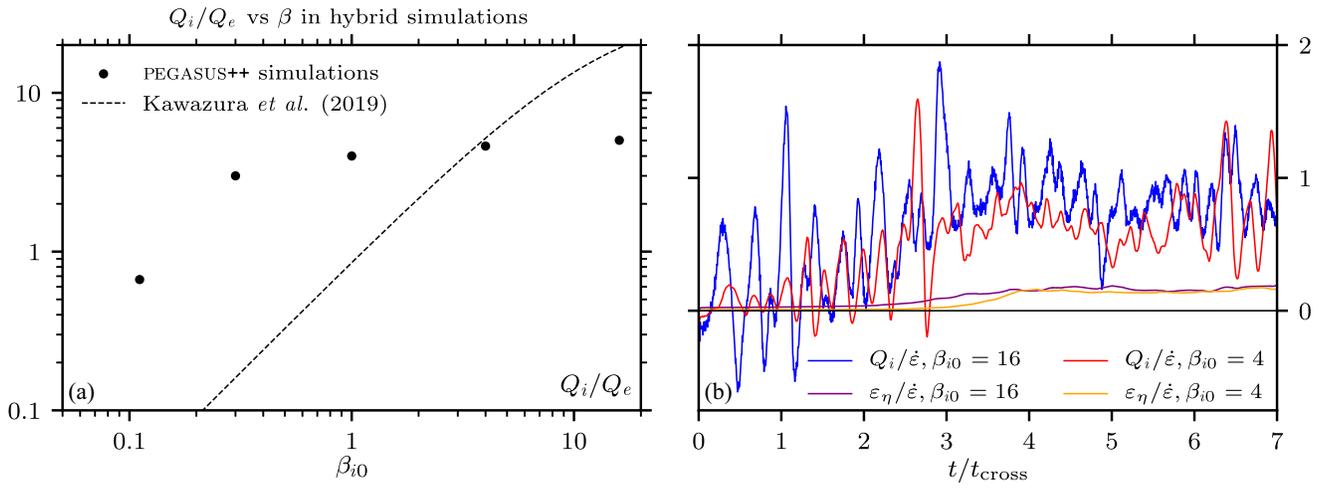
FIG. 15.   (a) The ratio of ion to electron energization Q_i/Q_e as a function of plasma β from several hybrid-kinetic simulations ($\beta_{i0} = 1/9$ simulation from Ref. [80], $\beta_{i0} = 1$ and 0.3 simulations from Ref. [79], and $\beta_{i0} = 16$ and 4 simulations herein). Ion heating is measured directly from the evolution of the thermal energy of the particles. Electron heating is inferred from hyperresistive dissipation near the grid scale. For comparison, the dashed line shows the results from the hybrid-gyrokinetic simulations of Ref. [78]. (b) Time dependence of ion heating (Q_i) and hyperresistive dissipation (ε_η) in the high-β hybrid-kinetic simulations. All lines are normalized to the total energy dissipation $\dot{\varepsilon}$ averaged over the final $3.5t_{\mathrm{cross}}$ of each simulation.

until it is removed by hyperresistivity near the grid scale. We estimate the electron heating in hybrid kinetics as this hyperresistive dissipation ε_η. We also plot (dashed line) the predicted Q_i/Q_e from a series of simulations with gyro-kinetic ions and fluid electrons [78]. Note that gyrokinetics assumes $\delta B/B \ll 1$, while the fluctuations in our simulations have finite amplitudes. Our results differ significantly from these hybrid-gyrokinetic predictions, which indicates the importance of including nonadiabatic processes (such as kinetic microinstabilities and nonadiabatic heating channels) that are ordered out of gyrokinetics (the only available dissipation channels in gyrokinetics are parallel Landau damping and nonlinear perpendicular phase mixing).

Finally, it is important to understand the caveats related to using Fig. 15(a) for black-hole accretion models. Other than missing electron physics, an important limitation of our work is limited scale separation between the energy-injection scale and the dissipation scale of the cascade. For the low-β runs [79,80], the effective scale separation is $\sim10^4$ (the separation between ρ_i and the scale at which $\delta u/v_A \sim 1$). Such a scale separation is realistic for the solar wind, but not for accretion flows, where it is expected to be $\sim10^{10}$. Dissipation mechanisms used to explain the low-β results (stochastic and cyclotron heating) are expected to diminish with scale separation, so it is unclear whether the conclusions from Refs. [79,80] will hold at scale separations relevant to black-hole accretion. That being said, astrophysical turbulence can be imbalanced (e.g., the solar-wind turbulence is measured to be imbalanced [103]). Recent work on imbalanced cascades [94,104] concluded that the imbalanced portion of the energy flux could not cascade beyond the ion-Larmor scale and was eventually

dissipated through AIC heating. Such dissipation is expected to be controlled solely by the degree of imbalance and not by the scale separation in the cascade.

For high-β turbulence, the results of this paper (Sec. III F) indicate that the majority of dissipation happens at the outer scale of the cascade. Therefore, ion heating may depend on the properties of the forcing, and may require a better understanding of realistic turbulence injection (e.g., through kinetic magnetorotational instability [5,72,73]). The results from high-β hybrid-kinetic simulations are likely to depend upon the amplitude of the forcing and on the scale separation (e.g., through their impact on spectral anisotropy at ion-Larmor scale). To test the latter, we conduct a test for the amplitude dependence by running a $\beta_{i0} = 16$ simulation with $\delta u_L/v_A \sim 1$, having a lower ion-scale spectral anisotropy than other runs used in this work. In this simulation, a slightly larger fraction of the cascade rate, $\sim90\%$, is dissipated on ions.

C. Dependence on scale separation

Given the limited size of our simulations, it is important to understand whether our results are expected to hold at scale separations relevant to astrophysical systems. One important (although transient) feature of our runs is Landau damping, which eventually pushes the pressure anisotropy over the firehose-instability threshold by raising the parallel temperature. If the effective collisionality from the instabilities is strong enough to interfere with the maintenance of the Landau resonance (namely, $\nu_{\mathrm{eff}} \gg k_\parallel v_{\mathrm{th}i}$), then the Landau damping can be shut off. From our estimates in Sec. II, $\nu_{\mathrm{eff}} \sim \beta M_A^3 v_A/L$, and thus at $k_\parallel\rho_\star \sim 1$, where Landau damping is expected to become important, $k_\parallel v_{\mathrm{th}i}/\nu_{\mathrm{eff}} \sim (L/\rho_i)/(\beta_i^{3/4}M_A^3) \gg 1$, the inequality following from the

typically enormous astrophysical scale separation between L and ρ_i. Therefore, Landau damping is expected to be important (arguably more important than in our simulations) and the plasma will approach the firehose-instability threshold in approximately one large-scale dynamical time (assuming that the entire cascade with $M_A \sim 1$ is dissipated as parallel heating; our simulations approach it in $\sim 4t_{\mathrm{cross}}$ given the smaller fluctuation amplitude of $M_A \sim 0.5$).

In order to estimate the amplitude of firehose fluctuations at the Larmor scale, we can leverage some results from recent PEGASUS++ expanding-box simulations [45,84], which have shown for $\Omega_i/S \gtrsim 30\beta_i^{3/2}$ that the kinetic firehose threshold is $\approx -1.4/\beta_i$ and that the instability saturates at an amplitude $(\delta B_\perp/B)_{\mathrm{FH}}^2 \sim (S/\Omega_i)^{1/2} \sim M_A^{3/2}(\rho_i/L)^{1/2}\beta_i^{-1/4}$ for $S \sim M_A^3 v_A/L$. For comparison, the amplitude of fluctuations in an Alfvénic cascade with the Goldreich-Sridhar spectrum evaluated at $k_\perp \rho_i \sim 1$ is $(\delta B_\perp/B)_{\mathrm{AW}}^2 \sim M_A^2(\rho_i/L)^{2/3} \ll (\delta B_\perp/B)_{\mathrm{FH}}^2$ for $M_A \sim 1$ and $\rho_i/L \ll \beta_i^{-3/2}$. For a $k_\perp^{-2}$ spectrum, $(\delta B_\perp/B)_{\mathrm{AW}}^2$ is even smaller at the ion-Larmor scale. We therefore conclude that in astrophysical systems, as found in our simulations, ion-Larmor-scale magnetic-field fluctuations are expected to be composed mostly of firehose modes rather than of Alfvénic fluctuations. Therefore, ion-Larmor-scale fluctuations in our simulations are similar to those expected in astrophysical systems.

D. Observational implications

Unfortunately, outside of the solar wind, observations of turbulence in high-β systems are limited. And the solar-wind observations are in a slightly different regime than our simulations: the solar wind starts as a low-β plasma, which expands and reaches the high-β regime. In this situation, which we studied in Ref. [45], the expansion is also an important source of pressure anisotropy. Nevertheless, the solar wind shows a pressure anisotropy with an average value close to zero, and with a spread consistent with the $1/\beta$ instability thresholds (although the collisional age at ~ 1 au, being comparable to outer-scale dynamical time-scales, is short enough to matter [83]). Our simulations show very similar behavior (see Fig. 5), with a spread in the pressure anisotropy comparable to $1/\beta$ and an average value that is negative but smaller than the firehose threshold.

Outside the solar wind, the most promising system in which high-β turbulence can be studied is the ICM, which has $\beta \sim 100$. There have been several attempts to measure plasma-velocity fluctuations in the ICM. The x-ray observations presented in Ref. [58] use bremsstrahlung emission from the hot intracluster plasma to determine the density fluctuations, from which the velocity fluctuations are then inferred. Their energy spectrum is consistent with the Kolmogorov prediction and extends to scales considerably smaller than the viscous scale expected from Coulomb collisions alone. This implies that the effective collisionality of the ICM is appreciably enhanced. One

explanation for this enhancement is scattering from kinetic microinstabilities, which can be triggered for turbulence with Alfvénic Mach numbers $M_A \gtrsim 1/\beta \ll 1$. The value of collisionality required to explain the spectra in Ref. [58] is consistent with our analytical estimate Eq. (13).

Our simulations show that, although the effective viscous scale is large, the spectrum in this case is closer to Kolmogorov than $\nabla^2 \boldsymbol{u}$ dissipation would imply (it steepens to approximately $k_\perp^{-2}$ instead of exhibiting an exponential decrease; current observations [58] cannot distinguish between $-5/3$ and -2 spectral slopes). Reference [59] used optical emission from cold gas in the ICM to measure the spectrum of plasma velocity. Their observations show a slightly steeper spectrum than $-5/3$; for some clusters, it is close to -2. Our simulations predict similar spectra: the effective viscosity does not produce an exponential cutoff in the spectrum, but rather steepens it slightly. Optical measurements are much more precise than those taken in the x ray, but their connection to turbulence in the bulk ICM is unclear (optical measurements are dominated by the interiors of cluster cores, which are expected to be much more collisional than ICM outskirts). Future observations are required to determine better the relationship between our simulations and the ICM turbulence.

Of course, even though we have a testable prediction for the slope of the subviscous spectra, the scale separation we use in our simulations is much smaller than in actual astrophysical systems; our simulations have only ~ 1 decade in scale between $\ell_{\nu,\mathrm{eff}}$ and ρ_i, which is much smaller than the ~ 12 decades in the ICM. Relatively small-scale separation leads to firehose fluctuations being produced relatively close to $\ell_{\nu,\mathrm{eff}}$, which may impact the spectral slopes and the comparison between the rate of strain and the pressure anisotropy. However, we are encouraged that our numerical results agree well with the analytical estimates presented in Sec. II, which we expect to hold for any scale separation. Given the steep scaling of the computational cost of kinetic simulations with scale separation (as the fourth power), future efforts should concentrate on the development of realistic subgrid models for kinetic physics in high-β plasmas.

V. SUMMARY

We present analytical estimates of effective collisionality and viscosity in collisionless high-β turbulence and test those estimates by performing first-principles hybrid-kinetic simulations. We explore the interplay between local nonlinear turbulent cascades and kinetic instabilities, which tap the free energy of large-scale deviations from local thermodynamic equilibrium (e.g., pressure anisotropies) to produce small-scale magnetic-field fluctuations. Our results are summarized as follows.

(i) Large-scale fluctuations (continuously driven by a random, incompressible force in our simulations) generate pressure anisotropy through approximate

adiabatic invariance and ultimately excite rapidly growing kinetic instabilities, thereby transferring energy nonlocally to small (ion-Larmor) scales.

(ii) At the beginning of the simulations, the main kinetic instabilities are mirror and AIC, because the magnetic-field strength in our box is mostly increasing, which drives positive-pressure anisotropy.

(iii) Turbulence reaches an intermediate steady state, in which the cascade energy is dissipated primarily by Landau damping, causing parallel heating.

(iv) The parallel heating pushes the system toward the firehose-instability threshold.

(v) In the quasisteady state, the turbulence is primarily mediated by the firehose instability with nonlocal energy transfer due to the growth of small-scale firehose fluctuations that is comparable to the overall energy flux. The mean pressure anisotropy is slightly negative, with some parts of the box below the kinetic-firehose threshold.

(vi) Firehose instability creates small-scale magnetic fluctuations, which scatter particles. The effective collisionality in the quasisteady state is consistent with an estimate based on incompressible Braginskii MHD with the pressure anisotropy regulated by firehose instability, viz., $\nu_{\mathrm{eff}} \sim \beta \hat{\boldsymbol{b}}\hat{\boldsymbol{b}} : \boldsymbol{\nabla u}$.

(vii) The effective viscous scale due to the firehose-induced collisionality is close to the driving scale of the turbulence. For a cascade with Alfvénic Mach number M_A, our analytical estimates suggest that the ratio of effective viscous scale and the outer scale is $\ell_\nu/L \sim M_A^{-3}$. In our simulations, $M_A \sim 1$ at the outer scale.

(viii) In addition to small-scale dissipation due to Landau damping, there is a considerable amount of viscous heating at the effective viscous scale.

(ix) Ion heating removes the majority of the cascading energy, $\sim 80\%$–90% for $\beta = 4$ and 16.

(x) Viscous heating steepens the kinetic-energy spectrum of the turbulence. The spectrum is approximately $k_\perp^{-2}$. Large-scale viscous heating dissipates $\approx 40\%$–45% of the cascade as ion heating.

(xi) The magnetic-energy spectrum is shallower than $k_\perp^{-5/3}$ near the ion-Larmor scale due to the presence of firehose fluctuations.

This work provides the first self-consistent estimate of the effective viscosity in a turbulent collisionless high-β plasma. It makes observational predictions, which can be tested in the solar wind [105] and in the intracluster medium, and raises important complications for models of radiatively inefficient black-hole accretion flows.

APPENDIX A: MIRROR AND AIC INSTABILITIES IN $\beta_{i0} = 16$ SIMULATION

In the early stages of our simulations, the external driving excites large-scale modes, which produce large coherent patches of positive-pressure anisotropy, owing to the conservation of the particles' magnetic moments. Once this pressure anisotropy grows above the $\sim 1/\beta$ threshold, the mirror instability is triggered. This instability produces "cross-patterned" oblique structures in $\delta B_\parallel$, which act to reduce the magnetic-field strength locally. Particles trapped in these structures "see" an almost constant-in-time magnetic field, which prevents the pressure anisotropy of the trapped-particle population to grow beyond the mirror-instability threshold. Eventually the mirrors become large enough and their edges sharp enough to scatter particles [24,48].

We illustrate this process in Fig. 16, which shows snapshots of $\delta B_\parallel$ in the planes perpendicular [Fig. 16(a)] and parallel [Fig. 16(b)] to the background magnetic field, two-dimensional histograms [Fig. 16(c)] of pressure anisotropy and plasma β, and structure functions of the magnetic-field fluctuations [Fig. 16(d)], defined as

$$\mathcal{S}^n(\boldsymbol{\ell}) \equiv \langle |\boldsymbol{B}(\boldsymbol{x} + \boldsymbol{\ell}) - \boldsymbol{B}(\boldsymbol{x})|^n \rangle_{\boldsymbol{x}}, \qquad \text{(A1)}$$
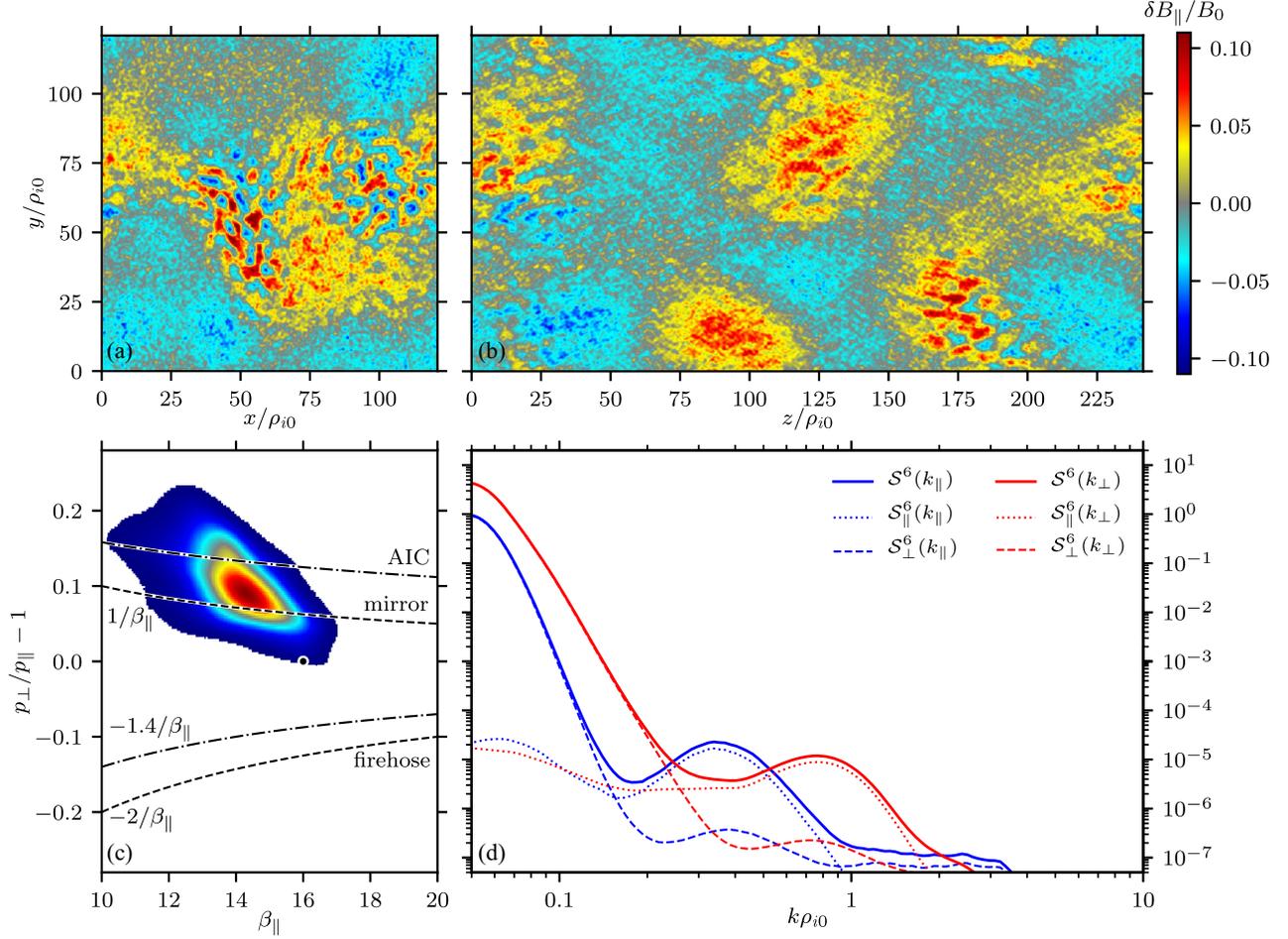
FIG. 16.   (a),(b) Snapshots of parallel magnetic-field fluctuations $\delta B_\parallel$ (relative to $\boldsymbol{B}_0$) during the early stage of the $\beta_{i0} = 16$ simulation ($t \approx 0.4 t_{\text{cross}}$). Panel (a) shows a slice perpendicular to the guide field; panel (b) shows a slice along the guide field. There is a clear "cross" pattern in both slices, indicating oblique mirror fluctuations. (c) The distribution function of points in the box as a function of their β and pressure anisotropy. Dashed lines show the thresholds for mirror [18–20] and fluid-firehose [14–17] instabilities; dot-dashed line represents a threshold for the AIC instability [21,74] and kinetic firehose instabilities [45,84]. In this snapshot, the majority of the box is above the mirror threshold. The black dot indicates the initial position of the simulation box. (d) Sixth-order structure function of the fluid velocity- and magnetic-field fluctuations. High-order structure functions are chosen to highlight intense small-scale fluctuations, which for this snapshot are mirror modes: oblique modes producing kinetic-range peaks in both parallel and perpendicular structure functions of parallel magnetic-field fluctuations of parallel magnetic field.

where n is the order of the structure function and $\langle \cdot \rangle_x$ represents the spatial average over the simulation domain. In addition to the full structure function Eq. (A1), we also compute the structure functions of magnetic-field fluctuations oriented parallel and perpendicular to the local, scale-dependent magnetic-field direction. To determine the latter, we define

$$\boldsymbol{B}_{\text{loc}}(\boldsymbol{\ell}, \boldsymbol{x}) \equiv [\boldsymbol{B}(\boldsymbol{x} + \boldsymbol{\ell}) + \boldsymbol{B}(\boldsymbol{x})]/2, \qquad (A2)$$

and then compute the structure functions of those fluctuating magnetic-field components parallel and perpendicular to $\hat{\boldsymbol{b}}_{\text{loc}} \equiv \boldsymbol{B}_{\text{loc}}/B_{\text{loc}}$ [107], e.g., $\mathcal{S}_\parallel$ represents the structure function computed using $\boldsymbol{B}_\parallel(\boldsymbol{\ell}, \boldsymbol{x}) \equiv [\boldsymbol{B}(\boldsymbol{x}) \cdot \hat{\boldsymbol{b}}_{\text{loc}}(\boldsymbol{\ell}, \boldsymbol{x})] \times \hat{\boldsymbol{b}}_{\text{loc}}(\boldsymbol{\ell}, \boldsymbol{x})$, and $\mathcal{S}_\perp$ represents a structure function

computed using $\boldsymbol{B}_\perp(\boldsymbol{\ell}, \boldsymbol{x}) \equiv \boldsymbol{B}(\boldsymbol{x}) - \boldsymbol{B}_\parallel(\boldsymbol{\ell}, \boldsymbol{x})$. For additional details concerning structure-function analyses of turbulence simulations, see Ref. [108].

Figure 16 shows a snapshot from the $\beta_{i0} = 16$ simulation at a relatively early time. One can see several large-scale modes, which have not yet had time to shear one another. These large-scale fluctuations produce appreciable positive pressure anisotropy ($\Delta p > 0$), with a considerable fraction of the box being above both the mirror and AIC instability thresholds. We choose this particular snapshot because it highlights the mirror instability being triggered by pressure anisotropy—throughout the box, one can see oblique fluctuations predominantly of $\delta B \approx \delta B_\parallel$. To examine these fluctuations further, we plot the sixth-order structure functions of $\delta B_\perp$ (blue) and $\delta B_\parallel$ (red). The high order
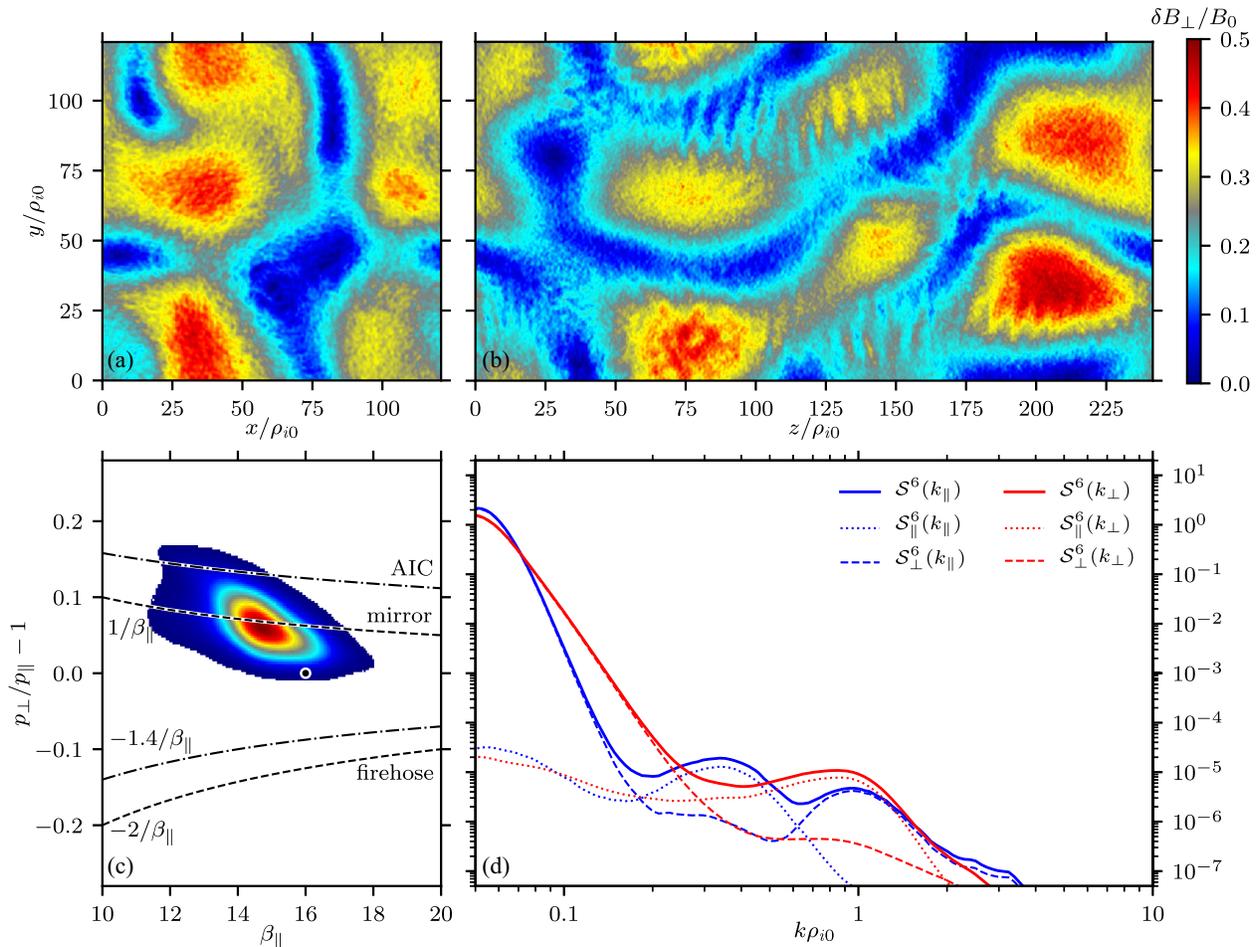
FIG. 17. The same as Fig. 16, but for a slightly later time $t \approx 0.6 t_{\mathrm{cross}}$, at which quasiparallel fluctuations are manifest. The perpendicular component of magnetic field is shown instead of the parallel one. Those fluctuations are produced by the AIC instability. The structure functions show two predominant modes of fluctuations: oblique fluctuations in $\delta B_{\parallel}$ caused by mirror instability and quasiparallel fluctuations in $\delta B_{\perp}$, which are AIC waves.

of these structure functions is chosen to highlight localized, high-amplitude structures, such as those expected to be produced by kinetic microinstabilities [24]. This analysis clearly shows that there is considerable magnetic energy at the driving scales of the simulation and some energy at the kinetic scales (due to instabilities), with very little energy in between. This is an indication that the energy stored in the anisotropic distribution function has been transferred non-locally from the driving scales (which have the largest pressure anisotropy) to the kinetic scales.

At the scale separations achieved in our simulations, trapping of particles by mirror fluctuations and the consequent regulation of the pressure anisotropy toward the mirror thresholds occur relatively slowly. Because of this, the unstable pressure anisotropy [24,48,77] overshoots the mirror threshold enough to reach the AIC instability threshold (this is unlikely to occur in real astrophysical systems, which have significantly larger scale separations). Figure 17 shows a simulation snapshot at $t \approx 0.6 t_{\mathrm{cross}}$, by which time the AIC instability has had enough time to

grow, as indicated by the strong quasiparallel fluctuations in $\delta B_{\perp}$ (cf. Fig. 16). Examination of the structure functions indicates that this instability is cleanly separated from the previously triggered mirrors: in addition to "bumps" in the structure functions due to the mirror instability, an extra bump in $\delta B_{\perp}$ appears, with no obvious indication of interactions between the two instabilities. Finally, the histogram of pressure anisotropy and $\beta_{\parallel}$ shows that the pressure anisotropy has decreased from the previous snapshot even though the fluctuation amplitude at the driving scale has increased, suggesting that the instabilities have already backreacted on the plasma and reduced its departures from isotropy.

APPENDIX B: ENERGY TRANSFER IN KINETIC HIGH-β TURBULENCE

In this appendix, we summarize the energy-transfer analysis that we use to study nonlocal interaction in high-β kinetic turbulence. Energy is injected by the external

forcing in the form of bulk kinetic energy $\mathcal{E}_{\text{bulk}} \equiv \varrho u^2 / 2$. Part of this energy is then converted into magnetic energy $\mathcal{E}_{\text{mag}} \equiv B^2 / 8\pi$ through electromagnetic induction. This energy is ultimately dissipated by increasing the thermal energy of ions ($\mathcal{E}_{\text{th}} \equiv p_\perp + p_\parallel / 2$) or by hyperresistivity at small scales.

The evolution of bulk kinetic energy follows from the momentum equation for ions (assuming gyrotropy of the ion distribution function):

$$\frac{\partial \varrho \boldsymbol{u}}{\partial t} = -\boldsymbol{\nabla} \cdot \left[\varrho \boldsymbol{u} \boldsymbol{u} + \left(p_\perp + nT_e + \frac{B^2}{8\pi} \right) \mathsf{I} \right.$$
$$\left. - \left(\frac{B^2}{4\pi} + \Delta p \right) \hat{\boldsymbol{b}} \hat{\boldsymbol{b}} \right] + \boldsymbol{F}. \tag{B1}$$

Similarly, the evolution of magnetic energy follows from Faraday's and Ohm's laws:

$$\frac{\partial \boldsymbol{B}}{\partial t} = -c \boldsymbol{\nabla} \times \boldsymbol{E}$$
$$= \boldsymbol{\nabla} \times \left[\boldsymbol{u} \times \boldsymbol{B} - \frac{(\boldsymbol{\nabla} \times \boldsymbol{B}) \times \boldsymbol{B}}{4\pi n e / c} + \eta_{\text{hyper}} \boldsymbol{\nabla}^2 \left(\frac{\boldsymbol{\nabla} \times \boldsymbol{B}}{4\pi / c} \right) \right], \tag{B2}$$

where the last term represents dissipation due to hyperresistivity. Equations for the evolution of kinetic and magnetic energies can be obtain by multiplying Eqs. (B1) and (B2) by $\boldsymbol{u}$ and $\boldsymbol{B}$ correspondingly. Thermal energy $\mathcal{E}_{\text{th}}$ in the system increases due to viscous dissipation and compressive heating:

$$\frac{d\mathcal{E}_{\text{th}}}{dt} = -\int \mathsf{P} : \boldsymbol{\nabla} \boldsymbol{u} \, d^3 \boldsymbol{x}$$
$$= -\int [p_\perp \boldsymbol{\nabla} \cdot \boldsymbol{u} - (\Delta p \hat{\boldsymbol{b}} \hat{\boldsymbol{b}}) : \boldsymbol{\nabla} \boldsymbol{u}] d^3 \boldsymbol{x}. \tag{B3}$$

In what follows, it is useful to define the energy "reservoirs" corresponding to kinetic, magnetic, and thermal energies, with each reservoir associated with a certain vector field $\boldsymbol{a}$, so that $\mathcal{E}_{\boldsymbol{a}} \equiv a^2 / 2$. For the bulk kinetic energy, $\boldsymbol{a}^u = \sqrt{\varrho} \boldsymbol{u}$, so

$$\mathcal{E}_{\text{bulk}} = \int \frac{(\sqrt{\varrho} \boldsymbol{u})^2}{2} d^3 \boldsymbol{x}$$
$$= \frac{1}{(2\pi)^3} \int \frac{1}{2} (\sqrt{\varrho} \boldsymbol{u})_{\boldsymbol{k}} \cdot (\sqrt{\varrho} \boldsymbol{u})_{\boldsymbol{k}}^* d^3 \boldsymbol{k}. \tag{B4}$$

The definition for magnetic energy is also straightforward, $\boldsymbol{a}^B \equiv \boldsymbol{B} / \sqrt{4\pi}$, so

$$\mathcal{E}_{\text{mag}} = \int \frac{(\boldsymbol{B} / \sqrt{4\pi})^2}{2} d^3 \boldsymbol{x}$$
$$= \frac{1}{(2\pi)^3} \int \frac{1}{8\pi} (\boldsymbol{B})_{\boldsymbol{k}} \cdot (\boldsymbol{B})_{\boldsymbol{k}}^* d^3 \boldsymbol{k}. \tag{B5}$$

The definition of the energy reservoir associated with anisotropic thermal energy is less straightforward. In this article, we use $\boldsymbol{a}^{\Delta p} \equiv \sqrt{|\Delta p|} \hat{\boldsymbol{b}}$. This definition is motivated by two facts. First, in the KRMHD limit, $(\delta \boldsymbol{a}^{\Delta p})^2 / 2$ matches up to a sign with the corresponding term in the plasma free energy [46]:

$$W_{\text{KRMHD}}^\Delta = \int \beta_{\parallel i} \frac{\Delta_i}{2} \frac{\delta B_\perp^2}{B_0^2} d^3 \boldsymbol{x}. \tag{B6}$$

Second, the thermal energy of the plasma can be written as

$$\mathcal{E}_{\text{th}} = \int \frac{n(2T_\perp + T_\parallel)}{2} d^3 \boldsymbol{x} = \int \left(\frac{3}{2} p_\perp - \frac{1}{2} \Delta p \right) d^3 \boldsymbol{x}$$
$$= \mathcal{E}_{\text{th}}^{\text{iso}} - \int \frac{\vartheta_{\Delta p}}{2} (\sqrt{|\Delta p|} \hat{\boldsymbol{b}})^2 d^3 \boldsymbol{x}$$
$$= \mathcal{E}_{\text{th}}^{\text{iso}} - \frac{1}{(2\pi)^3} \int \frac{\vartheta_{\Delta p}}{2} (\sqrt{|\Delta p|} \hat{\boldsymbol{b}})_{\boldsymbol{k}} \cdot (\sqrt{|\Delta p|} \hat{\boldsymbol{b}})_{\boldsymbol{k}}^* d^3 \boldsymbol{k}, \tag{B7}$$

where $\vartheta_{\Delta p} \equiv \text{sgn}(\Delta p)$ and $\mathcal{E}_{\text{th}}^{\text{iso}}$ is the "isotropic thermal energy" associated with $p_\perp$. The proposed definition of the anisotropic thermal energy allows us to consider the "advectionlike" terms in Eqs. (B3) and (B4) associated with Δp separately from the "compressionlike" terms proportional to divergences of various vector fields in the system and terms proportional to gradients of $p_\perp$ and $B^2 / 2$.

The rates of exchange of energy between different reservoirs follow from Eqs. (B1)–(B3). Let us consider the individual terms in Eq. (B1) separately. As we show later (Fig. 18), the most dominant terms are related to the Reynolds, Maxwell, and anisotropic viscous stresses. The rate of change of kinetic energy due to the Reynolds stress is

$$\frac{d\mathcal{E}_{\text{bulk}}^{\text{Re}}}{dt} = -\int \frac{(\sqrt{\varrho} \boldsymbol{u})}{\sqrt{\varrho}} \cdot \{ \boldsymbol{\nabla} \cdot [(\sqrt{\varrho} \boldsymbol{u})(\sqrt{\varrho} \boldsymbol{u})] \} d^3 \boldsymbol{x}$$
$$= -\int \frac{\boldsymbol{a}^u}{\sqrt{\varrho}} \cdot [\boldsymbol{\nabla} \cdot (\boldsymbol{a}^u \boldsymbol{a}^u)] d^3 \boldsymbol{x}$$
$$= -\int \left\{ \boldsymbol{a}^u \cdot \left[\frac{\boldsymbol{a}^u}{\sqrt{\varrho}} \cdot \boldsymbol{\nabla} \boldsymbol{a}^u \right] + \frac{(\boldsymbol{a}^u)^2}{\sqrt{\varrho}} \boldsymbol{\nabla} \cdot \boldsymbol{a}^u \right\} d^3 \boldsymbol{x}. \tag{B8}$$

The second term in the integrand of the final expression is related to compressive motions ($\propto \boldsymbol{\nabla} \cdot \boldsymbol{a}^u$). As we show later (Fig. 18), in high-β turbulence, this term is smaller than the first, advectionlike term. To explore the locality of this cascade, we define k-shell averaged fields:

$$\langle \boldsymbol{a} \rangle_K \equiv \frac{1}{(2\pi)^3} \int_{\boldsymbol{k} \in K} \boldsymbol{a}_{\boldsymbol{k}} e^{-i\boldsymbol{k} \cdot \boldsymbol{x}} d^3 \boldsymbol{k}. \tag{B9}$$

We choose cylindrical $k_\perp$ shells with width $dk_\perp \propto k_\perp$, so that the shells have equal width in $\log k_\perp$. With such a choice
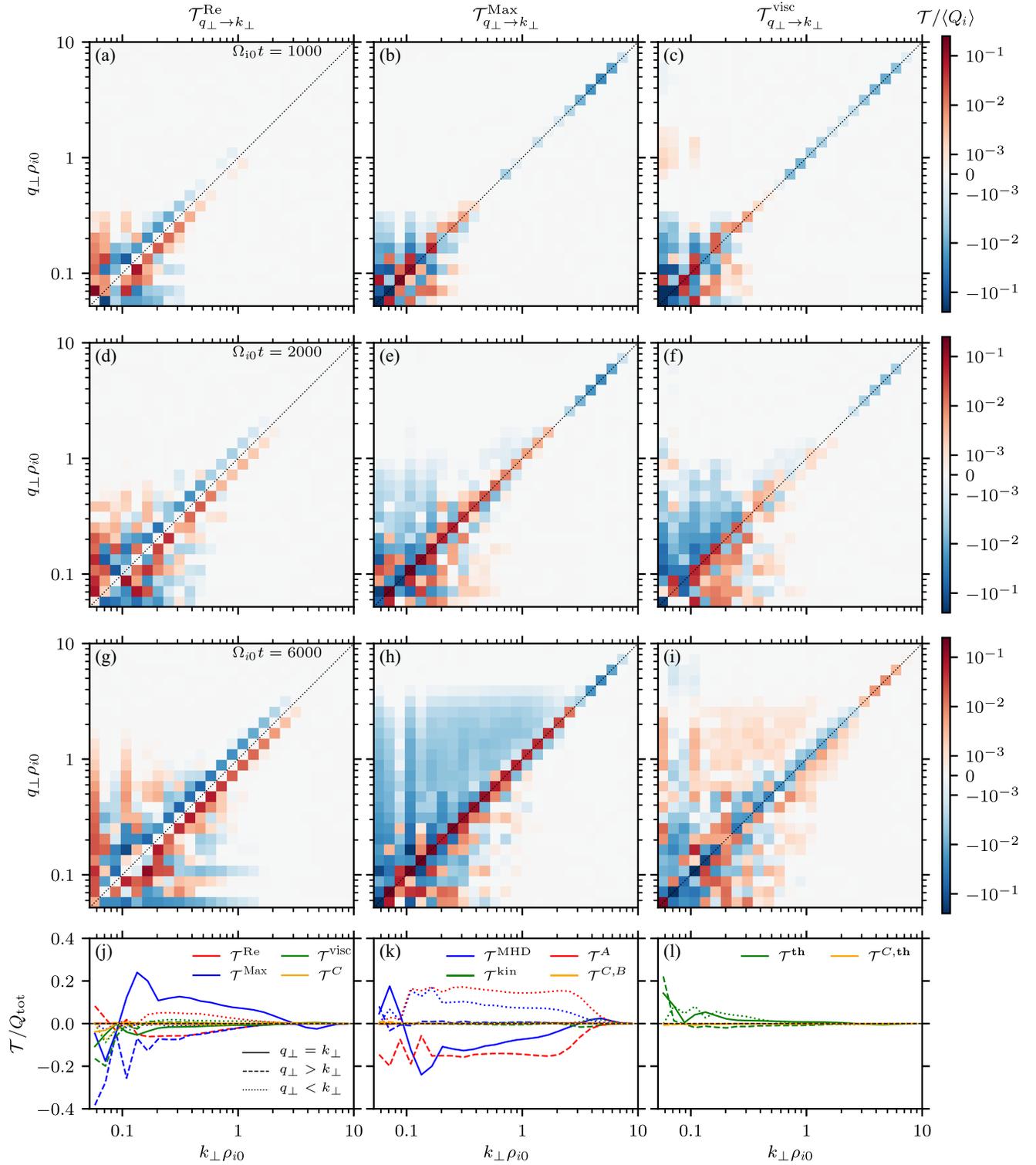
FIG. 18. Nonlocal energy transfer functions averaged over the quasisteady state due to the Reynolds stress (left), Maxwell stress (center), and anisotropic viscous stress (right) in $\beta_{i0} = 16$ simulation. Most of the transfer in the early stages of the simulation is local, but there is considerable nonlocal transfer mediated by the Maxwell stress in the quasisteady state. Panels (j)–(l) show the remaining transfer terms in the momentum equation as well as terms in the induction equation and the equation for thermal energy. Note that terms associated with compressions and gradients of isotropic pressures are smaller than "advectionlike" terms.

of shells, $\langle a \rangle_K$ is proportional to the fluctuation amplitude $\delta a_{k_\perp}$ (i.e., $\delta a_{k_\perp}^2 = \int_{k_\perp} |a_k|^2 d^3 k$). As a result, an energy transfer rate of the form $\langle u \rangle_K \cdot [\langle u \rangle_K \cdot \boldsymbol{\nabla}]\langle u \rangle_K \sim k_\perp \delta u_{k_\perp}^3 \sim \varepsilon$ approximates the cascade rate. For a conservative cascade, this energy transfer rate is the same for each $k_\perp$ shell.

For nonoverlapping shells, the shell-averaged vectors a_K satisfy by construction

$$a = \sum_K \langle a \rangle_K, \quad (B10)$$

and, therefore,

$$\frac{d\mathcal{E}_{\text{bulk}}^{\text{Re}}}{dt} = \sum_K \int \frac{d\langle a^u \rangle_K^2}{dt} d^3 x$$

$$\approx -\sum_K \int \langle a^u \rangle_K \cdot (u \cdot \boldsymbol{\nabla} a^u) d^3 x \equiv \sum_{KPQ} \int T_{KPQ}^{\text{Re}} d^3 x, \quad (B11)$$

where in the last step we define three-shell correlators (see, e.g., Ref. [87] for details):

$$T_{KPQ}^{\text{Re}} \equiv -\langle a^u \rangle_K \cdot (\langle u \rangle_P \cdot \boldsymbol{\nabla}) \langle a^u \rangle_Q. \quad (B12)$$

These correlators describe the transfer of energy associated with field a^u from shell Q to shell K, mediated by field $\langle u \rangle_P$, i.e.,

$$\int \frac{d\langle a^u \rangle_K^2}{dt}\bigg|_{PQ} d^3 x = \int T_{KPQ}^{\text{Re}} d^3 x. \quad (B13)$$

The energy cannot go from shell P to shells K and Q or vice versa. This can be easily seen from the sum of the energies in the shells K and Q during their mutual interaction mediated by the shell P:

$$\int \frac{d\langle a^u \rangle_K^2}{dt}\bigg|_{PQ} + \frac{d\langle a^u \rangle_Q^2}{dt}\bigg|_{PK} d^3 x$$

$$= -\int [\langle a^u \rangle_K \cdot (\langle u \rangle_P \cdot \boldsymbol{\nabla}\langle a^u \rangle_Q) + \langle a^u \rangle_Q \cdot (\langle u \rangle_P \cdot \boldsymbol{\nabla}\langle a^u \rangle_K)] d^3 x$$

$$= -\int \langle u \rangle_P \cdot \boldsymbol{\nabla}\langle a^u \rangle_K \cdot \langle a^u \rangle_Q d^3 x$$

$$= \int \langle a^u \rangle_K \cdot \langle a^u \rangle_Q \boldsymbol{\nabla} \cdot \langle u \rangle_P d^3 x, \quad (B14)$$

so that the total energy during the interaction can only come from the compressive motions of the mediator shell, which are small in high-β turbulence. As we are not interested in specific mediator shells, we can sum over P and introduce a *shell-to-shell* energy transfer function, i.e., the energy-transfer function due to the Reynolds stress [88]:

$$\mathcal{T}_{q_\perp \to k_\perp}^{\text{Re}} \equiv -\int \langle a^u \rangle_{k_\perp} \cdot (u \cdot \boldsymbol{\nabla}\langle a^u \rangle_{q_\perp}) d^3 x. \quad (B15)$$

Similar transfer functions could be defined for any field a and any mediator function f:

$$\mathcal{T}_{q_\perp \to k_\perp}^{a_1 f a_2} \equiv \int \langle a_1 \rangle_{k_\perp} \cdot (f \cdot \boldsymbol{\nabla}\langle a_2 \rangle_{q_\perp}) d^3 x. \quad (B16)$$

Of particular importance to us are the transfer-function rates due to the Reynolds stress Eq. (B15), the Maxwell stress,

$$\mathcal{T}_{q_\perp \to k_\perp}^{\text{Max}} \equiv \int \langle a^u \rangle_{k_\perp} \cdot \left(\frac{B}{\sqrt{4\pi\varrho}} \cdot \boldsymbol{\nabla}\langle a^B \rangle_{q_\perp}\right) d^3 x, \quad (B17)$$

and the anisotropic viscous stress,

$$\mathcal{T}_{q_\perp \to k_\perp}^{\text{visc}} \equiv \int \langle a^u \rangle_{k_\perp} \cdot \left(\vartheta_{\Delta p}\sqrt{\frac{|\Delta p|}{\varrho}}\hat{b} \cdot \boldsymbol{\nabla}\langle a^{\Delta p} \rangle_{q_\perp}\right) d^3 x. \quad (B18)$$

The mediator field for the Maxwell stress has a form of local Alfvén speed, and the mediator for the viscous stress has the form of the sound speed directed along the local magnetic field, but computed using the pressure anisotropy Δp. Both transfer functions have corresponding terms (of opposite signs) in the equations for magnetic energy and the anisotropic thermal energy. Namely,

$$\frac{d\mathcal{E}_{\text{mag}}}{dt}\bigg|_{\text{MHD}} = \int \frac{1}{4\pi} B \cdot [\boldsymbol{\nabla} \times (u \times B)] d^3 x$$

$$= \int [a^B \cdot (a^B \cdot \boldsymbol{\nabla} u) - u \cdot \boldsymbol{\nabla}(a^B)^2 / 2 - (a^B)^2 \boldsymbol{\nabla} \cdot u] d^3 x$$

$$= \sum_{q_\perp k_\perp} \mathcal{T}_{q_\perp \to k_\perp}^{\text{MHD}} + (\text{compressive terms}), \quad (B19)$$

where we only used the "MHD" electric field $u \times B/c$ and

$$\mathcal{T}_{q_\perp \to k_\perp}^{\text{MHD}} \equiv \int \langle a^B \rangle_{k_\perp} \cdot \left(\frac{B}{\sqrt{4\pi\varrho}} \cdot \boldsymbol{\nabla}\langle a^u \rangle_{q_\perp}\right) d^3 x, \quad (B20)$$

and

$$\frac{d\mathcal{E}_{\text{th}}^{\text{visc}}}{dt} = \int \Delta p \hat{b}\hat{b} : \boldsymbol{\nabla} u d^3 x$$

$$= \int \sqrt{\varrho} a^{\Delta p} \cdot (a^{\Delta p} \cdot \boldsymbol{\nabla} u)$$

$$= \sum_{q_\perp k_\perp} \mathcal{T}_{q_\perp \to k_\perp}^{\text{th}} + (\text{compressive terms}), \quad (B21)$$

where

$$\mathcal{T}^{\text{th}}_{q_\perp \to k_\perp} \equiv \int \langle \boldsymbol{a}^{\Delta p} \rangle_{k_\perp} \cdot \left(\vartheta_{\Delta p} \sqrt{\frac{|\Delta p|}{\varrho}} \hat{\boldsymbol{b}} \cdot \boldsymbol{\nabla} \langle \boldsymbol{a}^u \rangle_{q_\perp} \right) d^3\boldsymbol{x}.$$

(B22)

To summarize, we write the time derivative of the bulk kinetic energy as a sum of five terms:

$$\frac{d\mathcal{E}_{\text{bulk}}}{dt} = \sum_{q_\perp k_\perp} [\mathcal{T}^{\text{Re}}_{q_\perp \to k_\perp} + \mathcal{T}^{\text{Max}}_{q_\perp \to k_\perp} + \mathcal{T}^{\text{visc}}_{q_\perp \to k_\perp}$$
$$+ \mathcal{T}^{C}_{q_\perp \to k_\perp} + \mathcal{T}^{F}_{q_\perp \to k_\perp}],$$

(B23)

where $\mathcal{T}^{F}_{q_\perp \to k_\perp}$ represents energy injection due to large-scale external forcing, and $\mathcal{T}^{C}_{q_\perp \to k_\perp}$ is the sum of all terms neglected in other transfer functions, which are related to compressive motions and various pressure forces:

$$\mathcal{T}^{C}_{q_\perp \to k_\perp} \equiv \int \left\{ -\langle \boldsymbol{a}^u \rangle_{k_\perp} \cdot \langle \boldsymbol{a}^u \rangle_{q_\perp} \frac{\boldsymbol{\nabla} \cdot \boldsymbol{u}}{2} \right.$$
$$- \langle \boldsymbol{a}^u \rangle_{k_\perp} \cdot \frac{1}{\sqrt{\varrho}} \boldsymbol{\nabla} \langle p_\perp + n T_e \rangle_{q_\perp}$$
$$- \langle \boldsymbol{a}^u \rangle_{k_\perp} \cdot \left[\frac{1}{2\sqrt{4\pi\varrho}} \boldsymbol{\nabla} (\boldsymbol{B} \cdot \langle \boldsymbol{a}^B \rangle_{q_\perp}) \right]$$
$$\left. + \langle \boldsymbol{a}^u \rangle_{k_\perp} \cdot \langle \boldsymbol{a}^{\Delta p} \rangle_{q_\perp} \vartheta_{\Delta p} \frac{\boldsymbol{\nabla} \cdot \sqrt{|\Delta p|} \hat{\boldsymbol{b}}}{\sqrt{\varrho}} \right\} d^3\boldsymbol{x}.$$

(B24)

The magnetic energy evolves according to a similar sum of energy-transfer functions:

$$\frac{d\mathcal{E}_{\text{mag}}}{dt} = \sum_{q_\perp k_\perp} [\mathcal{T}^{\text{MHD}}_{q_\perp \to k_\perp} + \mathcal{T}^{\text{kin}}_{q_\perp \to k_\perp} + \mathcal{T}^{A}_{q_\perp \to k_\perp}$$
$$+ \mathcal{T}^{C,B}_{q_\perp \to k_\perp} + \mathcal{T}^{\text{diss}}_{q_\perp \to k_\perp}],$$

(B25)

where

$$\mathcal{T}^{\text{MHD}}_{q_\perp \to k_\perp} \equiv \int \langle \boldsymbol{a}^B \rangle_{k_\perp} \cdot \left(\frac{\boldsymbol{B}}{\sqrt{4\pi\varrho}} \cdot \boldsymbol{\nabla} \langle \boldsymbol{a}^u \rangle_{q_\perp} \right) d^3\boldsymbol{x},$$

(B26)

$$\mathcal{T}^{\text{kin}}_{q_\perp \to k_\perp} \equiv \int -\langle \boldsymbol{a}^B \rangle_{k_\perp} \cdot \left(\frac{\boldsymbol{B}}{\sqrt{4\pi\varrho}} \cdot \boldsymbol{\nabla} \left\langle \frac{\sqrt{\varrho} \boldsymbol{J}}{ne} \right\rangle_{q_\perp} \right) d^3\boldsymbol{x},$$

(B27)

$$\mathcal{T}^{A}_{q_\perp \to k_\perp} \equiv \int -\langle \boldsymbol{a}^B \rangle_{k_\perp} \cdot \left[\left(\boldsymbol{u} - \frac{\boldsymbol{J}}{ne} \right) \cdot \boldsymbol{\nabla} \langle \boldsymbol{a}^B \rangle_{q_\perp} \right] d^3\boldsymbol{x},$$

(B28)

$$\mathcal{T}^{C,B}_{q_\perp \to k_\perp} \equiv \int \left\{ -\langle \boldsymbol{a}^B \rangle_{k_\perp} \cdot \langle \boldsymbol{a}^B \rangle_{q_\perp} \boldsymbol{\nabla} \cdot \boldsymbol{u} + \langle \boldsymbol{a}^B \rangle_{k_\perp} \cdot \langle \boldsymbol{a}^B \rangle_{q_\perp} \boldsymbol{\nabla} \cdot \frac{\boldsymbol{J}}{ne} \right.$$
$$\left. - \frac{1}{2} \langle \boldsymbol{a}^B \rangle_{k_\perp} \cdot \left(\langle \boldsymbol{a}^u \rangle_{q_\perp} - \left\langle \frac{\sqrt{\varrho} \boldsymbol{J}}{ne} \right\rangle_{q_\perp} \right) \frac{\boldsymbol{B}}{\sqrt{4\pi\varrho}} \cdot \frac{\boldsymbol{\nabla}\varrho}{\varrho} \right\} d^3\boldsymbol{x},$$

(B29)

$$\mathcal{T}^{\text{diss}}_{q_\perp \to k_\perp} \equiv \int \frac{\langle \boldsymbol{a}^B \rangle_{k_\perp}}{\sqrt{4\pi}} \cdot \left[\boldsymbol{\nabla} \times \left(\boldsymbol{\nabla}^2 \left\langle \frac{\eta_{\text{hyper}} \boldsymbol{J}}{ne} \right\rangle_{q_\perp} \right) \right] d^3\boldsymbol{x}.$$ (B30)

Finally, the thermal energy evolves according to

$$\frac{d\mathcal{E}_{\text{th}}}{dt} = \sum_{q_\perp k_\perp} [\mathcal{T}^{\text{th}}_{q_\perp \to k_\perp} + \mathcal{T}^{C,\text{th}}_{q_\perp \to k_\perp}],$$ (B31)

where

$$\mathcal{T}^{\text{th}}_{q_\perp \to k_\perp} \equiv \int \langle \boldsymbol{a}^{\Delta p} \rangle_{k_\perp} \cdot \left(\vartheta_{\Delta p} \sqrt{\frac{|\Delta p|}{\varrho}} \hat{\boldsymbol{b}} \cdot \boldsymbol{\nabla} \langle \boldsymbol{a}^u \rangle_{q_\perp} \right) d^3\boldsymbol{x},$$

(B32)

$$\mathcal{T}^{C,\text{th}}_{q_\perp \to k_\perp} \equiv \int \left\{ -\frac{\boldsymbol{\nabla} \cdot \langle \boldsymbol{a}^u \rangle_{k_\perp}}{\sqrt{\varrho}} \langle p_\perp \rangle_{q_\perp} - \frac{\langle \boldsymbol{a}^u \rangle_{k_\perp} \cdot \langle \boldsymbol{a}^u \rangle_{q_\perp}}{2} \boldsymbol{\nabla} \cdot \boldsymbol{u} \right.$$
$$\left. - \frac{1}{2} \langle \boldsymbol{a}^{\Delta p} \rangle_{k_\perp} \cdot \langle \boldsymbol{a}^u \rangle_{q_\perp} \vartheta_{\Delta p} \sqrt{\frac{|\Delta p|}{\varrho}} \hat{\boldsymbol{b}} \cdot \frac{\boldsymbol{\nabla}\varrho}{\varrho} \right\} d^3\boldsymbol{x}.$$ (B33)

The transfer functions $\mathcal{T}^{\text{Re}}_{q_\perp \to k_\perp}$, $\mathcal{T}^{\text{Max}}_{q_\perp \to k_\perp}$, and $\mathcal{T}^{\text{visc}}_{q_\perp \to k_\perp}$ for our $\beta_{i0} = 16$ simulation are shown in Fig. 18. The energy transfer due to Reynolds stress is consistent with a local cascade (see, e.g., Ref. [88]): there is a positive energy flux coming from large scales to small scales ($q_\perp < k_\perp$) and a similar negative flux from small scales to large scales ($q_\perp > k_\perp$). The energy transfers due to Maxwell and viscous stresses are mostly local: there is a positive energy-transfer rate at $q_\perp = k_\perp$ coming from the magnetic tension, and a negative transfer mediated by pressure anisotropy at the same $q_\perp$. However, unlike in a local MHD cascade, there is a considerable energy transfer at $q_\perp > k_\perp$ mediated by the Maxwell stress. This corresponds to the transfer of large-scale kinetic energy to small-scale magnetic energy, as we discuss in Sec. III C.

Finally, we note that the largest, advectionlike energy-transfer terms correspond to turbulent dynamics and microfluctuations produced by instabilities. These terms, however, do not describe thermalization of anisotropic thermal energy due to the effective collisionality. Studying this thermalization requires considering the full equation for pressure anisotropy, which involves higher-order moments of the distribution functions, such as the heat fluxes. Such an analysis goes beyond the scope of this paper.

APPENDIX C: ION DISTRIBUTION FUNCTION

Figure 19 shows the ion parallel and perpendicular distribution functions at the end of the $\beta_{i0} = 4$ and $\beta_{i0} = 16$ runs, defined as $f(w_\parallel) \equiv \int dw_\perp^2 f(w_\parallel, w_\perp)$ and $f(w_\perp) \equiv \int dw_\parallel f(w_\parallel, w_\perp)$. Both runs produce distribution functions close to a bi-Maxwellian with $T_\parallel > T_\perp$. The core of the parallel distribution function is flattened, which
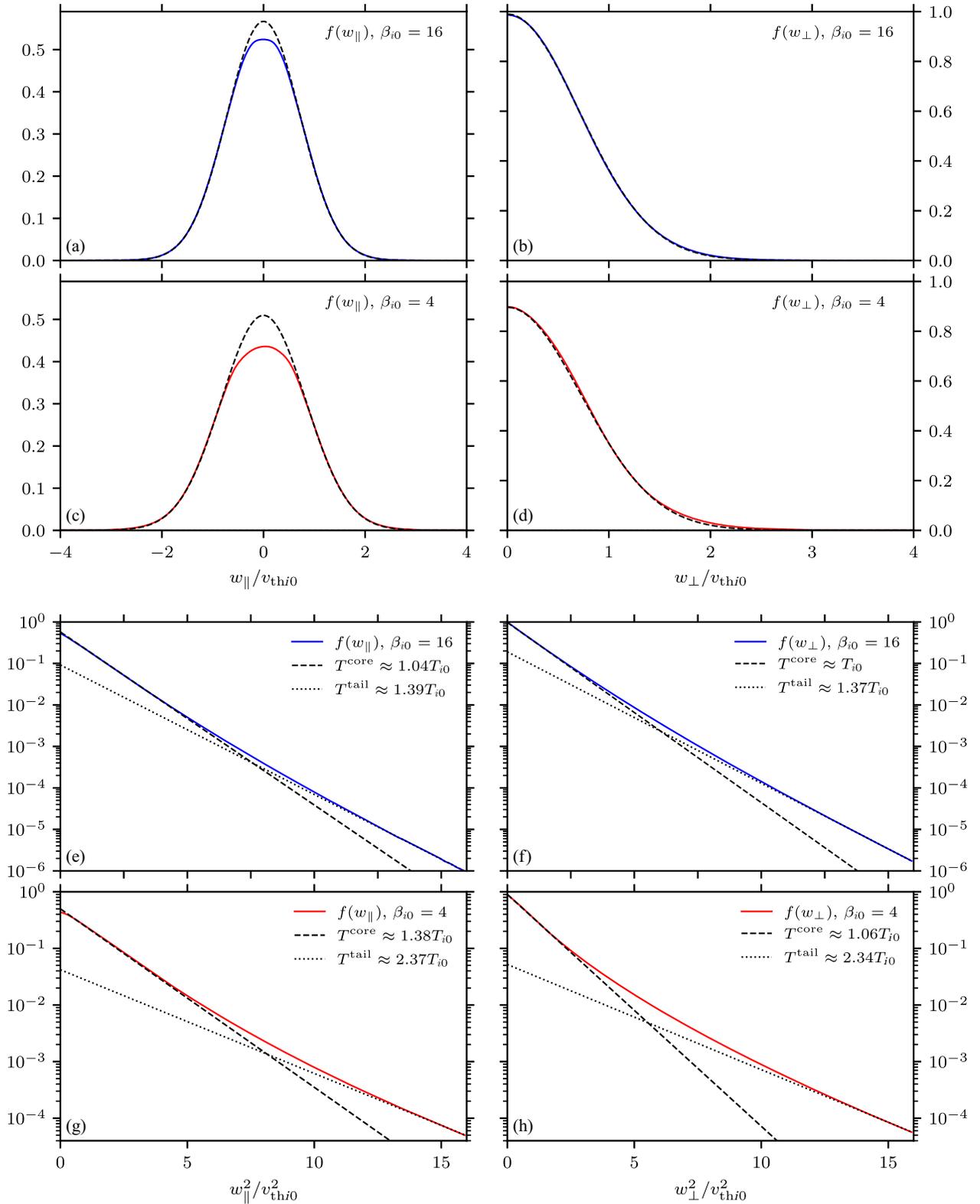
FIG. 19. Parallel (a),(c) and perpendicular (b),(d) ion distribution function at the end of the $\beta_{i0} = 16$ (a),(b) and $\beta_{i0} = 4$ (c),(d) simulations. Parallel distribution functions (a),(c) have a flat core, which we associate with the Landau damping and the firehose instability [45]. Dashed lines show best-fit Maxwellians to $f(w_\parallel)$ at $w_\parallel \approx 1.6 v_{\mathrm{th}i0}$ (in particular, from 1.59 to $1.61 v_{\mathrm{th}i0}$ to exclude the flattened part of the core) and to $f(w_\perp)$ at $w_\perp < v_{\mathrm{th}i0}$. (e)–(h) The same distribution functions, plotted on logarithmic scale. The core and the tail of the distributions may be approximated with Gaussians (straight lines in these coordinates). It is apparent that the wings of the distribution functions are much more isotropic than the cores ($T_\parallel^{\mathrm{tail}} \sim T_\perp^{\mathrm{tail}}$, while $T_\parallel^{\mathrm{core}} > T_\perp^{\mathrm{core}}$).

we attribute to Landau damping (mostly active in the early stages of the simulations) and to the nonlinear phase of the firehose instability [109].

Although the final distribution functions are not isotropic, the tails of those distributions are, as we show in Figs. 19(e)–19(h). This implies that pitch-angle scattering due to kinetic instabilities affects different parts of the distribution function differently, and causes the wings of the distribution function to be much more collisional, and therefore isotropic, than the cores. Similar features had been seen in the distribution functions of prior $\beta \sim 1$ simulations [79], in which pitch-angle scattering was present without instabilities, and in simulations of magnetized turbulence in an expanding box [45], in which anomalous scattering was associated with firehose fluctuations. Understanding such distribution functions requires careful examination of the particle-energy dependence of the effective collisionality, which falls beyond the scope of this paper.

---

[1] I. Zhuravleva, E. Churazov, P. Arévalo, A. A. Schekochihin, S. W. Allen, A. C. Fabian, W. R. Forman, J. S. Sanders, A. Simionescu, R. Sunyaev, A. Vikhlinin, and N. Werner, *Gas Density Fluctuations in the Perseus Cluster: Clumping Factor and Velocity Power Spectrum*, Mon. Not. R. Astron. Soc. **450**, 4184 (2015).

[2] F. K. Baganoff, Y. Maeda, M. Morris, M. W. Bautz, W. N. Brandt, W. Cui, J. P. Doty, E. D. Feigelson, G. P. Garmire, S. H. Pravdo, G. R. Ricker, and L. K. Townsley, *Chandra X-Ray Spectroscopic Imaging of Sagittarius A* and the Central Parsec of the Galaxy*, Astrophys. J. **591**, 891 (2003).

[3] E. Marsch and H. Goldstein, *The Effects of Coulomb Collisions on Solar Wind Ion Velocity Distributions*, J. Geophys. Res. **88**, 9933 (1983).

[4] P. Sharma, G. W. Hammett, E. Quataert, and J. M. Stone, *Shearing Box Simulations of the MRI in a Collisionless Plasma*, Astrophys. J. **637**, 952 (2006).

[5] M. W. Kunz, J. M. Stone, and E. Quataert, *Magnetorotational Turbulence and Dynamo in a Collisionless Plasma*, Phys. Rev. Lett. **117**, 235101 (2016).

[6] F. Foucart, M. Chandra, C. F. Gammie, E. Quataert, and A. Tchekhovskoy, *How Important Is Non-Ideal Physics in Simulations of Sub-Eddington Accretion on to Spinning Black Holes?*, Mon. Not. R. Astron. Soc. **470**, 2240 (2017).

[7] P. Kempski, E. Quataert, J. Squire, and M. W. Kunz, *Shearing-Box Simulations of MRI-Driven Turbulence in Weakly Collisional Accretion Discs*, Mon. Not. R. Astron. Soc. **486**, 4013 (2019).

[8] R. Narayan and I. Yi, *Advection-Dominated Accretion: A Self-Similar Solution*, Astrophys. J. Lett. **428**, L13 (1994).

[9] R. Narayan and I. Yi, *Advection-Dominated Accretion: Self-Similarity and Bipolar Outflows*, Astrophys. J. **444**, 231 (1995).

[10] K. Akiyama *et al.* (Event Horizon Telescope Collaboration), *First M87 Event Horizon Telescope Results. I. The Shadow of the Supermassive Black Hole*, Astrophys. J. Lett. **875**, L1 (2019).

[11] K. Akiyama *et al.* (Event Horizon Telescope Collaboration), *First Sagittarius A* Event Horizon Telescope Results. V. Testing Astrophysical Models of the Galactic Center Black Hole*, Astrophys. J. Lett. **930**, L16 (2022).

[12] A. A. Schekochihin, *MHD Turbulence: A Biased Review*, arXiv:2010.00699.

[13] A. A. Schekochihin, S. C. Cowley, W. Dorland, G. W. Hammett, G. G. Howes, E. Quataert, and T. Tatsuno, *Astrophysical Gyrokinetics: Kinetic and Fluid Turbulent Cascades in Magnetized Weakly Collisional Plasmas*, Astrophys. J. Suppl. Ser. **182**, 310 (2009).

[14] M. N. Rosenbluth, *Stability of the Pinch*, LANL Report LA-2030, 1956.

[15] E. N. Parker, *Dynamical Instability in an Anisotropic Ionized Gas of Low Density*, Phys. Rev. **109**, 1874 (1958).

[16] S. Chandrasekhar, A. N. Kaufman, and K. M. Watson, *The Stability of the Pinch*, Proc. R. Soc. A **245**, 435 (1958).

[17] A. A. Vedenov and R. Z. Sagdeev, *Some Properties of the Plasma with Anisotropic Distribution of the Velocities of Ions in the Magnetic Field*, Sov Phys Dokl **3**, 278 (1958).

[18] V. D. Shapiro and V. I. Shevchenko, *Quasilinear Theory of Instability of a Plasma with an Anisotropic Ion Velocity Distribution*, Sov. Phys. JETP **18**, 1109 (1964).

[19] A. Barnes, *Collisionless Damping of Hydromagnetic Waves*, Phys. Fluids **9**, 1483 (1966).

[20] D. J. Southwood and M. G. Kivelson, *Mirror Instability: 1. Physical Mechanism of Linear Instability*, J. Geophys. Res. **98**, 9181 (1993).

[21] R. Z. Sagdeev and V. D. Shafranov, *On the Instability of a Plasma with an Anisotropic Distribution of Velocities in a Magnetic Field*, Sov. Phys. JETP **39**, 181 (1960), http://jetp.ras.ru/cgi-bin/dn/e_012_01_0130.pdf.

[22] In making this statement, we implicitly assume conservation of adiabatic invariants. We discuss this in more detail in Sec. II.

[23] P. Goldreich and S. Sridhar, *Toward a Theory of Interstellar Turbulence. 2: Strong Alfvenic Turbulence*, Astrophys. J. **438**, 763 (1995).

[24] M. W. Kunz, A. A. Schekochihin, and J. M. Stone, *Firehose and Mirror Instabilities in a Collisionless Shearing Plasma*, Phys. Rev. Lett. **112**, 205003 (2014).

[25] M. A. Riquelme, E. Quataert, and D. Verscharen, *Particle-in-Cell Simulations of Continuously Driven Mirror and Ion Cyclotron Instabilities in High Beta Astrophysical and Heliospheric Plasmas*, Astrophys. J. **800**, 27 (2015).

[26] P. Hellinger and P. M. Trávníček, *Oblique Proton Fire Hose Instability in the Expanding Solar Wind: Hybrid Simulations*, J. Geophys. Res. **113**, A10109 (2008).

[27] L. Sironi and R. Narayan, *Electron Heating by the Ion Cyclotron Instability in Collisionless Accretion Flows. I. Compression-Driven Instabilities and the Electron Heating Mechanism*, Astrophys. J. **800**, 88 (2015).

[28] J. Squire, M. W. Kunz, E. Quataert, and A. A. Schekochihin, *Kinetic Simulations of the Interruption of Large-Amplitude Shear-Alfvén Waves in a High-β Plasma*, Phys. Rev. Lett. **119**, 155101 (2017).

[29] M. W. Kunz, J. Squire, A. A. Schekochihin, and E. Quataert, *Self-Sustaining Sound in Collisionless, High-β Plasma*, J. Plasma Phys. **86**, 905860603 (2020).

[30] S. Majeski, M. W. Kunz, and J. Squire, *Microphysically Modified Magnetosonic Modes in Collisionless, High-β Plasmas*, arXiv:2301.02273.

[31] S. Boldyrev, *On the Spectrum of Magnetohydrodynamic Turbulence*, Astrophys. J. **626**, L37 (2005).

[32] R. Meyrand, S. Galtier, and K. H. Kiyani, *Direct Evidence of the Transition from Weak to Strong Magnetohydrodynamic Turbulence*, Phys. Rev. Lett. **116**, 105002 (2016).

[33] A. Mallet, A. A. Schekochihin, and B. D. G. Chandran, *Refined Critical Balance in Strong Alfvénic Turbulence*, Mon. Not. R. Astron. Soc. **449**, L77 (2015).

[34] A. Kolmogorov, *The Local Structure of Turbulence in Incompressible Viscous Fluid for Very Large Reynolds' Numbers*, Dokl. Akad. Nauk SSSR **30**, 301 (1941).

[35] J. Cho and E. T. Vishniac, *The Anisotropy of Magnetohydrodynamic Alfvénic Turbulence*, Astrophys. J. **539**, 273 (2000).

[36] J. Maron and P. Goldreich, *Simulations of Incompressible Magnetohydrodynamic Turbulence*, Astrophys. J. **554**, 1175 (2001).

[37] T. S. Horbury, M. Forman, and S. Oughton, *Anisotropic Scaling of Magnetohydrodynamic Turbulence*, Phys. Rev. Lett. **101**, 175005 (2008).

[38] R. Bruno and V. Carbone, *The Solar Wind as a Turbulence Laboratory*, Living Rev. Solar Phys. **10**, 2 (2013).

[39] C. H. K. Chen, *Recent Progress in Astrophysical Plasma Turbulence from Solar Wind Observations*, J. Plasma Phys. **82**, 535820602 (2016).

[40] G. F. Chew, M. L. Goldberger, and F. E. Low, *The Boltzmann Equation and the One-Fluid Hydromagnetic Equations in the Absence of Particle Collisions*, Proc. R. Soc. A **236**, 112 (1956).

[41] E. N. Parker, *Newtonian Development of the Dynamical Properties of Ionized Gases of Low Density*, Phys. Rev. **107**, 924 (1957).

[42] E. N. Parker, *Dynamics of the Interplanetary Gas and Magnetic Fields*, Astrophys. J. **128**, 664 (1958).

[43] S. I. Braginskii, *Transport Processes in a Plasma*, Rev. Plasma Phys. **1**, 205 (1965).

[44] M. W. Kunz, I. G. Abel, K. G. Klein, and A. A. Schekochihin, *Astrophysical Gyrokinetics: Turbulence in Pressure-Anisotropic Plasmas at Ion Scales and Beyond*, J. Plasma Phys. **84**, 715840201 (2018).

[45] A. F. A. Bott, L. Arzamasskiy, M. W. Kunz, E. Quataert, and J. Squire, *Adaptive Critical Balance and Firehose Instability in an Expanding, Turbulent, Collisionless Plasma*, Astrophys. J. Lett. **922**, L35 (2021).

[46] M. W. Kunz, A. A. Schekochihin, C. H. K. Chen, I. G. Abel, and S. C. Cowley, *Inertial-Range Kinetic Turbulence in Pressure-Anisotropic Astrophysical Plasmas*, J. Plasma Phys. **81**, 325810501 (2015).

[47] J. Squire, E. Quataert, and A. A. Schekochihin, *A Stringent Limit on the Amplitude of Alfvénic Perturbations in High-beta Low-Collisionality Plasmas*, Astrophys. J. Lett. **830**, L25 (2016).

[48] S. Melville, A. A. Schekochihin, and M. W. Kunz, *Pressure-Anisotropy-Driven Microturbulence and Magnetic-Field Evolution in Shearing, Collisionless Plasma*, Mon. Not. R. Astron. Soc. **459**, 2701 (2016).

[49] If kinetic microinstabilities are active, the cascade can only be approximately conservative. In our derivation, we assume the energy leak due to instabilities to be small.

[50] A similar derivation of the effective viscous scale in a plasma dynamo whose viscosity is controlled by kinetic microinstabilities can be found in Ref. [52].

[51] D. A. St-Onge and M. W. Kunz, *Fluctuation Dynamo in a Collisionless, Weakly Magnetized Plasma*, Astrophys. J. Lett. **863**, L25 (2018).

[52] D. A. St-Onge, M. W. Kunz, J. Squire, and A. A. Schekochihin, *Fluctuation Dynamo in a Weakly Collisional Plasma*, J. Plasma Phys. **86**, 905860503 (2020).

[53] C. S. Ng and A. Bhattacharjee, *Scaling of Anisotropic Spectra due to the Weak Interaction of Shear-Alfvén Wave Packets*, Phys. Plasmas **4**, 605 (1997).

[54] P. Goldreich and S. Sridhar, *Magnetohydrodynamic Turbulence Revisited*, Astrophys. J. **485**, 680 (1997).

[55] J. Squire, A. A. Schekochihin, E. Quataert, and M. W. Kunz, *Magneto-Immutable Turbulence in Weakly Collisional Plasmas*, J. Plasma Phys. **85**, 905850114 (2019).

[56] K. T. Kim, P. P. Kronberg, P. E. Dewdney, and T. L. Landecker, *The Halo and Magnetic Field of the Coma Cluster of Galaxies*, Astrophys. J. **355**, 29 (1990).

[57] A. Bonafede, L. Feretti, M. Murgia, F. Govoni, G. Giovannini, D. Dallacasa, K. Dolag, and G. B. Taylor, *The Coma Cluster Magnetic Field from Faraday Rotation Measures*, Astron. Astrophys. **513**, A30 (2010).

[58] I. Zhuravleva, E. Churazov, A. A. Schekochihin, S. W. Allen, A. Vikhlinin, and N. Werner, *Suppressed Effective Viscosity in the Bulk Intergalactic Plasma*, Nat. Astron. **3**, 832 (2019).

[59] Y. Li, M.-L. Gendron-Marsolais, I. Zhuravleva, S. Xu, A. Simionescu, G. R. Tremblay, C. Lochhaas, G. L. Bryan, E. Quataert, N. W. Murray, A. Boselli, J. Hlavacek-Larrondo, Y. Zheng, M. Fossati, M. Li, E. Emsellem, M. Sarzi, L. Arzamasskiy, and E. T. Vishniac, *Direct Detection of Black Hole-Driven Turbulence in the Centers of Galaxy Clusters*, Astrophys. J. Lett. **889**, L1 (2020).

[60] L. Arzamasskiy *et al.* (to be published).

[61] M. W. Kunz, J. M. Stone, and X.-N. Bai, *Pegasus: A New Hybrid-Kinetic Particle-in-Cell Code for Astrophysical Plasma Dynamics*, J. Comput. Phys. **259**, 154 (2014).

[62] J. M. Stone, K. Tomida, C. J. White, and K. G. Felker, *The ATHENA++ Adaptive Mesh Refinement Framework: Design and Magnetohydrodynamic Solvers*, Astrophys. J. Suppl. Ser. **249**, 4 (2020).

[63] J. W. Belcher and L. Davis, Jr., *Large-Amplitude Alfvén Waves in the Interplanetary Medium, 2*, J. Geophys. Res. **76**, 3534 (1971).

[64] C.-Y. Tu and E. Marsch, *MHD Structures, Waves and Turbulence in the Solar Wind: Observations and Theories*, Space Sci. Rev. **73**, 1 (1995).

[65] R. Bruno and V. Carbone, *The Solar Wind as a Turbulence Laboratory*, Living Rev. Solar Phys. **2**, 4 (2005).

[66] F. Aharonian *et al.* (Hitomi Collaboration), *Temperature Structure in the Perseus Cluster Core Observed with Hitomi*, Proc. Astron. Soc. Jpn. **70**, 11 (2018).

[67] M. Murgia, F. Govoni, L. Feretti, G. Giovannini, D. Dallacasa, R. Fanti, G. B. Taylor, and K. Dolag, *Magnetic Fields and Faraday Rotation in Clusters of Galaxies*, Astron. Astrophys. **424**, 429 (2004).

[68] C. Vogt and T. A. Enßlin, *A Bayesian View on Faraday Rotation Maps—Seeing the Magnetic Power Spectra in Galaxy Clusters*, Astron. Astrophys. **434**, 67 (2005).

[69] F. Govoni, M. Murgia, V. Vacca, F. Loi, M. Girardi, F. Gastaldello, G. Giovannini, L. Feretti, R. Paladino, E. Carretti *et al.*, *Sardinia Radio Telescope Observations of Abell 194. The Intra-Cluster Magnetic Field Power Spectrum*, Astron. Astrophys. **603**, A122 (2017).

[70] C. Stuardi, A. Bonafede, L. Lovisari, P. Domínguez-Fernández, F. Vazza, M. Brüggen, R. J. van Weeren, and F. de Gasperin, *The Intracluster Magnetic Field in the Double Relic Galaxy Cluster Abell 2345*, Mon. Not. R. Astron. Soc. **502**, 2518 (2021).

[71] J. Walker, G. Lesur, and S. Boldyrev, *On the Nature of Magnetic Turbulence in Rotating, Shearing Flows*, Mon. Not. R. Astron. Soc. **457**, L39 (2016).

[72] F. Bacchini, L. Arzamasskiy, V. Zhdankin, G. R. Werner, M. C. Begelman, and D. A. Uzdensky, *Fully Kinetic Shearing-Box Simulations of Magnetorotational Turbulence in 2D and 3D. I. Pair Plasmas*, Astrophys. J. **938**, 86 (2022).

[73] Y. Kawazura, A. A. Schekochihin, M. Barnes, W. Dorland, and S. A. Balbus, *Energy Partition between Alfvénic and Compressive Fluctuations in Magnetorotational Turbulence with Near-Azimuthal Mean Magnetic Field*, J. Plasma Phys. **88**, 905880311 (2022).

[74] S. P. Gary, M. E. McKean, D. Winske, B. J. Anderson, R. E. Denton, and S. A. Fuselier, *The Proton Cyclotron Instability and the* Anisotropy/β *Inverse Correlation*, J. Geophys. Res. **99**, 5903 (1994).

[75] S. P. Gary, *The Mirror and Ion Cyclotron Anisotropy Instabilities*, J. Geophys. Res. **97**, 8519 (1992).

[76] P. Hellinger, P. Trávníček, J. C. Kasper, and A. J. Lazarus, *Solar Wind Proton Temperature Anisotropy: Linear Theory and WIND/SWE Observations*, Geophys. Res. Lett. **33**, L09101 (2006).

[77] F. Rincon, A. A. Schekochihin, and S. C. Cowley, *Non-Linear Mirror Instability*, Mon. Not. R. Astron. Soc. **447**, L45 (2015).

[78] Y. Kawazura, M. Barnes, and A. A. Schekochihin, *Thermal Disequilibration of Ions and eEectrons by Collisionless Plasma Turbulence*, Proc. Natl. Acad. Sci. U.S.A. **116**, 771 (2019).

[79] L. Arzamasskiy, M. W. Kunz, B. D. G. Chandran, and E. Quataert, *Hybrid-Kinetic Simulations of Ion Heating in Alfvénic Turbulence*, Astrophys. J. **879**, 53 (2019).

[80] S. S. Cerri, L. Arzamasskiy, and M. W. Kunz, *On Stochastic Heating and Its Phase-Space Signatures in Low-beta Kinetic Turbulence*, Astrophys. J. **916**, 120 (2021).

[81] G. G. Howes, K. G. Klein, and T. C. Li, *Diagnosing Collisionless Energy Transfer Using Field-Particle Correlations: Vlasov-Poisson Plasmas*, J. Plasma Phys. **83**, 705830102 (2017).

[82] J. C. Kasper, A. J. Lazarus, and S. P. Gary, *Wind/SWE Observations of Firehose Constraint on Solar Wind Proton Temperature Anisotropy*, Geophys. Res. Lett. **29**, 1839 (2002).

[83] S. D. Bale, J. C. Kasper, G. G. Howes, E. Quataert, C. Salem, and D. Sundkvist, *Magnetic Fluctuation Power Near Proton Temperature Anisotropy Instability Thresholds in the Solar Wind*, Phys. Rev. Lett. **103**, 211101 (2009).

[84] A. F. A. Bott, L. Arzamasskiy, M. W. Kunz, E. Quataert, and J. Squire, *Alfvénic Dynamics in Firehose-Susceptible High-β Plasmas* (to be published).

[85] See also Ref. [86] for the more recent Braginskii-MHD simulations of high-β turbulence.

[86] J. Squire, M. W. Kunz, L. Arzamasskiy, Z. Johnston, E. Quataert, and A. A. Schekochihin, *Pressure Anisotropy and Viscous Heating in Weakly Collisional Plasma Turbulence*, arXiv:2303.00468.

[87] R. H. Kraichnan, *Inertial Ranges in Two-Dimensional Turbulence*, Phys. Fluids **10**, 1417 (1967).

[88] P. Grete, B. W. O'Shea, K. Beckwith, W. Schmidt, and A. Christlieb, *Energy Transfer in Compressible Magneto-hydrodynamic Turbulence*, Phys. Plasmas **24**, 092311 (2017).

[89] For a critically balanced cascade, the effective collisionality becomes unable to regulate pressure anisotropy when $\nu_{\rm eff}/k_\perp \delta u_\perp \sim 1$, which corresponds to $k_\perp L \sim M_A^{9/2}\beta^{3/2}$; for our $\beta_{i0} = 16$ simulation, the latter is ≈ 2.8.

[90] Another potential explanation could have been scale dependence of the effective Alfvén speed. This explanation does not work for our simulations because pressure anisotropy is mostly concentrated at the outer scale.

[91] A more detailed model for the effective collisionality will be presented in an upcoming publication by A. F. A. Bott *et al.*

[92] I. W. Hoppock, B. D. G. Chandran, K. G. Klein, A. Mallet, and D. Verscharen, *Stochastic Proton Heating by Kinetic-Alfvén-Wave Turbulence in Moderately High-β Plasmas*, J. Plasma Phys. **84**, 905840615 (2018).

[93] Unfortunately, the $\beta_{i0} = 16$ simulation with double-mode driving does not have tracked particles, and the $\beta_{i0} = 16$ simulation with single-mode driving does not have the collisionality diagnostic. Therefore, in this figure, we combine diagnostics from these two different simulations. The simulations have similar distributions of $\tau_{\rm coll}$.

[94] J. Squire, R. Meyrand, M. W. Kunz, L. Arzamasskiy, A. A. Schekochihin, and E. Quataert, *High-Frequency Heating of the Solar Wind Triggered by Low-Frequency Turbulence*, Nat. Astron. **6**, 715 (2022).

[95] G. G. Howes, S. C. Cowley, W. Dorland, G. W. Hammett, E. Quataert, and A. A. Schekochihin, *Astrophysical Gyrokinetics: Basic Equations and Linear Theory*, Astrophys. J. **651**, 590 (2006).

[96] B. D. G. Chandran, B. Li, B. N. Rogers, E. Quataert, and K. Germaschewski, *Perpendicular Ion Heating by Low-Frequency Alfvén-Wave Turbulence in the Solar Wind*, Astrophys. J. **720**, 503 (2010).

[97] All intervals have significant energization at the outer scale, which is likely due to adiabatic processes such as the overall growth of the magnetic-field strength in the box.

[98] S. M. Ressler, A. Tchekhovskoy, E. Quataert, M. Chandra, and C. F. Gammie, *Electron Thermodynamics in GRMHD Simulations of Low-Luminosity Black Hole Accretion*, Mon. Not. R. Astron. Soc. **454**, 1848 (2015).

[99] A. Chael, M. Rowan, R. Narayan, M. Johnson, and L. Sironi, *The Role of Electron Heating Physics in Images and Variability of the Galactic Centre Black Hole Sagittarius A**, Mon. Not. R. Astron. Soc. **478**, 5209 (2018).

[100] P. Sharma, E. Quataert, G. W. Hammett, and J. M. Stone, *Electron Heating in Hot Accretion Flows*, Astrophys. J. **667**, 714 (2007).

[101] V. Zhdankin, D. A. Uzdensky, and M. W. Kunz, *Production and Persistence of Extreme Two-Temperature Plasmas in Radiative Relativistic Turbulence*, Astrophys. J. **908**, 71 (2021).

[102] G. G. Howes, S. C. Cowley, W. Dorland, G. W. Hammett, E. Quataert, and A. A. Schekochihin, *A Model of Turbulence in Magnetized Plasmas: Implications for the Dissipation Range in the Solar Wind*, J. Geophys. Res. **113**, A05103 (2008).

[103] M. D. McManus, T. A. Bowen, A. Mallet, C. H. K. Chen, B. D. G. Chandran, S. D. Bale, D. E. Larson, T. Dudok de Wit, J. C. Kasper, M. Stevens, P. Whittlesey, R. Livi, K. E. Korreck, K. Goetz, P. R. Harvey, M. Pulupa, R. J. MacDowall, D. M. Malaspina, A. W. Case, and J. W. Bonnell, *Cross Helicity Reversals in Magnetic Switchbacks*, Astrophys. J. Suppl. Ser. **246**, 67 (2020).

[104] R. Meyrand, J. Squire, A. A. Schekochihin, and W. Dorland, *On the Violation of the Zeroth Law of Turbulence in Space Plasmas*, J. Plasma Phys. **87**, 535870301 (2021).

[105] An important source of pressure anisotropy in the solar wind is its expansion and the consequent dilution of the interplanetary magnetic field [106]. See Ref. [45] for a recent discussion of how such expansion affects Alfvénic turbulence in a collisionless, magnetized plasma.

[106] E. Leer and W. I. Axford, *A Two-Fluid Solar Wind Model with Anisotropic Proton Temperature*, Sol. Phys. **23**, 238 (1972).

[107] C. H. K. Chen, A. Mallet, T. A. Yousef, A. A. Schekochihin, and T. S. Horbury, *Anisotropy of Alfvénic Turbulence in the Solar Wind and Numerical Simulations*, Mon. Not. R. Astron. Soc. **415**, 3219 (2011).

[108] S. S. Cerri, D. Grošelj, and L. Franci, *Kinetic Plasma Turbulence: Recent Insights and Open Questions from 3D3V Simulations*, Front. Astron. Space Sci. **6**, 64 (2019).

[109] A similar flattened-core feature was seen previously in a kinetic simulation of expanding Alfvénic turbulence, which was also affected by the firehose instability but exhibited significantly less Landau damping [45] because of its lower value of β_{i0}.